Chapter 3
Internal Waves in the Atmosphere and Ocean: Instability Mechanisms

Bruce R. Sutherland

Abstract This chapter summarizes and extends part of the lectures on internal gravity waves in the atmosphere and ocean by focusing upon the various instabilities associated with vertically propagating internal waves, including breaking due to convective overturning and shear, parametric subharmonic instability, and modulational instability associated with spatially localized wave packets.

Overview

Internal gravity waves move within a fluid whose density changes with height, and are driven by buoyancy forces. The waves can be subdivided broadly into two classes: interfacial and vertically propagating waves. Interfacial internal waves and modes move horizontally being confined by localized stratification and/or by horizontal boundaries at the top and bottom of the domain. Vertically propagating internal waves move upward and downward in continuously varying stratification. Here we will focus on the latter case, referring to them simply as "internal waves". (For an introduction to the theory for propagation, generation, and breaking of interfacial and internal waves, see the textbook by Sutherland 2010). The aim of this chapter is to examine some of the stability properties of vertically propagating internal waves. There are a myriad of mechanisms through which energy and momentum on the scale of the waves can be transferred to different scales. Understanding these processes is essential to improve predictions of the general circulation of the atmosphere and of mixing in the ocean. Particularly in the latter case, internal waves are an important conduit through which energy injected into the ocean at large scales (through surface winds or tidal flow over bottom topography) is ultimately dissipated, thus providing closure to the ocean energy budget. The use of linear theory is well established to estimate the breaking of waves due to overturning or (in the atmosphere) due to

B. R. Sutherland (✉)
Departments of Physics and of Earth and Atmospheric Sciences, University of Alberta, Edmonton, AB, Canada
e-mail: bsuther@ualberta.ca

M. Le Bars and D. Lecoanet (eds.), *Fluid Mechanics of Planets and Stars*,
CISM International Centre for Mechanical Sciences 595,
https://doi.org/10.1007/978-3-030-22074-7_3

interactions with the synoptic-scale winds near a critical level, which is where the ground-based horizontal phase speed of the waves matches the wind speed (Lindzen 1981). Because of the interest in mixing induced by oceanic internal waves, several new breaking mechanisms have only recently come under investigation. These include the breakdown of a wave beam reflecting from bottom topography with a critical slope (e.g., see Chalamalla and Sarkar 2016), breaking waves exerting drag upon oceanic eddies (Trossman et al. 2013; Marshall et al. 2017), or waves simply being trapped and eventually absorbed within an anticyclonic eddy (Danioux et al. 2015). These and other energy and momentum cascade processes are discussed in a recent review paper (Sutherland et al. 2019).

Although an entire book could be devoted to internal wave breaking, this chapter focuses specifically upon the stability of internal waves in the absence of topography, background flows, or other waves. Even with these restrictions, there are still many mechanisms through which internal waves may become unstable, whether through overturning, shear instability, parametric subharmonic instability, or modulational instability. In the section "Dispersion and Polarization Relations", we review the linear theory for small-amplitude, plane-periodic Boussinesq, and anelastic internal waves. Breaking conditions (whether due to convective overturning or shear instability) are then reviewed in the section "Breaking Conditions". In the section "Triad Resonant Instability" reviews the theory for triad resonance instability (TRI) with discussion of its adaptation to confined modes and internal wave beams. Moderately large amplitude quasi-monochromatic wave packets may be susceptible to modulational instability, as discussed in the section "Modulational Stability and Instability". Finally, future directions for research are discussed in the section "Future Directions".

Dispersion and Polarization Relations

The motion of internal waves is given by the laws of conservation of mass, momentum, and internal energy with additional approximations to filter the dynamics of sound waves and to account for the magnitude of background density variations in the vertical. In the ocean or in the atmosphere over small ($\lesssim 5\,\mathrm{km}$) vertical distances, the Boussinesq approximation is used: this amounts to treating density as a constant, ρ_0, where it multiplies the material derivative in the momentum equations; density variations are included only as they influence buoyancy. For internal waves with vertical structure or propagating over vertical distances larger than about 10 km, it is necessary to use the anelastic approximation. In this case, the background density profile $\bar{\rho}(z)$ multiplies the material derivative in the momentum equations. The way in which sound is filtered is different under these two approximations: a Boussinesq fluid is assumed to be incompressible; for an anelastic gas, the background density variations are accounted for in the mass conservation equation.

Explicitly, ignoring viscosity and dissipative effects, the equations are given by

$$\begin{array}{rr} \text{Boussinesq equations} & \text{anelastic equations} \\ \nabla \cdot \vec{u} = 0 & \nabla \cdot (\bar{\rho}\vec{u}) = 0 \\ \frac{Du}{Dt} - fv = -\frac{1}{\rho_0}\frac{\partial p}{\partial x} & \frac{Du}{Dt} - fv = -\frac{\partial}{\partial x}\left(\frac{p}{\bar{\rho}}\right) \\ \frac{Dv}{Dt} + fu = -\frac{1}{\rho_0}\frac{\partial p}{\partial y} & \frac{Dv}{Dt} + fu = -\frac{\partial}{\partial y}\left(\frac{p}{\bar{\rho}}\right) \\ \frac{Dw}{Dt} = -\frac{1}{\rho_0}\frac{\partial p}{\partial z} - b & \frac{Dw}{Dt} = -\frac{\partial}{\partial z}\left(\frac{p}{\bar{\rho}}\right) - b \\ \frac{Db}{Dt} = -N^2 w & \frac{Db}{Dt} = -N^2 w. \end{array} \tag{3.1}$$

Here we will examine internal waves in otherwise stationary fluid so that $\vec{u} = (u, v, w)$ represents the velocity fluctuations due to waves. We also assume that the fluid is uniformly stratified, meaning that the buoyancy frequency, N, is a constant. The buoyancy frequency represents the frequency (in radians per second) of vertical oscillations in the fluid which results when fluid is carried upward and so finds itself more dense than its surroundings or it is carried downward and finds itself lighter than its surroundings. In the ocean, over vertical domains less than about a kilometer (so that the thermodynamic effects of pressure upon density and temperature can be ignored), the buoyancy frequency is given by $N = [-(g/\rho_0)\, d\bar{\rho}/dz]^{1/2}$. The ocean is uniformly stratified where the density increases linearly with depth, corresponding to an approximately linear decrease in temperature and/or linear increase in salinity provided that these changes are not so large that the nonlinear equation of state of sea water needs to be taken into account. In the atmosphere, the buoyancy frequency is given generally by $N = [(g/\bar{\theta})\, d\bar{\theta}/dz]^{1/2}$, in which g is gravity and $\bar{\theta}(z)$ is the vertical profile of the background potential temperature. Explicitly, $\bar{\theta} \equiv \bar{T}(\bar{p}/p_0)^{-\kappa}$, in which $\bar{T}(z)$ and $\bar{p}(z)$, respectively, are the background temperature and pressure, p_0 is a reference pressure (typically taken to be that at the ground), and $\kappa \simeq 2/7$ for Earth's atmosphere, which is composed primarily of the diatomic molecules of nitrogen and oxygen. The atmosphere is uniformly stratified where the background temperature is constant with height in which case the potential temperature increases exponentially with height and the corresponding density decreases exponentially with height according to $\bar{\rho}(z) = \rho_0 \exp(-z/H_\rho)$, with $H_\rho = R_a T/g$ being the density scale height for air with gas constant $R_a = 287\,\mathrm{J/kg\,K}$. Internal waves exist on sufficiently small spatial scales that the influence of the Earth's rotation can be treated as approximately uniform with latitude, if its influence is considered at all. Thus, the Coriolis parameter, f, is taken to be constant. Finally, b represents the buoyancy associated with perturbations in the fluid: for the ocean $b \equiv -g\rho/\rho_0$; for the atmosphere $b \equiv g\theta/\bar{\theta}$.

What is clear from (3.1) is that the anelastic equations reduce to the Boussinesq equations by taking $\bar{\rho} \to \rho_0$. This is one reason why one can perform laboratory experiments in tanks filled with stratified salt solutions and yet still make predictions about stratified air flow on relatively small vertical scales in the atmosphere.

The equations for small-amplitude waves are produced by neglecting the advective terms in the material derivatives appearing in (3.1) so that $D/Dt \equiv \partial/\partial t + \vec{u} \cdot \nabla \to$

$\partial/\partial t$. In the Boussinesq approximation, this gives five coupled linear equations in five unknowns all having constant coefficients. The structure and dynamics of these waves are correspondingly straightforward to derive. For small-amplitude anelastic waves, the exponentially decreasing background density $\bar{\rho}$ leads to a moderately more involved analysis. Nonetheless, after combining the coupled equations to a single equation in one unknown, the mass streamfunction, the result is a partial differential equation with constant coefficients, and so is straightforward to solve. These procedures are discussed in more detail below.

Boussinesq Internal Waves

After linearizing the Boussinesq equations in (3.1), we seek plane-periodic solutions with the understanding from the superposition principle that any solution can be written as a sum of waves. Thus, we seek solutions of the form

$$(u, v, w, b, p) = (A_u, A_v, A_w, A_b, A_p) \exp[\imath(kx + \ell y + mz - \omega t)], \tag{3.2}$$

in which it is understood that the actual field is the real part of the right-hand side expression. Each of the constant amplitudes (A_u, etc) is possibly complex valued such that its magnitude represents the actual amplitude and its argument represents the phase.

Substituting (3.2) into (3.1) thus results in an algebraic matrix eigenvalue problem whose eigenvalue gives the dispersion relation (an equation relating the frequency, ω, to the wavenumber $\vec{k} = (k, \ell, m)$) and whose eigenvector gives the polarization relations (the relationship between the amplitudes of each field). Explicitly, the dispersion relationship for Boussinesq internal waves is

$$\omega^2 = \frac{N^2(k^2 + \ell^2) + f^2 m^2}{k^2 + \ell^2 + m^2} = N^2 \cos^2\Theta + f^2 \sin^2\Theta, \tag{3.3}$$

where in the last expression we have defined $\Theta \equiv \tan^{-1}(m/k_h)$ with $k_h \equiv (k^2 + \ell^2)^{1/2}$ being the horizontal wavenumber. Thus, Θ represents the angle from the horizontal of the wavenumber vector or, equivalently, the angle from the vertical of lines of constant phase. Supposing that the maximum vertical displacement, A_0, is prescribed and the phase is arbitrarily set so that the vertical displacement amplitude $A_\eta = A_0$ is real valued, then the polarization relations can be written to express how the amplitudes of the remaining fields depend upon A_0. For mathematical convenience, we further simplify the results by supposing the x-axis points in the horizontal direction of propagation of the waves. (Such a transformation is possible because the full Eq. (3.1) is invariant upon rotation about the z-axis provided that the Coriolis parameter, f, is constant.) In effect, this allows us to set $\ell = 0$ so that $k_h = k$. The results are given in Table 3.1 and illustrated in Fig. 3.1.

Table 3.1 Polarization relations for Boussinesq internal waves giving (left) the possibly complex amplitudes and (right) the actual fields supposing the vertical displacement amplitude A_0 is real valued

$A_\eta = A_0$	$\Rightarrow$	$\eta = A_0 \cos(kx + mz - \omega t)$
$A_u = \imath\omega \tan\Theta\ A_0$	$\Rightarrow$	$u = -\omega\,(m/k)\ A_0 \sin(kx + mz - \omega t)$
$A_v = f \tan\Theta\ A_0$	$\Rightarrow$	$v = f\,(m/k)\ A_0 \cos(kx + mz - \omega t)$
$A_w = -\imath\omega\ A_0$	$\Rightarrow$	$w = \omega\ A_0 \sin(kx + mz - \omega t)$
$A_b = -N^2\ A_0$	$\Rightarrow$	$b = -N^2\ A_0 \cos(kx + mz - \omega t)$

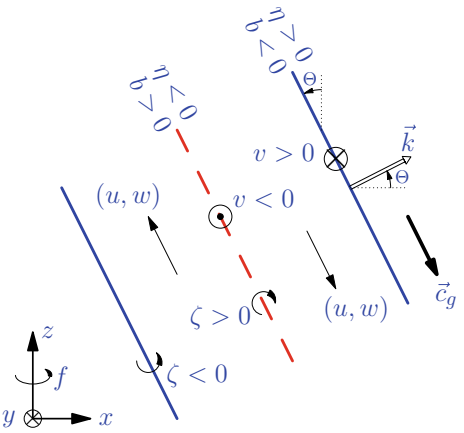

Fig. 3.1 Schematic illustrating the polarization relations associated with internal waves in the x–z plane having phase (group) velocity directed upward (downward) to the right. The Coriolis parameter is taken to be positive. Circles with crosses inside indicate vectors pointing into the page, whereas circles with filled circles inside indicate vectors pointing out of the page. The spanwise vorticity is indicated by ζ

Of course another approach to come up with these results is to combine the five coupled linearized Boussinesq equations in (3.1) to form a single differential equation. Assuming the waves have no structure in the y-direction, this is done most straightforwardly by defining the streamfunction ψ implicitly through $u = -\partial_z\psi$ and $w = \partial_x\psi$, thus automatically satisfying the condition for incompressibility. The terms involving pressure are eliminated by taking the spanwise component of the curl of the momentum equations and so arriving at an equation for the spanwise vorticity, $\zeta = \partial_z u - \partial_x w = -\nabla^2\psi$. Finally, buoyancy can be eliminated by using the internal energy equation. If this procedure is followed retaining the nonlinear terms, the resulting fully nonlinear equation for the evolution of the streamfunction is

$$[\partial_{tt}\nabla^2 + N^2\partial_{xx} + f^2\partial_{zz}]\psi = \nabla\cdot[\partial_t(\zeta\vec{u}) - \partial_x(b\vec{u}) + f\partial_z(v\vec{u})]. \tag{3.4}$$

For small-amplitude waves, the right-hand side can be neglected and the resulting linear partial differential equation can immediately be seen to give the dispersion relation (3.3).

Anelastic Internal Waves

Because of the z-dependent coefficients involving $\bar{\rho}$ in the anelastic equations given in (3.1), one cannot start by assuming solutions with vertical periodicity in z. Instead, after linearizing it is necessary to combine the equations to form one equation in one unknown. As with Boussinesq waves, we simplify the algebra by orienting the x-axis in the horizontal direction of propagation of the waves, thus eliminating terms involving y-derivatives in (3.1). From the expression for mass conservation of anelastic waves, $\nabla \cdot (\bar{\rho}\vec{u}) = 0$, we define the mass streamfunction, Ψ, implicitly so that $u = -(1/\bar{\rho})\partial_z \Psi$ and $w = (1/\bar{\rho})\partial_x \Psi$. We then proceed as described above for Boussinesq flow by taking the spanwise curl of the momentum equations to give an evolution equation for the spanwise vorticity,

$$\zeta = \partial_z u - \partial_x w = -(1/\bar{\rho})[\nabla^2 \Psi + (1/H_\rho)\partial_z \Psi], \tag{3.5}$$

in which $H_\rho \equiv -(\bar{\rho}'/\bar{\rho})^{-1}$ is the density scale height and, for simplicity, the influence of the Earth's rotation has been neglected. Eliminating buoyancy from the resulting equations and neglecting background rotation gives

$$\frac{\partial^2}{\partial t^2}\nabla^2 \Psi + \frac{1}{H_\rho}\frac{\partial^3 \Psi}{\partial t^2 \partial z} + N^2 \frac{\partial^2 \Psi}{\partial x^2} = 0. \tag{3.6}$$

This reduces to the linearized Boussinesq equation (3.4) with f = 0 by taking the limit $H_\rho \to \infty$.

Because both N and H_ρ are constant in an isothermal, uniformly stratified atmosphere it is possible to find solutions to (3.6) in the form of an exponential: $\Psi = A_\Psi \exp[\imath(kx + Mz - \omega t)]$, in which the z-dependent background suggests that M is not necessarily real valued. Indeed, by substituting into (3.6), we find $M = m + \imath/(2H_\rho)$, in which m is the usual real-valued vertical wavenumber. Thus, the mass streamfunction has the form of a exponentially decaying oscillator with height. The corresponding velocity fields increase exponentially with height according to

$$\begin{aligned} u &= -\tfrac{1}{\rho_0}(\imath m - 1/2H_\rho)\, A_\Psi\, e^{z/2H_\rho}\, e^{\imath(kx+mz-\omega t)} \\ w &= \tfrac{1}{\rho_0}(\imath k)\, A_\Psi\, e^{z/2H_\rho}\, e^{\imath(kx+mz-\omega t)}, \end{aligned} \tag{3.7}$$

and the dispersion relation for anelastic waves not influenced by the Earth's rotation is given by $\omega^2 = N^2 k^2\, [k^2 + m^2 + (4H_\rho)^{-2}]^{-1/2}$. While it may seem unphysical that u and w appear to be unbounded, the exponential increase in these fields follows directly

from the physical requirement that momentum is conserved, which is to say that in the absence of breaking the horizontally averaged vertical flux of horizontal momentum, $\bar{\rho}\langle uw\rangle$, must be constant. The velocities increase because the background density decreases with height. In reality, waves do not grow to infinite amplitude: upward-propagating waves eventually grow to such large amplitude that weakly nonlinear effects (ignored in the derivation of (3.6)) begin to play a role and eventually fully nonlinear effects of convective overturning and turbulent breakdown occur.

Breaking Conditions

Although linear theory strictly makes reliable predictions only for waves of sufficiently small amplitude, it is insightful to extrapolate the results for waves that are of such large amplitude that they are overturning or otherwise lead to fine-scale instabilities associated with breaking waves (Lindzen 1981). While we can imagine that anelastic waves eventually grow to such large amplitude that they break, the breaking itself is expected to occur over small vertical scales compared with the density scale height. This gives some justification for using the polarization relations for Boussinesq waves to examine breaking.

Overturning

Internal waves are overturning if the amplitude is so large that the waves carry dense fluid over less dense fluid rendering the fluid locally to be unstably stratified. Mathematically, this means that the total squared buoyancy frequency, $N_T^2 \equiv N^2 + \Delta N^2$, composed of the background squared buoyancy frequency plus the change due to waves $\Delta N^2 \equiv \partial b/\partial z$, is negative somewhere in the flow field. Thus, the condition for the critical vertical displacement amplitude $A_{\rm OT}$ of waves on the cusp of overturning is $\min\{[\Delta N^2/N^2]\}|_{A=A_{\rm OT}} = -1$. Using the polarization relations in Table 3.1 gives

$$A_{\rm OT} = \left|\frac{1}{m}\right|. \tag{3.8}$$

Convection

Just because the waves are overturning, it does not mean they will necessarily convectively breakdown. This is because convective instability itself takes time to grow. If the growth rate is not sufficiently fast, the waves may pull back the overturned fluid so that the region becomes stably stratified again.

Thus, an assessment of whether convection actually occurs is found by comparing the growth rate, σ_c, for convection with the frequency, ω, of the waves. The growth rate itself is given by the maximum value of $(-N_T^2)^{1/2}$ in which the discriminant is evaluated where the local total stratification is unstable ($N_T^2 < 0$). The critical vertical displacement amplitude, $A_{\rm CV}$, of overturning waves that are susceptible to convection is given implicitly by the condition $\sigma_c = \omega$. Using the polarization and dispersion relations, we find

$$A_{\rm CV} = \left|\frac{1}{m}\right| \left(1 + \frac{\omega^2}{N^2}\right), \tag{3.9}$$

in which the frequency is given by (3.3). In the low-frequency limit, appropriate for near-inertial internal waves, $A_{\rm CV} \simeq A_{\rm OT}$.

Shear Instability

For near-inertial internal waves, which have low frequency close to f, their motion is close to horizontal ($\Theta \lesssim 90°$). Thus, even if the waves are not overturning, it is possible for shear instability to develop and ultimately result in the breakdown of the waves. A necessary condition for the linear instability of a parallel stratified shear flow is that the minimum gradient Richardson number, Ri_g, is below 1/4. For the case of internal waves moving in the x–z plane ($\ell = 0$), Ri_g is the ratio of the local stratification, N_T^2, to the square of the local vertical shear $\partial u/\partial z$. For small amplitude, non-overturning waves, it turns out that this has a minimum close to where the stratification is unaffected by the waves ($\Delta N^2 = 0$) but where the shear is strongest (see Sect. 4.6.3 of Sutherland 2010). Thus, the critical vertical displacement amplitude for waves satisfying $\min\{\mathrm{Ri}_g\} = 1/4$ is

$$A_{\rm SHR} = 2\frac{N|k|}{\omega m^2}\sqrt{1 - \left(\frac{Nk}{\omega m}\right)^2}. \tag{3.10}$$

This criterion is met for amplitudes below the overturning threshold ($A_0 = A_{\rm OT}$) for internal waves having $|k/m| < \sqrt{f/N} \simeq 0.1$, in which the last value is estimated from characteristic values in the atmosphere and ocean of $f \sim 10^{-4}\mathrm{s}^{-1}$ and $N \sim 10^{-2}\mathrm{s}^{-1}$.

Summary of Breaking Instabilities

Figure 3.2 plots the critical amplitudes $A_{\rm OT}$, $A_{\rm CV}$, and $A_{\rm SHR}$ against relative wave numbers. Also shown in Fig. 3.2a is the prediction for instability due to

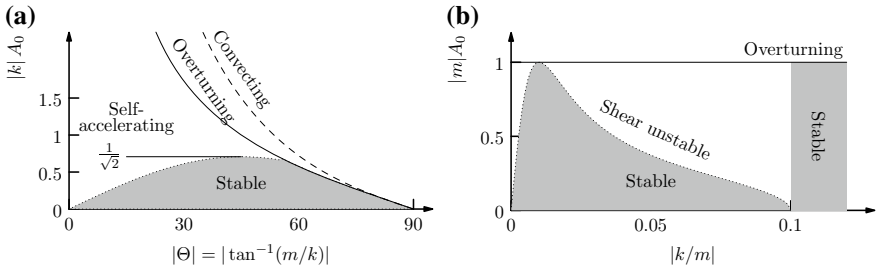

Fig. 3.2 Breaking regimes heuristically predicted from linear theory showing (**a**) the critical amplitudes associated with overturning and convective instability as well as self-acceleration and (**b**) the critical amplitude associated with stratified shear instability of near-inertial waves. (Adapted with permission from Fig. 4.18 of Sutherland 2010)

self-acceleration, a weakly nonlinear mechanism to be discussed in the section "Modulational Stability and Instability". Focusing on the high-frequency non-hydrostatic waves in Fig. 3.2a, it appears that the waves become unstable to self-acceleration before reaching overturning amplitudes. This is bourne out in simulations of horizontally periodic vertically localized wave packets though fully localized non-hydrostatic wave packets may achieve higher amplitudes before being driven to overturn by the effects of self-acceleration (e.g., see Sutherland 2001). Focusing on the near-inertial waves in Fig. 3.2b, it is clear that the waves become unstable due to shear instability before reaching overturning amplitudes if their wavenumber is such that $|k/m| < (f/N)^{1/2}$. Surprisingly, if $|k/m| \lesssim (f/N)^{1/2}$ then even waves with very small amplitude are susceptible to shear instability.

Triad Resonant Instability

Parametric subharmonic instability (PSI) or, more generally, triad resonant instability (TRI) is considered as a potentially important and pervasive mechanism for the breakdown of internal waves, particularly in the ocean where anelastic growth cannot contribute to drive the waves to breaking through one of the mechanisms described above. The general theory was developed for plane periodic waves (Hasselmann 1967) and applied specifically to internal waves by several researchers (see reviews by Phillips (1981); Staquet and Sommeria (2002); Dauxois et al. (2018)). Mathematically, TRI is a consequence of weakly nonlinear interactions between a triplet of waves including a "parent wave" with wavenumber $\vec{k}_0$ and a pair of "sibling waves" with wave numbers $\vec{k}_\pm$. Through the nonlinear advective terms in the equations of motion, energy can pass between the parent and siblings provided they satisfy the resonance conditions

$$\begin{aligned} \vec{k}_0 &= \pm\vec{k}_+ \pm \vec{k}_- \\ \omega_0 &= \pm\omega_+ \pm \omega_-, \end{aligned} \tag{3.11}$$

in which the frequencies ω_0 and $\omega_\pm$ are given by the corresponding dispersion relations. Even for waves restricted to the x–z plane, there are a rich number of solutions to these three equations in four unknowns. Of these it remains to determine for which the amplitudes of the sibling waves indeed grow. These are the waves that are expected to grow out of noise, extracting energy from the parent wave with the fastest growing siblings expected to be dominant.

Taking a somewhat different approach from that of previous researchers (Benielli and Sommeria 1998; Bourget et al. 2013), we begin by working with the fully nonlinear Boussinesq equations in the form given by (3.4). The parent wave is characterized in terms of the streamfunction in which extracting the real part of the complex exponential is made explicit:

$$\psi_0 = \frac{1}{2} a_0 \exp[\imath\,(k_0 x + m_0 z - \omega_0 t)] + \text{c.c.}, \tag{3.12}$$

in which c.c. denotes the complex conjugate. Likewise, the sibling waves have streamfunction

$$\psi_\pm = \frac{1}{2} a_\pm \exp[\imath\,(k_\pm x + m_\pm z - \omega_\pm t)] + \text{c.c.}. \tag{3.13}$$

The polarization relations can be used to find corresponding expressions for the vorticity, velocity, and buoyancy associated with the parent and sibling waves. In all these expressions, the amplitudes a_0 and $a_\pm$ are considered to be functions of time allowing for the possible growth of the sibling waves at the expense of the parent.

Putting these results into (3.4) together with the resonance conditions (3.11) gives a triplet of equations expressing how two of the waves interact to influence the third wave. In particular, the interaction between the parent and the "+" sibling to influence the "−" sibling is expressed through

$$\begin{aligned}&[\partial_{tt}\nabla^2 + N^2\partial_{xx} + f^2\partial_{zz}]\psi_- = \\ &\quad \nabla\cdot[\partial_t(\zeta_0\vec{u}_+ + \zeta_+\vec{u}_0) - \partial_x(b_0\vec{u}_+ + b_+\vec{u}_0)] + f\partial_z(v_0\vec{u}_+ + v_+\vec{u}_0)].\end{aligned} \tag{3.14}$$

With use of (3.12) and (3.13) and the corresponding polarization relations, this can then be written as an equation for the time evolution of the amplitude a_-. In doing so, it is convenient to assume that the growth rate is small compared to the wave frequency so that $\|d_{tt}a_-\| \ll \omega_-\|d_t a_-\|$ and the term $d_t(a_0 a_+^\star)$ arising on the right-hand side of (3.14) is considered to be negligible.

The resulting equation can be written $d_t a_- = I_- a_0 a_+^\star$, in which I_- is an expression involving the wave numbers of the parent wave and the "+" sibling. Similarly, the evolution equation for the amplitude of the "+" sibling can be written $d_t a_+ = I_+ a_0 a_-^\star$. Combining these results gives

$$\frac{d^2}{dt^2} a_+ = I_+ I_-^\star\, |a_0|^2\, a_+. \tag{3.15}$$

Thus, through the process of passing energy from one sibling to the other via the parent, it is possible for both siblings to grow in amplitude. Assuming the change in a_0 is small while the sibling amplitudes are small, so that $|a_0|$ can be treated as a constant in (3.15), the growth is exponential with growth rate, σ_p, given by the positive real part of $\sqrt{I_+ I_-^\star}\,|a_0|$. (As $|a_\pm|$ grows to be comparable to $|a_0|$, the waves can saturate or, if $|a_0|$ is sufficiently large, additional nonlinear effects can lead to energy being transferred to a broader frequency spectrum possibly leading to overturning.)

If rotation is neglected, then $I_\pm$ is pure real. In this case, it is possible for there to be no growth of sibling waves if their wave numbers are such that $I_+ I_- < 0$. However, numerous studies have shown growth for a range of sibling waves in two dimensions (Mied 1976) and for a wide range in three dimensions (Klostermeyer 1991; Lombard and Riley 1996).

Although the resonance conditions (3.11) strictly require the waves to be perfectly periodic in infinite space, sibling waves may also grow from a bounded parent mode in uniform stratification if the wave numbers of the sibling waves are sufficiently small that a wavelength can fit inside the domain. This has been observed in laboratory experiments (Bouruet-Aubertot et al. 1995; Benielli and Sommeria 1998), as shown in Fig. 3.3a.

TRI has also been observed for horizontally propagating vertically confined internal waves having a mode-1 vertical structure (Joubaud et al. 2012), as shown in Fig. 3.3b. Recent advances have been made in the study of TRI for internal wave beams (Bourget et al. 2013; Karimi and Akylas 2014; Dauxois et al. 2018), showing that sibling waves can grow within and emerge from a parent beam if there are a sufficient number of wavelengths of parent waves within the beam. For the interpretation of experiments showing TRI occurring within an internal wave beam (Fig. 3.3c), Bourget et al. (2013) included viscosity in their theoretical analysis.

Modulational Stability and Instability

If the amplitude of the waves varies in space, as surely occurs for naturally occurring internal waves, then there is another mechanism for amplitude growth or decay in time resulting from the waves inducing a flow that then Doppler shifts the waves themselves. If resulting in amplitude growth, the waves are said to be modulationally unstable. Otherwise, they are modulationally stable, meaning that their amplitude decreases faster than linear theory for dispersion would predict. The structure of the induced flow and its consequent impact back upon the waves depends non-trivially upon the dimensionality of the amplitude envelope, which describes the space- and time-dependent amplitude of the waves.

Conceptually, it is most straightforward to understand the physics of induced flows by considering a one-dimensional wave packet, which is spanwise uniform and horizontally periodic so that the amplitude envelope varies spatially only in the vertical. Thus, the vertical displacement field for a 1D Boussinesq wave packet is

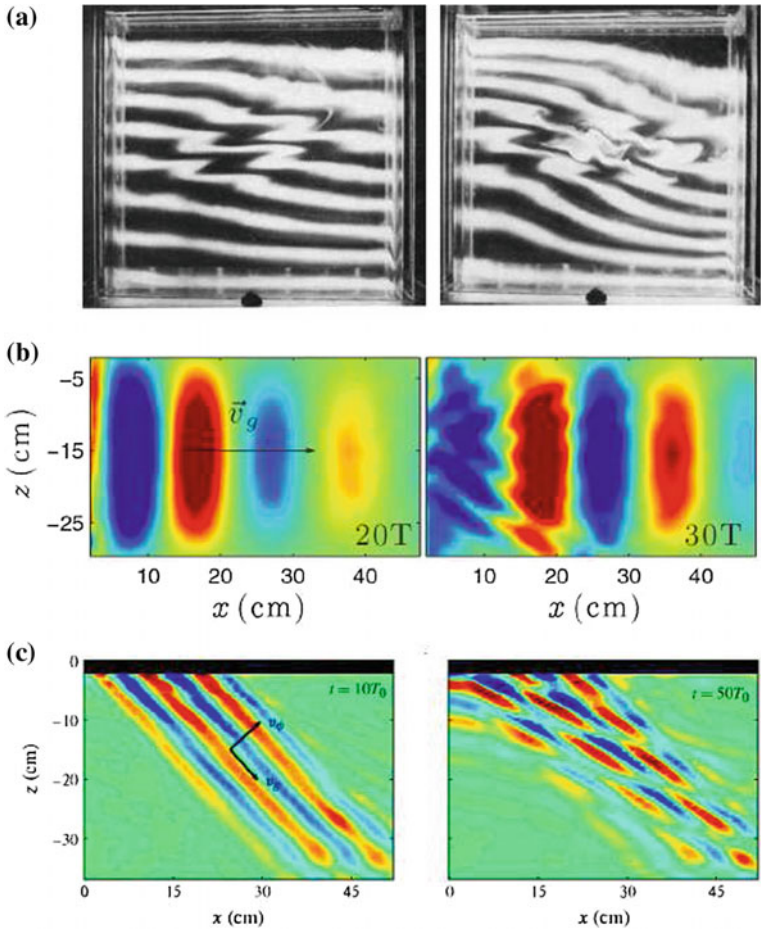

Fig. 3.3 Observations in laboratory experiments of TRI occurring for internal waves as (**a**) a mode in an oscillating square tank (adapted with permission from Fig. 6 of Bouruet-Aubertot et al. 1995), (**b**) a horizontally propagating vertically confined mode (adapted with permission from Fig. 1 of Joubaud et al. 2012), and (**c**) a down and rightward propagating beam (adapted with permission from Fig. 2 of Bourget et al. 2013)

written

$$\eta(x, z, t) = \frac{1}{2} A(Z, T) e^{\imath(kx+mz-\omega t)} + \text{c.c.}. \tag{3.16}$$

Assuming the modulated waves are quasi-monochromatic, the variables Z and T, respectively, represent slow variations in the vertical and in time as compared with the vertical wavelength and period of the waves.

Using the polarization relations in Table 3.1, the leading-order expressions for the corresponding horizontal and vertical velocity fields are

$$\begin{aligned} u_1(x,z,t) &= \tfrac{1}{2}\imath(\omega m/k)\, A(Z,T)\, e^{\imath(kx+mz-\omega t)} + \text{c.c.} \\ w_1(x,z,t) &= -\tfrac{1}{2}\imath\omega\, A(Z,T)\, e^{\imath(kx+mz-\omega t)} + \text{c.c.}, \end{aligned} \tag{3.17}$$

in which the subscripts emphasize that these fields, arising from linear theory, are proportional to the amplitude. The mean momentum flux, $F_z = \rho_0 \langle u_1 w_1 \rangle$, is straightforwardly computed from the cross-terms of the product, $u_1 w_1$, for which the complex conjugate cancels the complex exponential leaving only the slow variations. Explicitly,

$$F_z = -\rho_0 \frac{\omega^2 m}{2k} |A|^2. \tag{3.18}$$

Rightward propagating wave packets with upward group velocity, c_{gz}, have $k > 0$ and $m < 0$, and so $F_z > 0$ for such waves as expected.

Being horizontally periodic and incompressible, one can write the x-momentum equation in flux-form and average over one horizontal wavelength. For conceptual convenience we neglect rotation and so find

$$\frac{\partial}{\partial t}\left(\rho_0 \langle u \rangle\right) = -\frac{\partial}{\partial z} F_z. \tag{3.19}$$

The key here is to recognize that u on the left-hand side is not the u_1 appearing in (3.17). Instead it is a quantity proportional to the amplitude squared and which is independent of x. For convenience, we will write $u_2 \equiv \langle u \rangle$ on the left-hand side of (3.19). Thus, $\partial_t u_2$ represents the horizontal acceleration of the background resulting from the divergence of the momentum flux.

For plane waves the amplitude is constant and, consequently, so is the momentum flux, F_z. Hence, there is no force or corresponding flow induced by plane waves until they break or otherwise dissipate. However, even without dissipation, modulated internal wave packets do induce a (time-changing) flow directly as a consequence of the vertical variation in F_z. An example with an upward-propagating wave packet having a Gaussian amplitude envelope is illustrated in Fig. 3.4. The momentum flux is largest where the amplitude is largest at the vertical center of the wave packet. Corresponding to the decrease in the momentum flux going upward from this point there is a time-transient acceleration of the background flow. Likewise, the momentum flux increases going upward from below the wave packet to its center and so there the background flow decelerates after the center of the wave packet passes. The net increase in speed due to the acceleration occurring on the leading flank of the wave packet is canceled by the net decrease occurring on the trailing flank. And so the speed of the background flow remains the same from before to after the passage of the wave packet. However, a floating particle (a passive tracer) will find itself displaced rightward from its initial position.

A formula for the induced flow itself can be found if one assumes the flow is steady in a frame of reference moving with the group velocity of the wave packet. That is, we suppose $u_2(z,t) = u_2(\tilde{z})$ in which $\tilde{z} \equiv z - c_{gz} t$. Likewise, we know that the amplitude envelope translates at the group velocity and assume that time variations in the translating frame due to wave packet dispersion occur on much

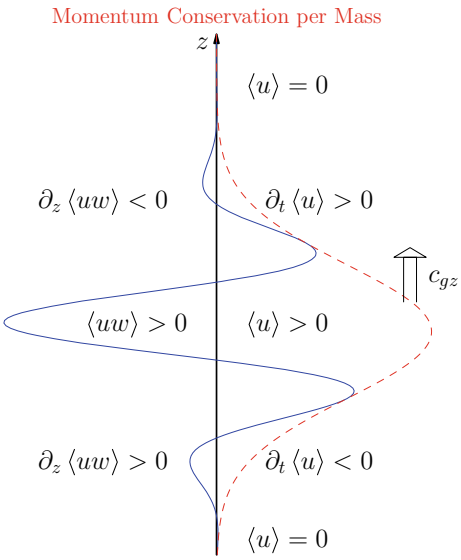

Fig. 3.4 Schematic illustrating the physical mechanism for the transient acceleration of the mean flow due to the divergence of the momentum flux associated with a wave packet. The curved solid line represents vertical variations of, e.g., displacement along some vertical cut; the dashed line represents the amplitude envelope, which translates vertically upward at the group velocity c_{gz}

slower time scales. Thus, we can approximate $A(Z, T) \simeq A(\tilde{z})$ in the expression for F_z in (3.18). So, changing co-ordinates in (3.19) to the translating frame gives $-c_{gz}\partial_{\tilde{z}}(\rho_0 u_2) = -\partial_{\tilde{z}} F_z$. Integrating both sides and using (3.18) gives

$$u_2 = -\frac{1}{2}\frac{1}{c_{gz}}\frac{\omega^2 m}{k}|A|^2 = \frac{1}{2}N|\vec{k}||A|^2, \tag{3.20}$$

in which $|\vec{k}| = (k^2 + m^2)^{1/2}$. In the case illustrated by Fig. 3.4, the induced flow is a vertically translating squared Gaussian. A parcel at a fixed point in space accelerates rightward as the leading edge of the wave packet approaches and then decelerates as the squared Gaussian flow passes, but overall is displaced rightward as given by the vertical integral of u_2.

Now being aware that a modulated 1D wave packet induces a flow that translates vertically with the wave packet, it is anticipated that this flow, if sufficiently large, could act significantly to Doppler shift the waves, just as a time-independent background shear flow can act to cause wave reflection or breaking near a critical level. This is indeed the case. As a crude heuristic, an estimate for the critical amplitude at which this Doppler shifting might force the waves to overturn is given by the condition for "self-acceleration", which assumes the waves break if the maximum of the induced flow exceeds the horizontal group velocity of the waves. The critical amplitude for self-acceleration is $A_{\rm SA} = \sqrt{2}\,m/|\vec{k}|$, which is plotted in Fig. 3.2a.

In a more rigorous examination, we note that the effect of a background horizontal flow, U, acting upon waves is given by the advection operator $U\partial_x$. So, in the absence of other influences, the evolution of the amplitude envelope due to the leading-order effect of Doppler shifting of the waves is represented by $\partial_t A = -\imath k U A$. Including

the effects of the vertical translation of the wave packet at the group velocity as well as the dispersion of the waves, which can be important at this order, the evolution of the amplitude envelope of a wave packet as influenced by the flow it induces is given by

$$\partial_t A = -c_{gz}\partial_z A + \imath\frac{1}{2}\omega_{mm}\partial_{zz}A - \imath\frac{1}{2}Nk|\vec{k}||A|^2 A. \tag{3.21}$$

This is a nonlinear Schrödinger (NLS) equation (normally written in a frame translating with the wave packet at its vertical group velocity, in which case the first term on the right-hand side disappears and z is replaced with $\tilde{z} = z - c_{gz}t$). An example of the solution of the NLS equation for a modulationally unstable wave packet is shown in Fig. 3.5.

The NLS equation predicts whether the amplitude initially grows or decays depending upon the product of the sign of the induced flow and the sign of $\omega_{mm} = \partial_m c_{gz}$: modulational stability occurs if $U\omega_{mm} > 0$ (the group velocity increases with increasing wavenumber); otherwise, the wave packet is modulationally unstable. (For the general theory, see Whitham 1974 or Sect. 4.2.4 of Sutherland 2010.) For non-rotating internal waves, the maximum upward group velocity occurs for waves with $m = m_c = -k/\sqrt{2}$. For larger m (with smaller magnitude), c_{gz} is smaller and

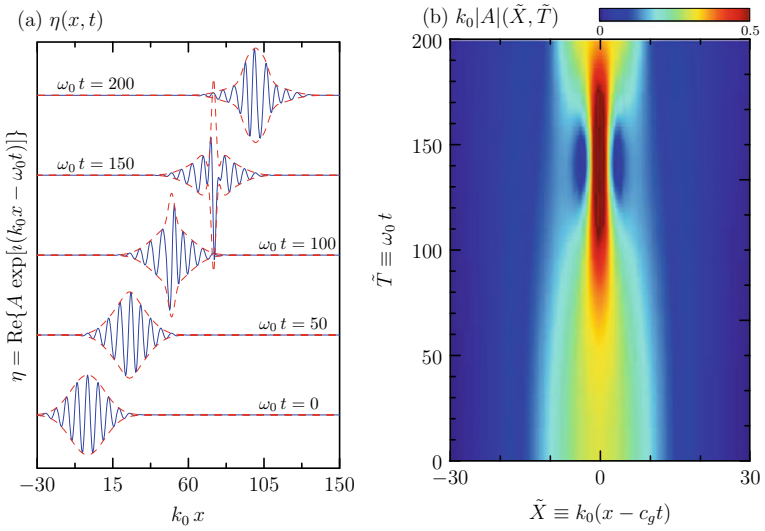

Fig. 3.5 Evolution of a modulationally unstable Gaussian wave packet showing (**a**) the displacement due to waves (solid blue lines) and the amplitude envelope (dashed red lines) at five different times during the evolution as indicated and (**b**) the evolution of the amplitude envelope in a frame moving with the group velocity of the wave packet, with magnitude indicated by the color scale. Note that after the initial amplitude growth the wave packet then broadens and its amplitude decays. Over longer times the growth and decay process repeats. (Adapted with permission from Fig. 4.4 of Sutherland (2010))

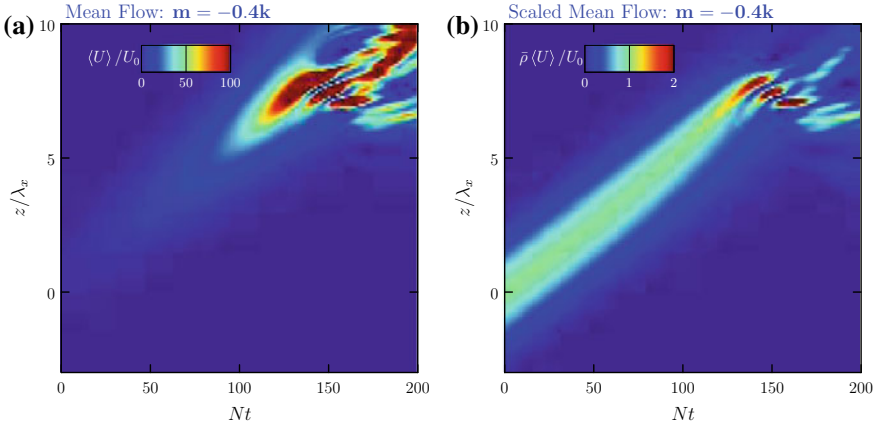

Fig. 3.6 Breakdown of an anelastic nonlinear 1D packet showing (**a**) induced flow that grows exponentially with height, (**b**) induced momentum that would be unchanging in the absence of weakly nonlinear effects

so $\omega_{mm} < 0$: the waves are modulationally unstable. Conversely, more hydrostatic waves with $|m| > k/\sqrt{2}$ are modulationally stable.

The physics of modulational stability and instability are clear by considering the effect of the induced flow that Doppler shifts the waves. For non-hydrostatic waves with $|m/k| < 1/\sqrt{2}$, Doppler shifting acts to reduce the effective frequency of the waves which, in turn, reduces their vertical group velocity. Thus, the trailing edge of the wave packet catches up with the leading edge causing the amplitude to increase while the vertical extent of the packet decreases. On the other hand, if $|m/k| > 1/\sqrt{2}$ then the effective decrease in the wave frequency leads to an increase in the vertical group velocity causing the wave packet to spread vertically and its amplitude to decrease faster than would occur due to linear dispersion alone.

Although the NLS equation predicts that a modulationally unstable wave packet will periodically narrow and then spread (see Fig. 3.5), in reality other nonlinear effects may come into play as the amplitude peaks. An example is shown in Fig. 3.6 illustrating the evolution of the induced flow associated with an anelastic wave packet. As the wave packet narrows and peaks, the wave packet becomes convectively unstable. Although this is predicted by linear theory to happen for a 1D anelastic wave packet, the addition of the weakly nonlinear effect of modulational instability shows that breaking occurs at much lower altitudes (Dosser and Sutherland 2011).

Conversely, modulationally stable 1D anelastic wave packets spread as they grow in amplitude and weakly nonlinear effects become important. Thus, overturning is retarded and simulations show that they break at much higher altitudes than predicted by linear theory. The overturning heights found in simulations are compared with those predicted by linear theory in Fig. 3.7.

What has been presented so far relates to 1D wave packets whose amplitude envelope varies spatially only in the z-direction. The structure of the flow changes

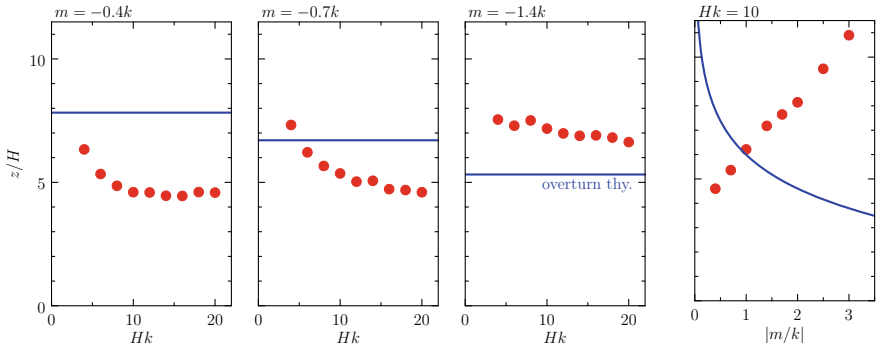

Fig. 3.7 Overturning heights of 1D anelastic wave packets measured in fully nonlinear numerical simulations and compared with theory, showing the altitude of overturning anelastic waves predicted by linear theory (solid blue lines) and fully nonlinear numerical simulation results for the altitude of the first occurrence of overturning (red dots). (Copyright © American Meteorological Society. Adapted with permission from Fig. 6 of Dosser and Sutherland 2011)

qualitatively for wave packets that are modulated in both the x- and z-directions. In this case, the induced flow resulting from the divergence of the momentum flux is itself horizontally divergent and so an order amplitude-squared pressure gradient is established to ensure the fluid remains incompressible. The result is that a spanwise infinite wave packet that is otherwise horizontally and vertically localized induces a flow in the form of a long wave provided the frequency of the long wave is larger than the Coriolis frequency (Bretherton 1969; Tabaei and Akylas 2007; van den Bremer and Sutherland 2014). Unlike the induced flow for 1D wave packets, this flow is positive over the leading flank of the wave packet and is negative over the trailing flank. Thus, whatever the wavenumber of the waves in the wave packet, the waves are always modulationally unstable with the leading edge narrowing and peaking if $|m/k| < 1/\sqrt{2}$ and the trailing edge narrowing and peaking otherwise. Evidently from numerical simulations of 2D anelastic wave packets, this results in overturning occurring at altitudes not too different from those predicted by linear theory (Gervais et al. 2018).

The flow induced by 3D wave packets is entirely different again. In this case, provided the spanwise extent of the wave packet is not too wide, the response to the horizontal divergence of the momentum flux is to create a circulation that goes horizontally around the wave packet in what is termed the Bretherton flow (Bretherton 1969; Tabaei and Akylas 2007; Bühler 2014; van den Bremer and Sutherland 2018). The induced flow over the extent of the wave packet is unidirectional as in the case of 1D wave packets, although the magnitude of the flow is smaller. Thus, while the effects of modulational instability and stability are again anticipated, their influence is expected to be not so pronounced for 3D as for 1D wave packets. Examination of these effects is currently under investigation.

Future Directions

Here we have presented a brief overview of some of the instability mechanisms associated with internal waves in uniformly stratified fluid. While plane-periodic internal waves are an exact solution of the fully nonlinear Euler equations, their stability properties are by no means trivial. Even at small amplitudes, periodic waves, modes, and beams can eventually break down due to resonant-triad wave interactions. If, as in the atmosphere, the waves grow sufficiently rapidly with height that TRI can be ignored, then the waves can break either due to convection or shear instability. And the height at which this breakdown occurs can be preconditioned by the weakly nonlinear effects of modulational stability and instability.

Despite interest in internal waves for their momentum transport in the atmosphere and their energy transport in the ocean, several fundamental aspects of their instability properties remain to be explored. Of these, this author believes the most important avenues for exploration include studying the influence of nonuniform stratification and spatial confinement upon TRI and examining the influence of background rotation upon wave-induced flows and their corresponding weakly nonlinear influence upon the modulational stability/instability and ultimate breaking of wave packets.

References

Benielli, D., & Sommeria, J. (1998). Excitation and breaking of internal gravity waves by parametric instability. *Journal of Fluid Mechanics*, *374*, 117–144.

Bourget, B., Dauxois, T., Joubaud, S., & Odier, P. (2013). Experimental study of parametric subharmonic instability for internal plane waves. *Journal of Fluid Mechanics*, *723*, 1–20.

Bouruet-Aubertot, P., Sommeria, J., & Staquet, C. (1995). Instabilities and breaking of standing internal gravity waves. *Journal of Fluid Mechanics*, *285*, 265–301.

Bühler, O. (2014). *Waves and mean flows* (2nd ed.). Cambridge: Cambridge University Press.

Bretherton, F. P. (1969). Momentum transport by gravity waves. *Quarterly Journal Royal Meteorological Society*, *95*(404), 213–243.

Chalamalla, V. K., & Sarkar, S. (2016). PSI in the case of internal wave beam reflection at a uniform slope. *Journal of Fluid Mechanics*, *789*, 347–367.

Danioux, E., Vanneste, J., & Bühler, O. (2015). On the concentration of near-inertial waves in anticyclones. *Journal of Fluid Mechanics*, *773*, R2. https://doi.org/10.1017/jfm.2015.252.

Dauxois, T., Joubaud, S., Odier, P., & Venaille, A. (2018). Instabilities of internal gravity wave beams. *Annual Reviews of Fluid Mechanics*, *50*, 131–156.

Dosser, H. V., & Sutherland, B. R. (2011). Anelastic internal wavepacket evolution and stability. *Journal of the Atmospheric Science*, *68*, 2844–2859.

Gervais, A., Swaters, G. E., van den Bremer, T. S., & Sutherland, B. R. (2018). Evolution and stability of two-dimensional anelastic internal gravity wavepackets. *Journal of the Atmospheric Sciences*, *75*, 3703–3724. https://doi.org/10.1175/JAS-D-17-0388.1.

Hasselmann, K. (1967). A criterion for non-linear wave stability. *Journal of Fluid Mechanics*, *30*, 737–739.

Joubaud, S., Munroe, J., Odier, P., & Dauxois, T. (2012). Experimental parametric subharmonic instability in stratified fluids. *Physics of Fluids*, *24*, 041703.

Karimi, H. H., & Akylas, T. R. (2014). Parametric subharmonic instability of internal waves: Locally confined beams versus monochromatic wavetrains. *Journal of Fluid Mechanics*, *757*, 381–402.

Klostermeyer, J. (1991). Two-dimensional and three-dimensional parametric instabilities in finite amplitude internal gravity waves. *Geophysical Astrophysical Fluid Dynamics*, *61*, 1–25.
Lindzen, R. S. (1981). Turbulence and stress owing to gravity wave and tidal breakdown. *Journal of Geophysical Research*, *86*, 9707–9714.
Lombard, P. N., & Riley, J. J. (1996). On the breakdown into turbulence of propagating internal waves. *Dynamics of Atmospheres and Oceans*, *23*, 345–355.
Marshall, D. P., Ambaum, M. H. P., Maddison, J. R., Munday, D. R., & Novak, L. (2017). Eddy saturation and frictional control of the Antarctic circumpolar current. *Geophysical Research Letters*, *44*(1), 286–292. https://doi.org/10.1002/2016gl071702.
Mied, R. R. (1976). The occurrence of parametric instabilities in finite-amplitude internal gravity waves. *Journal of Fluid Mechanics*, *78*, 763–784.
Phillips, O. M. (1981). Wave interactions - the evolution of an idea. *Journal of Fluid Mechanics*, *106*, 215–227.
Staquet, C., & Sommeria, J. (2002). Internal gravity waves: From instabilities to turbulence. *Annual Review of Fluid Mechanics*, *34*, 559–593.
Sutherland, B. R. (2001). Finite-amplitude internal wavepacket dispersion and breaking. *Journal of Fluid Mechanics*, *429*, 343–380.
Sutherland, B. R. (2010). *Internal gravity waves*. Cambridge: Cambridge University Press.
Sutherland, B. R., Achatz, U., Caulfield, C. P., & Klymak, J. M. (2019). Recent progress in modeling imbalance in the atmosphere and ocean. *Physical Review Fluids*, *4*(010501), 1–22. https://doi.org/10.1103/PhysRevFluids.4.010501.
Tabaei, A., & Akylas, T. R. (2007). Resonant long-short wave interactions in an unbounded rotating stratified fluid. *Studies in Applied Mathematics*, *119*, 271–296.
Trossman, D. S., Arbic, B. K., Garner, S. T., Goff, J. A., Jayne, S. R., Metzger, E. J., et al. (2013). Impact of parameterized lee wave drag on the energy budget of an eddying global ocean model. *Ocean Modelling*, *72*, 119–142. https://doi.org/10.1016/j.ocemod.2013.08.006.
van den Bremer, T. S., & Sutherland, B. R. (2014). The mean flow and long waves induced by two-dimensional internal gravity wavepackets. *Physics of Fluids*, *26*(106601), 1–23. https://doi.org/10.1063/1.4899262.
van den Bremer, T. S., & Sutherland, B. R. (2018). The wave-induced flow of internal gravity wavepackets with arbitrary aspect ratio. *Journal of Fluid Mechanics*, *834*, 385–408. https://doi.org/10.1017/jfm.2017.745.
Whitham, G. B. (1974). *Linear and nonlinear waves*. New York: Wiley.

inner core at its current size. However, powering the geodynamo happens to be more problematic when the inner core is smaller, and before its nucleation. With a low core thermal conductivity and $Q_{\mathrm{cmb}}^{\mathrm{ad}} = 5$ TW, the convective power P_a would be of a few tens of TW. Driving the geodynamo with thermal convection seems therefore possible, though the convective power would be much lower than at present. Whether this would have a significant impact on the large-scale part of the geomagnetic field remains an open question. If the high estimates of the core thermal conductivity are correct, the CMB heat flux may well be sub-adiabatic. In this situation thermal convection is not possible, and driving the dynamo requires another source of motion and energy. Possible additional sources of energy include exsolution of light elements from the core (O'Rourke and Stevenson 2016; Badro et al. 2016; O'Rourke et al. 2017) and astronomical forcing (Andrault et al. 2016). In addition, adding some radioactive heating in the core (possible due to ^{40}K) would help by decreasing the rate of cooling of the core and increasing the age of the inner core (Labrosse 2015).

Inner Core Dynamics

The Earth's inner core is the deepest layer of our planet: a 1221 km-radius sphere of solid iron-alloy surrounded by molten metal. Its existence was unknown until the first observations of seismic reflexions at the inner core boundary by Inge Lehmann, in one of the shortest-title paper ever: P' (Lehmann 1936). The arrivals of P-waves in the core shadow zone, where P-waves are refracted away by the presence of the 3600-km-radius core, have been explained by the existence of a new discontinuity inside the core, the inner core boundary.

Since these first observations, the study of seismic waves travelling through the inner core and normal modes sampling the deepest layers have provided a blurry image of the inner core structure (Fig. 5.14). Birch (1940) and Jacobs (1953) have proposed that the inner core is a solid sphere of the same metal constituting the outer core, while the actual solidity has been demonstrated only several years later by Dziewonski and Gilbert (1971). Poupinet et al. (1983) were the first to note the different propagation velocities of waves travelling parallel to the rotation axis and perpendicular to it. This anisotropy of seismic properties has since been extensively studied, demonstrating the existence of a complex structure of the inner core. Among the most robust and surprising features of the inner core structure, we can cite two: a strong anisotropy for the bulk of the inner core, and an uppermost layer of the inner core with a strong hemispherical dichotomy in P-waves velocity, but no detectable anisotropy.

The existence of anisotropy in the inner core is an evidence for crystal orientation within the bulk of the inner core (iron crystals being elastically anisotropic). Such crystal orientation is the main motivation for studying flows in the inner core, as lattice-preferred orientation (LPO) may be deformation-induced (Karato 2012). Thus, it is thought that the observed structure may be an evidence for flows within the inner core, likely to be combined with initial crystallisation-induced LPO.

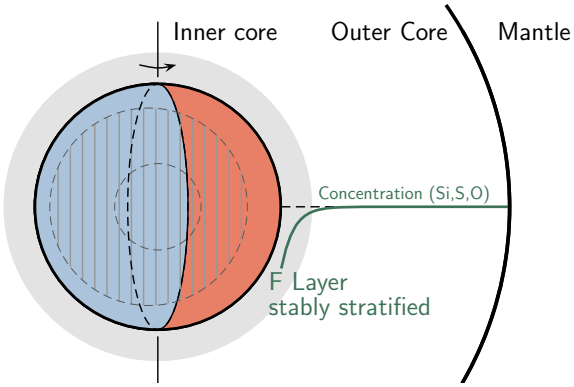

Fig. 5.14 A schematic view of the structure of the inner core. In addition to a global elastic anisotropy oriented parallel to the axis of rotation of the Earth (grey lines), the inner core has radial and horizontal variations of its seismic properties. There is a strong asymmetry between its western and eastern hemispheres (approximately defined by the Greenwich meridian), which have different seismic waves propagation velocity, attenuation, and degree of anisotropy. Anisotropy is weak or non-existent near the surface of the inner core, and increases in depth. Finally, the inner core is surrounded by a layer that appears to be stably stratified, the F-layer

We will discuss here the constitutive equations and some of the aspects of inner core dynamics, focusing on the flow forced in the inner core by the magnetic field diffused from the outer core.

Constitutive Equations

We consider an incompressible fluid in a spherical domain of radius $r_{\rm icb}$, with a Newtonian rheology and uniform viscosity η. Neglecting inertia and rotation, the equation of continuity and the conservation of momentum are written as

$$\nabla \cdot \mathbf{u} = 0, \tag{5.156}$$

$$\mathbf{0} = -\nabla p' + \frac{\eta}{\rho_s}\nabla^2 \mathbf{u} + \mathbf{F}, \tag{5.157}$$

where $\mathbf{F}$ denotes volume forces, p' is the dynamic pressure (including gravity potential) and $\mathbf{u}$ the velocity field.

Among the volume forces, the buoyancy force is written as $\mathbf{F}_{\rm buoyancy} = \Delta\rho \mathbf{g}$, where $\Delta\rho$ is the density difference compared to a neutral density profile and $\mathbf{g} = g_{\rm icb} r/r_{\rm icb}\mathbf{e}_r$ the acceleration of gravity. $g_{\rm icb}$ is the acceleration of gravity at the surface of the inner core.

In this model, the density variations only play a role in the buoyancy term, and they can be related to variations in temperature or concentration in light elements (Si, S, O, ...) compared to a reference state. We take as the reference temperature profile the adiabatic temperature profile $T_{\rm ad}(r)$ anchored at the melting temperature at the radius of the inner core $r_{\rm icb}$. The deviation of the temperature field compared to this reference profile is the potential temperature $\Theta = T - T_{\rm ad}$. The potential composition field is defined as $C = c^s - c^s_{\rm icb}$, where c^s is the concentration of light elements in the inner core and $c^s_{\rm icb}$ its value at the inner core boundary. The density variations are thus $\rho\alpha_T\Theta$ or $\rho\alpha_C C$ for respectively thermal or compositional stratification, where α_T and α_C are the thermal and compositional expansion coefficients. As both potential temperature and potential composition are solutions of an advection–diffusion equation and are both set to zero by construction at the inner core boundary, we will consider a general equation for a quantity χ, representing either of these quantities. χ is solution of

$$\frac{\partial \chi}{\partial t} + \mathbf{u}\cdot\boldsymbol{\nabla}\chi = \kappa_\chi \nabla^2\chi + S_\chi(t), \tag{5.158}$$

where κ_χ is the diffusivity and $S\chi(t)$ a source term built from the evolution of the reference profile as

$$S_T = \kappa_T \nabla^2 T_{\rm ad} - \frac{\partial T_{\rm ad}}{\partial t}, \tag{5.159}$$

$$S_C = -\frac{dc^s_{\rm icb}}{dt}. \tag{5.160}$$

The continuity and momentum equations can be solved using a poloidal–toroidal decomposition of the velocity field $\mathbf{u} = \nabla\times(T\mathbf{r}) + \nabla\times\nabla\times(P\mathbf{r})$, where $\mathbf{r} = r\mathbf{e}_r$ is the position vector and T and P respectively the toroidal and poloidal components. In the following, we will only consider boundary conditions with a zero vertical vorticity and volume forces without toroidal components. The flow is thus expected to have only non-zero poloidal component, and applying $\mathbf{r}\cdot(\nabla\times\nabla\times)$ to Eq. (5.157), we obtain

$$0 = -(\nabla^2)L^2 P + \mathbf{r}\cdot(\nabla\times\nabla\times\mathbf{F}), \tag{5.161}$$

where L^2 is the Laplace horizontal operator defined as

$$L^2 = -\frac{1}{\sin\theta}\frac{\partial}{\partial\theta}\left(\sin\theta\frac{\partial}{\partial\theta}\right) - \frac{1}{\sin^2\theta}\frac{\partial^2}{\partial\phi^2}. \tag{5.162}$$

One could note that for a volume force of the form $\mathbf{F} = F_r r\mathbf{e}_r$ such as the buoyancy forces, the second term of the right-hand side of the equation simplifies as $\mathbf{r}\cdot(\nabla\times\nabla\times\mathbf{F}) = L^2 F_r$. Splitting the volume force term as one term for the buoyancy forces and one term for the other forces, we have $\mathbf{F} = \rho\alpha_\chi\chi r g_{\rm icb}\mathbf{e}_r/r_{\rm icb} + \mathbf{F}_{\rm volume}$. Expanding the scalar fields P and χ with horizontal spherical harmonics Y_l^m satisfying $L^2 Y_l^m = -l(l+1)Y_l^m$ of degree l and order m, as $P = \sum_{l,m} P_l^m Y_l^m$ and

$\chi = \sum_{l,m} \chi_l^m Y_l^m$, the equation of interest is eventually written for each (l, m) as

$$\mathrm{D}_l^2 P_l^m - \rho \alpha_\chi g_{\mathrm{icb}} \frac{r}{r_{\mathrm{icb}}} \chi_l^m - \frac{f_l^m}{l(l+1)} = 0, \tag{5.163}$$

where f_l^m is the spherical harmonics decomposition of the poloidal component of the volume force $\mathbf{F}$, and D_l a second-order differential operator defined as

$$\mathrm{D}_l = \frac{\mathrm{d}}{\mathrm{d}r^2} + \frac{2}{r}\frac{\mathrm{d}}{\mathrm{d}r} - \frac{l(l+1)}{r^2}. \tag{5.164}$$

Boundary Conditions

The inner core boundary is a crystallisation front, where the iron-alloy of the outer core freezes due to the slow secular cooling of our planet. Its exact position is determined by the intersection of the melting temperature profile of the iron-alloy and the temperature profile in the core. Any solid material pushed dynamically further from this intersection would melt, while any liquid pushed inward would freeze. The timescale τ_ϕ involved in the freezing or melting of a small topography at the inner core boundary can be estimated from the timescale needed by outer core convection to extract the latent heat released by crystallisation. We note h the topography at the inner core boundary.

From continuity of stress at the ICB, the mechanical boundary conditions are written at $r = r_{\mathrm{icb}}(t)$. We consider that the dynamical topography h is small (compared to the horizontal wavelength) and that the vector normal to the boundary is close to the radial unit vector. The tangential and normal components of the stress tensor are written as

$$\tau_{r\theta} = \eta \left[r \frac{\partial}{\partial r}\left(\frac{u_\theta}{r}\right) + \frac{1}{r}\frac{\partial u_r}{\partial \theta} \right], \tag{5.165}$$

$$\tau_{r\phi} = \eta \left[r \frac{\partial}{\partial r}\left(\frac{u_\phi}{r}\right) + \frac{1}{r \sin\theta}\frac{\partial u_r}{\partial \phi} \right], \tag{5.166}$$

$$\tau_{rr} = 2\eta \frac{\partial u_r}{\partial r} - p, \tag{5.167}$$

where p here is the total pressure. The viscosity of the outer core being much smaller than the viscosity of the inner core, we can assume tangential stress-free conditions. The boundary conditions are then written as $\tau_{r\theta}(r = r_{\mathrm{icb}}) = \tau_{r\phi}(r = r_{\mathrm{icb}}) = 0$ and continuity of τ_{rr} across the ICB, which for a small topography amounts to state that the normal stress on the inner core side at $r = r_{\mathrm{icb}}$ is equilibrated by the weight of the topography:

$$\underbrace{2\eta\frac{\partial u_r}{\partial r} - p'}_{\text{normal stress}} = \underbrace{\Delta\rho g h}_{\substack{\text{topography}\\ \text{weight}}}, \tag{5.168}$$

p' being the dynamical pressure on the inner core side of the ICB.

To close the system of equations, we consider the time evolution of the topography. The topography can be formed by deformation of the inner core boundary by the underlying flow $u_r - \dot{r}_{\text{icb}}$ and is eroded by phase change, such that we can write that $\mathrm{D}h/\mathrm{D}t = u_r - \dot{r}_{\text{icb}} + V_r$, where V_r is the velocity of phase change in the radial direction. V_r at first order is $-h/\tau_\phi$, where τ_ϕ is a typical timescale for the phase change. Considering a dynamical equilibrium for the topography, we obtain $u_r - \dot{r}_{\text{icb}} = h/\tau_\phi$ and the continuity of normal stress is written as

$$-\Delta\rho g_{\text{icb}}\tau_\phi(u_r - \dot{r}_{\text{icb}}) - 2\eta\frac{\partial u_r}{\partial r} + p' = 0. \tag{5.169}$$

Non-dimensionalisation and Final Set of Equations

The governing equations are made dimensionless using characteristic scales for time, length, velocity, pressure and χ (potential temperature or composition) as, respectively, the diffusion time $r_{\text{icb}}^2/(6\kappa_\chi)$, its radius r_{icb}, $\kappa_\chi/r_{\text{icb}}$, $\eta\kappa_\chi/r_{\text{icb}}^2$ and $S_\chi r_{\text{icb}}^2/(6\kappa)$. Using the same symbols for dimensionless quantities, the non-dimensional set of equations is

$$\boldsymbol{\nabla}\cdot\mathbf{u} = 0, \tag{5.170}$$

$$-\boldsymbol{\nabla}p' + Ra\,\chi\,\mathbf{r} + \boldsymbol{\nabla}^2\mathbf{u} + \mathbf{F}_{\text{volume}} = 0, \tag{5.171}$$

$$\frac{\partial\chi}{\partial t} = \nabla^2\chi - \mathbf{u}\cdot\boldsymbol{\nabla}\chi + 6. \tag{5.172}$$

The dimensionless number Ra is a Rayleigh number expressed as

$$Ra = \frac{\alpha_\chi\rho g_{\text{icb}} S_\chi r_{\text{icb}}^5}{6\kappa_\chi^2\eta}. \tag{5.173}$$

The momentum equation (5.171) can also be written for the poloidal decomposition in spherical harmonics as

$$\mathrm{D}_l^2 P_l^m - Ra\,\chi_l^m - \frac{f_l^m}{l(l+1)} = 0. \tag{5.174}$$

The last step is to express the boundary conditions in term of the poloidal decomposition and in non-dimensional form. Noting that $u_r = L^2 P/r$ and that the horizontal

integration of the momentum equation taken at $r = 1$ gives $-p' + \partial(r\nabla^2 P)/\partial r =$ cste, the stress free condition takes the form

$$\frac{\mathrm{d}^2 P_l^m}{\mathrm{d}r^2} + [l(l+1) - 2]\frac{P_l^m}{r^2} = 0, \tag{5.175}$$

and the normal stress balance is

$$r^2 \frac{\mathrm{d}^3 P_l^m}{\mathrm{d}r^3} - 3l(l+1)\frac{\mathrm{d}P_l^m}{\mathrm{d}r} = \left[l(l+1)\mathcal{P} - \frac{6}{r}\right] P_l^m, \tag{5.176}$$

where $\mathcal{P}$ is a dimensionless number comparing the timescale of viscous relaxation of the boundary $\eta/\Delta\rho g_{\mathrm{icb}} r_{\mathrm{icb}}$ and the time scale of phase change τ_ϕ, *de facto* quantifying the permeability of the inner core boundary. It is defined as

$$\mathcal{P} = \frac{\Delta\rho g_{\mathrm{icb}} r_{\mathrm{icb}} \tau_\phi}{\eta}. \tag{5.177}$$

Unstable or Stable Stratification in the Inner Core?

The core crystallises from the center outward because the solidification temperature of the core mixture increases with depth faster than the (adiabatic) core geotherm (Jacobs 1953). One consequence of this solidification mode is that the inner core is cooled from above, a configuration which is potentially prone to thermal convection. Thermal convection further requires the inner core temperature profile to be super-adiabatic, which depends on a competition between extraction of the inner core internal heat by diffusion and advection, and cooling at the ICB. Equation (5.158) shows that super-adiabaticity in the inner core (i.e. a potential temperature increasing with depth) requires S_T to be positive. Fast cooling and a low inner core thermal diffusivity ($S_T > 0$) promotes super-adiabaticity; slow cooling and high thermal diffusivity ($S_T < 0$) results in a stable thermal stratification.

The expression of S_T (Eq. 5.159) can be rewritten by writing the time derivative of the temperature at the ICB as a function of the rate of inner core growth (Deguen and Cardin 2011). This gives

$$S_T = -\frac{1}{r_{\mathrm{icb}}}\left.\frac{\mathrm{d}T_{\mathrm{ad}}}{\mathrm{d}r}\right|_{\mathrm{icb}} \left(\left[\frac{\mathrm{d}T_s}{\mathrm{d}T_{\mathrm{ad}}} - 1\right] r_{\mathrm{icb}}\dot{r}_{\mathrm{icb}} - 3\kappa_T\right), \tag{5.178}$$

where $\mathrm{d}T_s/\mathrm{d}T_{\mathrm{ad}}$ is the ratio of the Clapeyron slope to the adiabat. It is then straightforward that the term S_T is positive only if

$$\frac{dr_{\mathrm{icb}}^2}{dt} > \frac{6\kappa_T}{\dfrac{\mathrm{d}T_s}{\mathrm{d}T_{\mathrm{ad}}} - 1}. \tag{5.179}$$

Unfortunately, the uncertainties on the thermal conductivity and inner core growth rate are such that the sign of S_T is not known with much certainty. The high value of the thermal conductivity currently favoured (de Koker et al. 2012; Pozzo et al. 2012; Gomi et al. 2013, 2016) results in a stable thermal stratification.

The inner core may also have developed a compositional stratification. The concentration in light elements of newly crystallised solid, c^s_{icb}, is linked through the partition coefficient D to the concentration in the liquid from which it crystallises, c^l_{icb}, as

$$c^s_{\mathrm{icb}} = D c^l_{\mathrm{icb}}, \tag{5.180}$$

while its derivative with respect to inner core size is

$$\frac{dc^s_{\mathrm{icb}}}{dr_{\mathrm{icb}}} = D\frac{dc^l_{\mathrm{icb}}}{dr_{\mathrm{icb}}} + c^l_{\mathrm{icb}}\frac{dD}{dr_{\mathrm{icb}}}, \tag{5.181}$$

$$= Dc^l_{\mathrm{icb}}\left[\frac{d\ln c^l_{\mathrm{icb}}}{dr_{\mathrm{icb}}} + \frac{d\ln D}{dr_{\mathrm{icb}}}\right]. \tag{5.182}$$

A stable compositional stratification would develop if c^s_{icb} increases with increasing inner core size (more light elements in the upper part of the inner core); conversely, an unstable stratification would develop if c^s_{icb} decreases with increasing inner core size. The first term on the right-hand-side term of Eq. (5.182) is very likely positive, due to the gradual enrichment of the outer core in light elements expelled during crystallisation. The second term depends on how D varies with pressure and temperature along the (P, T) path defined by the evolution of the position of the inner core boundary. Ab initio calculations (Gubbins et al. 2013) suggest that it is negative, and of the same order of magnitude as the first term on the r.h.s. of Eq. (5.182). The relative importance of the two terms depends on the exact composition of the inner core (Gubbins et al. 2013; Labrosse 2014), which is not very well constrained. Again, it is difficult to be definitive: given our current knowledge of the composition of the core and of the partitioning behaviour of its light elements, stable and unstable compositional stratifications seem equally plausible.

Natural (thermal or compositional) convection in the inner core has been studied in details (e.g. Weber and Machetel 1992; Wenk et al. 2000; Alboussière et al. 2010; Monnereau et al. 2010; Deguen and Cardin 2011; Cottaar and Buffett 2012; Deguen et al. 2013; Mizzon and Monnereau 2013; Deguen et al. 2018). In the limit $\mathcal{P} \to 0$, the convection instability takes the form of a translation of the inner core, with melting on one hemisphere and solidification on the other (Alboussière et al. 2010; Monnereau et al. 2010; Deguen et al. 2013; Mizzon and Monnereau 2013; Deguen et al. 2018). We will focus here on the case of neutral or stable stratification, and consider the flow forced by the Lorentz force associated with the magnetic field diffused in the inner core from the outer core.

Deformation Induced by the Lorentz Force

As discussed in section "The Geodynamo Hypothesis", the flow in the outer core sustains a magnetic field extending upward to the surface of the Earth but also inward inside the inner core. The magnetic Reynolds number of the inner core is likely small: assuming, for example, a velocity 10^{-10} m.s^{-1} gives a magnetic Reynolds number on the order of 10^{-5}. This shows that the magnetic field is only diffused inside the inner core, with no net advection or generation of the field. A diffused magnetic field in the inner core will add two terms in the set of equations: the Lorentz force in the momentum equation, and Joule heating in the energy equation. We are interested here in the flow driven by the Lorentz force in the inner core (Lasbleis et al. 2015).

Geodynamo simulations often exhibits a strong toroidal magnetic field close to the inner core boundary. As we are interested in the largest effect on the inner core dynamics, we consider here only low-order toroidal components of the magnetic field at the ICB, which have the largest penetration length scale.

We thus add in the momentum equation the Lorentz force due to a purely toroidal and axisymmetric magnetic field of degree two at the ICB $\mathbf{B}|_{\rm icb} = B_0 \sin\theta\cos\theta\mathbf{e}_\phi$ (Buffett and Bloxham 2000). Imposing this field at the ICB and solving for its diffusion inside the inner core assuming it does not vary with time ($\boldsymbol{\nabla}^2\mathbf{B} = 0$), we obtain $\mathbf{B} = B_0 r^2/r_{\rm icb}^2 \cos\theta\sin\theta\mathbf{e}_\phi$. This field is associated to an electric current density $\mathbf{j} = \frac{1}{\mu_0}\boldsymbol{\nabla}\times\mathbf{B}$, with μ_0 the magnetic permeability. The associated Lorentz force is $\mathbf{f}_L = \mathbf{j}\times\mathbf{B}$ which non-potential part (magnetic tension) can be written as

$$\tilde{\mathbf{f}}_L = \frac{B_0^2}{\mu_0 r_{\rm icb}}\frac{r^3}{r_{\rm icb}^3}\left[f_r\mathbf{e}_r + f_\theta\mathbf{e}_\theta\right], \tag{5.183}$$

with f_r and f_θ two functions of θ expressed as

$$f_r(\theta) = 3\cos^4\theta - \frac{15}{7}\cos^2\theta + \frac{4}{35}, \tag{5.184}$$

$$f_\theta(\theta) = \cos\theta\sin\theta\left(\frac{4}{7} - 3\cos^2\theta\right). \tag{5.185}$$

Injecting this force into the dimensionless Stokes equation, we obtain

$$\mathbf{0} = -\boldsymbol{\nabla}p + Ra\,\chi\,\mathbf{r} + \boldsymbol{\nabla}^2\mathbf{u} + M\tilde{\mathbf{f}}_L, \tag{5.186}$$

where

$$M = \frac{B_0^2 r_{\rm icb}^2}{\mu_0\eta\kappa} \tag{5.187}$$

is similar to a Hartmann number, quantifying the ratio of the Lorentz force to the viscous force, and $\tilde{\mathbf{f}}_L$ is defined as in (5.183) without the prefactor $\frac{B_0^2}{\mu_0 r_{\rm icb}}$.

Equation (5.186) is solved using a poloidal decomposition and horizontal spherical harmonics decomposition. The term corresponding to the Lorentz force gives

$$\mathbf{r} \cdot (\boldsymbol{\nabla} \times \boldsymbol{\nabla} \times \tilde{\mathbf{f}}_L) = 8r^2(1 - 3\cos^2\theta) = -\frac{16}{\sqrt{5}} r^2 Y_2^0, \tag{5.188}$$

where $Y_2^0 = \sqrt{5}(3\cos^2\theta - 1)/2$. The momentum equation can thus be written as an equation for the spherical harmonics components P_l^m and t_l^m of respectively the poloidal component of the velocity and the temperature as

$$D_l^2 P_l^m - Ra\, t_l^m + \frac{16}{\sqrt{5}l(l+1)} M r^2 \delta_{2l}\delta_{0m} = 0, \quad l \geq 1, \tag{5.189}$$

where δ is the Kronecker symbol.

Neutral Stratification

We first consider the neutral stratification end-member where $Ra = 0$. In that case, the only force driving flows in the system is the Lorentz force, and we do not need to solve for the temperature or composition fields. The flow results from a balance between the Lorentz and viscous forces. Since the characteristic length scale of velocity variations must be the size of the inner core (1 in dimensionless form), we have

$$\underbrace{\nabla^2 \mathbf{u}}_{\sim u} \sim \underbrace{M\tilde{\mathbf{f}}_L}_{\sim M}, \tag{5.190}$$

which implies that the magnitude of the velocity field should be proportional to M.

We can now solve analytically the flow field for a neutral stratification. With $Ra = 0$, Eq. (5.189) reduces for $l = 2$ and $m = 0$ to

$$D_2^2 P_l^m + \frac{8}{3\sqrt{5}} M r^2 = 0, \tag{5.191}$$

which we solve with the boundary conditions at $r = 1$ described in section "Boundary Conditions":

$$\frac{\mathrm{d}^2 P_2^0}{\mathrm{d}r} + 4\frac{P_2^0}{r^2} = 0, \tag{5.192}$$

$$r\frac{\mathrm{d}r^3 P_2^0}{\mathrm{d}r^3} - 18\frac{1}{r}\frac{\mathrm{d}P_2^0}{\mathrm{d}r} = \left(\mathcal{P} - \frac{1}{r^2}\right) 6P_2^0. \tag{5.193}$$

Equation (5.191) is a fourth order non-homogeneous differential equation, which solution can be obtained by solving the homogeneous equation and noticing that

$$P_2^0 = -\frac{1}{3^3 7\sqrt{5}} M r^6 \tag{5.194}$$

is one solution of the complete equation. Searching for a polynomial solution, we find that r^α is solution of the homogeneous equation $D_2^2 P_2^0 = 0$ if α is a zero of the polynomial expression $[\alpha(\alpha+1)-6][(\alpha-2)(\alpha-1)-6]$. We then obtain the general solution of equation (5.191) as

$$P_2^0(r) = -\frac{M}{3^3 7\sqrt{5}} r^6 + A r^{-3} + B r^{-1} + C r^2 + D r^4. \tag{5.195}$$

A and B must be equal to 0 for the velocity to remain finite at $r = 0$. C and D are obtained from the boundary conditions at $r = 1$, and we finally obtain

$$P_2^0(r) = \frac{1}{3^3 7\sqrt{5}} M \left(-r^6 + \frac{14}{5} r^4 - \frac{9}{5} r^2 + \frac{1}{19 + 5\mathcal{P}} \left[\frac{204}{5} r^4 - \frac{544}{5} r^2 \right] \right). \tag{5.196}$$

From the expression of P_2^0, we can now obtain the expressions for the velocity field from

$$u_r = 3 \frac{P_2^0}{r} Y_2^0, \tag{5.197}$$

$$u_\theta = \frac{1}{r} \frac{d}{dr} (r\, P_2^0) \frac{\partial Y_2^0}{\partial \theta}. \tag{5.198}$$

Defining the r.m.s. velocity as

$$V_{\text{rms}}^2 = \frac{3}{4\pi} \int_0^{2\pi} \int_0^{\pi} \int_0^1 (u_r^2 + u_\theta^2) \sin\theta r^2 \, dr \, d\theta \, d\phi, \tag{5.199}$$

we obtain

$$V_{\text{rms}} = M \frac{4}{189} \sqrt{\frac{34}{715}} \frac{\sqrt{74029 - 1576\, P + 76\, P^2}}{19 + 5\, P}. \tag{5.200}$$

This expression for the RMS velocity gives insight on the effect of $\mathcal{P}$ on the global dynamics. As predicted at the beginning of the subsection, the velocity is indeed a linear function of M, with the boundary conditions modifying the prefactor. For $\mathcal{P} \to 0$, $V_{\text{RMS}} \sim 0.066M$, and for $\mathcal{P} \to \infty$, $V_{\text{RMS}} \sim 0.008M$. Permeable boundary conditions ($\mathcal{P} \to 0$) give velocities about one order of magnitude higher than impermeable boundary conditions ($\mathcal{P} \to \infty$) (Fig. 5.15).

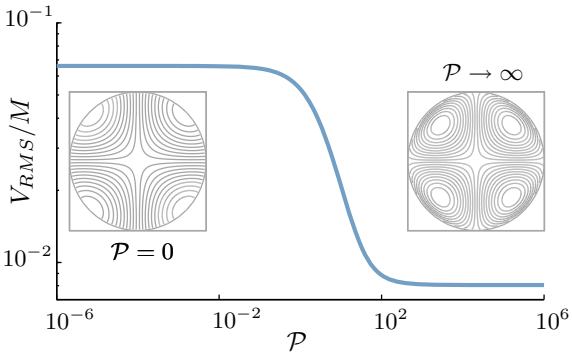

Fig. 5.15 Neutral stratification: r.m.s. velocity as a function of the parameter $\mathcal{P}$, and meridional cross-section of the streamlines of the two end-members $\mathcal{P} \to 0$ and $\mathcal{P} \to \infty$. (Modified from Lasbleis et al. (2015).)

Stable Stratification

If the inner core is stably stratified ($Ra < 0$), the buoyancy forces resulting from the deformation of constant density surfaces would tend to oppose further deformation, and inhibit vertical motions. We can thus anticipate that the flow obtained in the limit of $Ra = 0$ can be significantly altered by a strong stratification.

To estimate to what extent the neutral stratification solution can be altered by the presence of a stable density stratification, we consider the vorticity equation (obtained by taking the curl of Eq. (5.186)), which is

$$\mathbf{0} = -Ra\frac{\partial \chi}{\partial \theta}\mathbf{e}_\phi + M\boldsymbol{\nabla} \times \tilde{\mathbf{f}}_L + \boldsymbol{\nabla}^2\boldsymbol{\zeta}, \tag{5.201}$$

where $\boldsymbol{\zeta} = \boldsymbol{\nabla} \times \mathbf{u}$ is the vorticity. Because the form of the magnetic field considered here forces a degree 2 flow, and because in non-dimensional form χ varies between 0 and 1, the θ derivative of χ is $\lesssim 1$. The magnitude of the baroclinic vorticity production $-Ra\frac{\partial \chi}{\partial \theta}$ is therefore $\lesssim -Ra$. Since the vorticity production associated with the Lorentz force is on the order of M, a stable stratification can affect significantly the flow only if $-Ra \gtrsim M$. As one of the main unknown for inner core dynamics is the viscosity, it is interesting to note that the ratio M/Ra,

$$\frac{M}{Ra} = \frac{B_0^2}{\mu_0 \Delta\rho\, g_{\text{icb}}\, r_{\text{icb}}}, \tag{5.202}$$

does not depend on the viscosity, so that the boundary between a strongly stratified regime and a neutral stratification does not depends on the viscosity.

Figure 5.16 shows the temperature and vorticity fields obtained by solving numerically Eqs. (5.172) and (5.189) at $M = 10^4$ and $Ra = -10^4$, -6×10^4, -10^5, and -10^6. The stratification has a negligible effect on the flow at $Ra = -10^4$, but already has a significant effect at $Ra = -6 \times 10^4$, which is consistent with the criterion we just derived ($-Ra \gtrsim M$ for a strong effect of the stratification). At $Ra = -10^5$ and -10^6, the flow induced by the Lorentz force is essentially con-

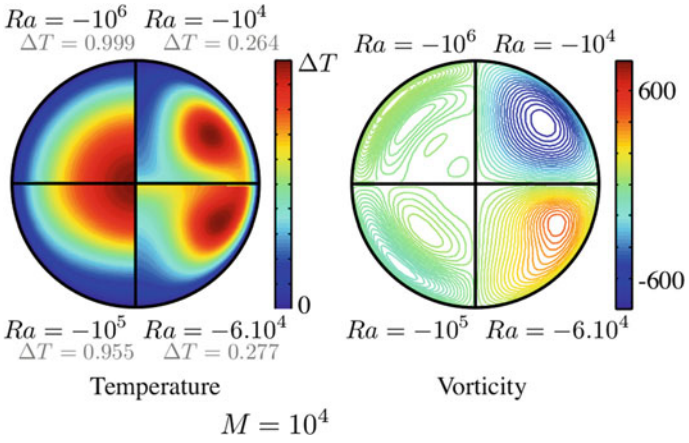

Fig. 5.16 Meridional cross-sections of the temperature and the vorticity fields for $M = 10^4$ and four different values of the Rayleigh number. At low Ra, the flow is similar to the neutral stratification case. If $-Ra \gtrsim M$ (strong stratification) the flow is confined in a layer at the top of the inner core. (Modified from Lasbleis et al. (2015).)

fined to a thin layer below the inner core boundary, in which the flow direction is essentially horizontal. Lasbleis et al. (2015) found that the thickness of this layer is $\propto (-Ra)^{-1/6}$ and the strain rate in the layer is $\propto M(-Ra)^{-1/3}$. For application to Earth's inner core, we take $\Delta\rho \sim -1$ kg.m^{-3} and $B_0 \sim 4$ mT (Gillet et al. 2010), and find $M/(-Ra) \sim 10^6$, which would imply that stratification strongly affects the flow forced by the Lorentz force.

Core Formation

The final section of this chapter concerns the formation of Earth's core. The Earth formed about 4.56 Gy ago through the accretion of solar nebula material, a process which is estimated to have taken a few tens of millions of years. Accretion in the solar system went through different dynamical phases which involved increasingly energetic and catastrophic impacts and collisions (Lunine et al. 2011; Walsh et al. 2011). The last phase of accretion, in which most of the Earth mass was accreted, involved extremely energetic collisions between already differentiated planetary embryos (∼100–1000 km size), which resulted in widespread melting and the formation of magma oceans.

The basic ingredients of a terrestrial planet—an iron-rich metal and silicates—are immiscible, and can separate under the action of gravity to form an iron-rich core surrounded by a rocky mantle. The timescale of phase separation is much smaller than the accretion timescale if at least one of the two phases is liquid, and it is thus believed that core formation has been concomitant with Earth's accretion. Importantly, the metal added to the Earth by each impact had no reason to be in thermodynamic equilibrium with the silicate mantle of the growing Earth, which implies that heat

and chemical elements would have been transferred from one phase to the other when the two phases were in contact. Chemical elements and heat released during accretion have thus been partitioned between the core and mantle, in a way which depends on the exact physical mechanism by which metal and silicate have separated.

This has important implications for the state of the planet at the end of its accretion, and its subsequent evolution. The partitioning between core and mantle of the heat released during accretion has set the initial temperature contrast between the mantle and core, a key parameter for the early dynamics of the planet, with implications for the possibility of forming a basal magma ocean (Labrosse et al. 2007), the existence of an early dynamo (Williams and Nimmo 2004; Monteux et al. 2011), and the subsequent thermal and magnetic evolution of the planet. The partitioning of chemical elements between the core and mantle has been used to constrain the timing of differentiation and the physical conditions under which it occurred (e.g. Yin et al. 2002; Halliday 2004; Wood et al. 2006; Rudge et al. 2010). It has also important implications for a number of geodynamical issues. One example is the identity and abundance of light elements and radioactive elements in the core (Corgne et al. 2007; Badro 2015), which depend on the conditions (pressure P, temperature T, oxygen fugacity fO_2) at which metal and silicate have interacted for the last time.

The large impacts which dominated the last stages of Earth formation injected enormous amounts of kinetic energy into the magma oceans, creating highly turbulent environments in which it has been conjectured that the cores of the bodies impacting the Earth would fragment down to centimetre scale, at which metal and silicates can efficiently exchange chemical elements and heat (Stevenson 1990; Karato and Rama Murthy 1997; Rubie et al. 2003). The metal is envisioned to disperse in the magma ocean and equilibrate with the silicates, before raining out. It would then collect at the base of the magma ocean, and finally migrate toward the core as large diapirs (Stevenson 1990; Karato and Rama Murthy 1997; Monteux et al. 2009; Samuel et al. 2010) or by the propagation of iron dykes (Stevenson 2003), at which point further chemical equilibration is unlikely to be significant.

Most geochemical models of core formation are based on this so-called *iron rain* scenario, but the fluid dynamics involved is actually poorly understood, even at a qualitative level. Efficient chemical exchange requires a high metal–silicates interfacial area-to-volume ratio, which requires fragmentation or stretching of the metal down to ∼cm size. Differentiation of terrestrial bodies started early, and it is now recognised that most of the mass of the Earth was accreted from already differentiated planetary bodies, with cores of their own. Whether or not these large volumes of iron (∼100–1000 km) would indeed fragment down to cm scale at which chemical equilibration can occurs therefore remains an open question, and a matter of much speculation (Dahl and Stevenson 2010; Deguen et al. 2011; Samuel 2012; Deguen et al. 2014; Wacheul et al. 2014).

We have yet no well-tested and self-consistent theory of fragmentation and thermal or compositional equilibration in the context of metal–silicate separation in a magma ocean. For this reason, we have here made the choice of focusing on the basic concepts and mechanisms which we believe are important to know and understand to tackle this problem, rather than trying to give a definitive answer to this question.

Problem Set-Up and Non-dimensional Numbers

To keep things reasonably simple, we will ignore here the dynamics of the impact itself and consider the fate of an initially spherical mass of molten iron falling into silicates, which can be either solid or molten. This molten iron mass may be either the core of a planetary body impacting the Earth or a fragment of the core if it has been significantly dispersed by the impact. As an additional simplifying hypothesis, we will even assume that the metal mass has no initial velocity.

The volume of molten iron is assumed to be close to spherical, and has a radius R_0. We denote by ρ_m and $\rho_s = \rho_m - \Delta\rho$ the densities of metal and silicates, and by η_m and η_s their viscosities. The metal and silicates phases are immiscible and we denote by γ the interfacial tension of the metal–silicates interface. We denote by g the acceleration of gravity.

The evolution of the metal mass depends on seven dimensional parameters (R_0, ρ_m, ρ_s, η_m, η_s, γ) involving 3 fundamental units (length, weight, and time). According to Vashy-Buckingham's theorem, the number of independent non-dimensional numbers to be used to describe the problem is equal to $7 - 3 = 4$. One possible set is the following:

$$\text{Bond number: } Bo = \frac{\Delta\rho\, g\, R_0^2}{\gamma}, \tag{5.203}$$

$$\text{Grashof number: } Gr = \frac{\Delta\rho}{\rho_s}\frac{g R_0^3}{\nu_s^2}, \tag{5.204}$$

$$\text{density ratio: } \frac{\rho_m}{\rho_s}, \tag{5.205}$$

$$\text{viscosity ratio: } \frac{\eta_m}{\eta_s}. \tag{5.206}$$

The Bond number is a measure of the relative importance of buoyancy and interfacial tension. The Grashof number is basically a Reynolds number obtained by taking Stokes' velocity as a velocity scale. Additional useful numbers include Reynolds and Weber numbers, which can be defined as

$$\text{Reynolds number: } Re = \frac{\rho_s U R_0}{\eta_s}, \tag{5.207}$$

$$\text{Weber number: } We = \frac{\rho_s U^2 R_0}{\gamma}, \tag{5.208}$$

where U is a velocity scale to be defined. The Reynolds and Weber numbers compare inertia to viscous forces and interfacial tension, respectively. The density ratio is close to 2.

If, in addition, we consider heat or mass transfer between metal and silicates, then two additional dimensional parameters enter the problem: the diffusivities (thermal or compositional) κ_m and κ_s in the metal and silicates. Since there is no additional

fundamental units, Vashy-Buckingham's theorem implies that two additional non-dimensional numbers must be used. One possible choice is to use the ratio of the diffusivities and a Péclet number:

$$\text{diffusivity ratio: } \frac{\kappa_m}{\kappa_s}, \tag{5.209}$$

$$\text{Péclet number: } Pe = \frac{U R_0}{\kappa_s}. \tag{5.210}$$

In what follows, we will assume that $\kappa_s = \kappa_m$ for the sake of simplicity.

Preliminary Considerations

Terminal Velocity

Since we have chosen to focus on the case of a metal mass falling with no initial velocity, a relevant velocity scale is its terminal velocity, reached when the buoyancy force ($\sim \Delta\rho g R_0^3$) is balanced by the drag on the surface of the metal mass. Two different scalings can be obtained depending on whether the drag is dominated by viscous stresses ($\sim \eta_s U/R_0$) or dynamic pressure ($\sim \rho_s U^2$). The ratio of the dynamic pressure and viscous stresses contributions to the total drag is

$$\frac{\text{dynamic pressure}}{\text{viscous stress}} \sim \frac{\rho_s U^2}{\eta_s U/R_0} = Re. \tag{5.211}$$

The drag on the metal mass is obtained by multiplying the dominant stress by the surface area of the metal mass: it is on the order of $\eta_s U R_0$ if the drag is dominated by the contribution of viscous stresses (low Re), and on the order of $\sim \rho_s U^2 R_0^2$ if it is dominated by the contribution of dynamic pressure (high Re). The force balance on the metal mass can thus be written as

$$\underbrace{\Delta\rho g R_0^3}_{\text{buoyancy}} \sim \underbrace{\max\left(\rho_s U^2 R_0^2, \eta_s U R_0\right)}_{\text{drag}}. \tag{5.212}$$

The terminal velocity obtained from this balance is

$$U \sim \min\left(\frac{\Delta\rho g R_0^2}{\eta_s}, \left(\frac{\Delta\rho}{\rho_s} g R_0\right)^{1/2}\right). \tag{5.213}$$

The first scaling gives Stokes' settling velocity, and corresponds to the low Re limit; the second scaling is the so-called newtonian scaling, and corresponds to the high Re limit. The two velocities are on the same order of magnitude when

$$Gr \sim 1, \tag{5.214}$$

which defines the boundary between the two scalings (here $\nu_s = \eta_s/\rho_s$). The terminal velocity is thus

$$U \sim \frac{\Delta\rho g R_0^2}{\eta_s} \quad \text{if } Gr \ll 1, \tag{5.215}$$

$$U \sim \left(\frac{\Delta\rho}{\rho_s} g R_0\right)^{1/2} \quad \text{if } Gr \gg 1. \tag{5.216}$$

With these scalings, the Reynolds and Weber numbers based on the terminal velocity are given by

$$\begin{cases} Re & \sim Gr \\ We & \sim Gr\,Bo \end{cases} \quad \text{if } Gr \ll 1, \tag{5.217}$$

$$\begin{cases} Re & \sim Gr^{1/2} \\ We & \sim Bo \end{cases} \quad \text{if } Gr \gg 1. \tag{5.218}$$

Maximal Stable Size of a Falling Drop

Interfacial tension (unit $\mathrm{J.m^{-2}}$) can be interpreted as an energy per unit area. Deforming an interface in a way which results in an increase of the interfacial area costs energy, and interfacial tension effects will tend to minimise the surface area of the interface. If no other force acts on a drop, interfacial tension would keep it spherical, hence minimising its surface area.

Interfacial tension can also be seen as a force per unit of length (it can be verified that $\mathrm{J.m^{-2}} = \mathrm{N.m^{-1}}$): if a piece of an interface is divided into two parts, the force imparted by one part of the surface on the other is parallel to the interface and has a magnitude given by the product of the interfacial tension with the length of the curve separating the two parts of the surface. If integrated over a curved surface, one can also show that interfacial tension induces a pressure jump across the interface equal to

$$\Delta P = \gamma\left(\frac{1}{R_1} + \frac{1}{R_2}\right), \tag{5.219}$$

where R_1 and R_2 are the principal radii of curvature. This pressure jump is called Laplace's pressure. Across a spherical interface (the surface of a drop or bubble of radius R_0), Laplace's pressure is equal to $2\gamma/R_0$.

A falling drop can be deformed by the stresses imparted by the surrounding fluid onto the drop, or in other words by the fluid drag. If the total drag on the drop is F_{drag}, the mean stress on the surface of the drop is $\sim F_{\mathrm{drag}}/R_0^2$. One can expect significant

deformation of the drop if the hydrodynamic stress variations due to the drag exceed Laplace's pressure:

$$\frac{F_{\text{drag}}}{R_0^2} \gtrsim \frac{\gamma}{R_0}. \tag{5.220}$$

If the drop reached its terminal velocity, then the drag must be equal to the total buoyancy of the drop, $F_{\text{drag}} \sim \Delta\rho g R_0^3$. Combining this with Eqs. (5.220), we find that strong deformation of the drop will happen if its radius is larger than a critical radius R_c given by

$$R_c \sim \left(\frac{\gamma}{\Delta\rho g}\right)^{1/2}. \tag{5.221}$$

This length is also known as a *capillary length*: it is the length scale over which buoyancy effects dominate over surface tension effects. Interfacial tension will keep the drop close to spherical if its radius is smaller than R_c. Equation (5.221) is equivalent to writing that deformation is significant if the Bond number of the drop is large compared to 1. The interfacial tension between metal and silicates is on the order of 1 J.m^{-2} and $\Delta\rho \sim 4000$ kg.m^{-3}. With $g \sim 10$ m.s^{-2}, we thus have $R_c \sim 5$ mm.

Strong drop deformation may happen before reaching terminal velocity, and in this case the above scaling will not be the most relevant. If drag is dominated by viscous effects ($F_{\text{drag}} \sim \eta_s U R_0$), then we find that deformation of the drop may happen if its velocity is larger than a critical velocity

$$U_c \sim \frac{\gamma}{\eta}. \tag{5.222}$$

This criterion is of limited use since if the drag is dominated by viscous effect (which means that $Re \ll 1$), then the drop velocity will very quickly reach a terminal velocity equal to Stokes' settling velocity. Using Stokes' velocity for U in Eq. (5.222) gives Eq. (5.220).

If instead drag is dominated by the contribution of dynamic pressure ($F_{\text{drag}} \sim \rho_s U^2 R_0^2$), then we find that strong deformation requires the drop Weber number is large:

$$We = \frac{\rho_s U^2 R_0}{\gamma} \gtrsim 1. \tag{5.223}$$

This criterion reduces to Eq. (5.221) when the drop reaches its terminal velocity ($U \sim \sqrt{(\Delta\rho/\rho_s) g R_0}$ since in this limit $Re \gg 1$).

The Low Reynolds Limit: Diapirism

A first relevant limit of the problem described in section "Problem Set-Up and Non-dimensional Numbers" corresponds to molten metal diapirs travelling through a solid, or partially molten, silicate layer. The radius of these diapirs may be similar

to the size of the core of the impactors, say somewhere between 1 km and 1000 km. The acceleration of gravity is smaller or equal to its current value in Earth's mantle, $g \sim 10$ m.s^{-2}. The viscosity η_s of the silicates is a strong function of temperature, and can also be significantly decreased if the silicate layer is partially molten. A reasonable range is 10^{15}–10^{21} Pa.s. The viscosity of molten iron is $\sim 10^{-2}$ Pa.s.

With this parameter values, $Bo \gtrsim 10^{10}$, $Gr \lesssim 10^{-4}$, $\rho_m/\rho_s \sim 2$, $\eta_m/\eta_s \lesssim 10^{-18}$. The Grashof number being small, we are well into the low Reynolds regime: viscous forces dominate over inertia in the silicates. The limit of low Re and high Bo has been studied numerically in the context of core formation (Samuel and Tackley 2008; Monteux et al. 2009; Samuel et al. 2010), and experimentally in other contexts (e.g. Ribe 1983; Bercovici and Kelly 1997). In this limit surface tension is unimportant, but the volume of metal is kept roughly spherical because $Re \ll 1$. Since viscous forces are so important in the silicates, the flow around the metal mass is limited to spatial scales on the order of R_0, which limits the deformation of the metal mass (in other words, small scale perturbations of the metal–silicate interface shape are damped viscously).

The falling velocity is thus simply given by Stokes' velocity [Eq. (5.215)]. The law of heat or mass transfer between the diapir and its surrounding is also well known (e.g. Clift et al. 1978; Ribe 2007; Ulvrová et al. 2011: the heat flux is given by

$$\text{heat flux} = a 4\pi R_0^2 k_s \frac{\bar{T} - T_s(z)}{R_0} Pe^{1/2} \tag{5.224}$$

where k_s is the thermal conductivity in the silicates, $\bar{T}$ the mean temperature in the diapir, $T_s(z)$ the temperature of the surrounding silicate layer at depth z, and a is a constant on the order of 1. A similar expression can be written for chemical elements transfer.

The heat balance of the diapir writes

$$\rho_m c_{p,m} \frac{4\pi}{3} R_0^3 \frac{d\bar{T}}{dt} = -4\pi R_0^2 a k_s \frac{\bar{T} - T_s(z)}{R_0} Pe^{1/2}, \tag{5.225}$$

where $c_{p,m}$ is the heat capacity of the metal phase. Transforming the time derivative into a derivative with respect to the distance z travelled by the diapir (using $d(...)/dt = U d(...)/dz$) and re-arranging gives

$$\frac{d\bar{T}}{dz} + \frac{\bar{T}}{\ell} = \frac{T_s(z)}{\ell}, \tag{5.226}$$

where the characteristic length ℓ is given by

$$\ell = \frac{1}{3\,a} \frac{\rho_m c_{p,m}}{\rho_s c_{p,s}} R_0 Pe^{1/2}. \tag{5.227}$$

ℓ is the characteristic distance over which the temperature of the diapir responds to changes of the surrounding temperature, the *thermal equilibration distance*. The general solution of equation (5.226) is

$$\bar{T} = T_0 \mathrm{e}^{-z/\ell} + \int_0^z \frac{\mathrm{e}^{(z'-z)/\ell}}{\ell} T_s(z') dz', \tag{5.228}$$

where T_0 is the initial temperature of the diapir. In practice, the amount of heat transfer is small because ℓ is typically larger than the mantle thickness. The compositional diffusivity in the solid silicates being perhaps four orders of magnitude smaller that the thermal diffusivity, exchange of chemical elements would be even smaller (the equilibration distance being $\propto Pe^{1/2} \propto \kappa^{-1/2}$). Diapirs migrating through a solid part of the mantle would therefore exchange a negligible amount of heat and chemical elements with the surrounding mantle.

The High Reynolds Limit: Metal–Silicates Separation in a Magma Ocean

Let us now consider the case of a volume of molten metal falling into molten rocks—a *magma ocean*. The parameter values are similar to what we have considered when discussing the case of diapirism, except that the viscosity of the silicates is much smaller, on the order of 10^{-1} Pa.s. With these parameter values, $Bo \gtrsim 10^{10}$, $Gr \gtrsim 10^{22}$, $\rho_m/\rho_s \sim 2$, $\eta_m/\eta_s \lesssim 10^{-18}$. Since $Gr \gg 1$, the relevant velocity scale is the newtonian scaling given by Eq. (5.216). This gives $Re \sim Gr^{1/2} \gtrsim 10^{11}$ and $We \sim Bo \gtrsim 10^{10}$. The very large values of Re, Bo, and We imply that neither viscous forces nor interfacial tension can keep the metal volume spherical: a molten mass of metal falling into a magma ocean should suffer significant deformation, possibly resulting in its fragmentation into drops.

Observations from Laboratory Experiments

The very large values of the Bond and Weber numbers imply that interfacial tension should be unimportant for the large-scale dynamics. This suggests to first look at the case of infinite Bond and Weber numbers, which corresponds to the limit of miscible fluids.

Figure 5.17a shows snapshots from an experiment in which a negatively buoyant volume of an aqueous solution of sodium iodide is released into fresh water. The volume of the (dyed) negatively buoyant fluid is seen to increase as it falls, which indicates that it entrains and incorporates ambient fluid, resulting in its gradual dilution. Measurements show that the mean radius of the dyed mixture increases linearly with the distance from the point of release. This is what is known as a *turbulent thermal* in the fluid mechanics and atmospheric science communities (e.g. Batchelor

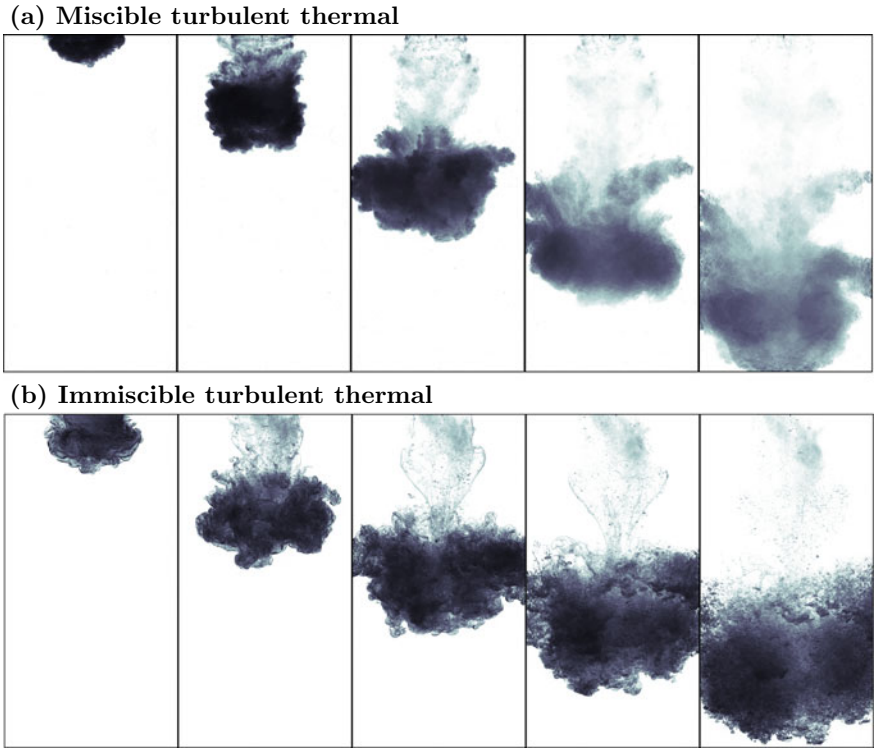

Fig. 5.17 **a** A 169 mL volume of an aqueous solution of NaI ($\rho = 1502$ kg.m^{-3}) falling into fresh water, at Re $= 4 \times 10^4$, $\rho_m/\rho_s = 1.5$, $\eta_m/\eta_s = 1$. The time interval between each image is 0.3 s. **b** A 169 mL volume of an aqueous solution of NaI ($\rho = 1601$ kg.m^{-3}) falling into a low-viscosity silicon oil ($\rho = 821$ kg.m^{-3}, $\eta = 8.2 \times 10^{-4}$ Pa.s), at $Bo = 3.4 \times 10^4$, Re $= 5.5 \times 10^4$, $\rho_m/\rho_s = 1.95$, $\eta_m/\eta_s = 1.2$ (Deguen et al. 2019). The time interval between each image is 0.2 s

1954; Scorer 1957; Woodward 1959). The name *thermal* is inherited from the usage of glider pilots, for whom a thermal is an isolated mass of warm air rising through the lower atmosphere. Though the buoyancy in atmospheric thermals is due to temperature differences, the nature of the source of buoyancy (thermal or compositional) happens to be of secondary importance and introduces no qualitative difference. The term thermal has since been used to denote an isolated buoyant mass of a fluid rising or falling (depending on the sign of the buoyancy), irrespectively of the nature of the source of buoyancy. Here we will also often use the term *buoyant cloud* instead of thermal.

Figure 5.17b shows snapshots from a similar experiment in which a negatively buoyant volume of sodium iodide is now released into a low-viscosity silicon oil. The NaI solution and the silicon oil are *immiscible*, so we are one important step closer to the core-mantle differentiation configuration. The experimental fluids and configuration have been chosen so as to maximise the values of the Bond and

Reynolds numbers, which are $Bo = 3.4 \times 10^4$ and $\mathrm{Re} = 5.5 \times 10^4$. The density ratio is $\rho_m/\rho_s = 1.95$ (close to metal–silicate), and the viscosity ratio is $\eta_m/\eta_s = 1.2$. The large-scale evolution of the negatively buoyant volume is strikingly similar to what has been observed in the *miscible* experiment: the volume of the negatively buoyant fluid increases linearly with distance, which indicates that it entrains and incorporates silicon oil. PIV measurements on a similar experiment (Fig. 5.18) show that the velocity field has a vortex ring structure, with most of the entrainment of silicon oil probably occurring from the rear of the cloud.

In contrast, the small scale structure in the immiscible experiment is qualitatively different from what we can observe in the miscible experiment. In the miscible experiment, the negatively buoyant solutions *mixes* with the entrained water, diffusion of the NaI salt allowing homogenisation at the molecular scale. In the immiscible experiment, the NaI solution of course does not mix with the entrained silicon oil since the two liquids are immiscible. A close inspection of the last snapshot of the immiscible experiment reveals that the dense phase has been fragmented into droplets.

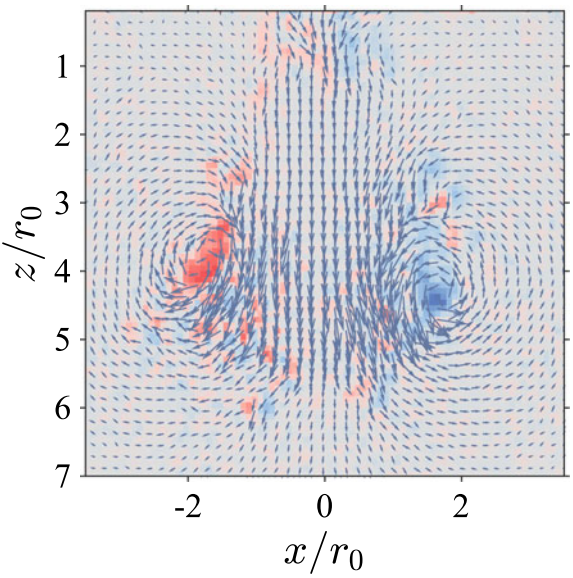

Fig. 5.18 Velocity field obtained from PIV measurements in an experiment in which a 169 mL of aqueous solution of NaI ($\rho = 1280$ kg.m^{-3}) is released in a 1cst viscosity silicon oil. The colorscale gives the vorticity field (red is clockwise, blue counterclockwise). The concentration of the NaI solution has been chosen so that its optical index matches that of the silicon oil, in order to avoid optical distorsion. The non-dimensional parameter values are $\mathrm{Bo} = 2 \times 10^4$, $\mathrm{Re} = 4.2 \times 10^4$, $\rho_m/\rho_s = 1.56$, $\eta_m/\eta_s = 1.2$

Large-Scale Dynamics: Turbulent Entrainment Model

We consider the evolution of a mass of negatively buoyant fluid falling into another one (Fig. 5.19). The mass of negatively buoyant fluid has an initially spherical shape and an initial radius R_0, and has a density $\rho_a + \Delta\rho$, where ρ_a is the density of the surrounding fluid. We denote by u_z the vertical velocity of the center of mass of the negatively buoyant cloud, and by $R(z)$ its spatial extension. Following Batchelor (1954), we assume that far from the source u_z and R only depend on either distance z or time t, and on its total amount of buoyancy defined as

$$B = g\frac{\Delta\rho}{\rho_a}V_0,$$

where V_0 is the initial volume of the released buoyant mass. We thus assume that surface tension has no effect on the evolution of u_z and R. Dimensional analysis then shows that

$$\begin{cases} u_z \sim B^{1/2}z^{-1} \\ R \sim z \end{cases} \quad \text{or, equivalently} \quad \begin{cases} u_z \sim B^{1/4}t^{-1/2} \\ R \sim B^{1/4}t^{1/2} \end{cases},$$

which predicts that the spatial extension of the cloud increases linearly with z: the cloud must therefore entrain ambient fluid. The prediction that the mean velocity decreases as z^{-1}, or, equivalently, as R^{-1}, is consistent with the fact that the total buoyancy of the cloud is conserved, but not its volume. The buoyancy is "diluted" by the incorporation of neutrally buoyant ambient fluid to the cloud.

A more physical (and more general) way to obtain the evolution of a turbulent thermal has been given by Morton et al. (1956), who based their analysis on the assumption that the rate of entrainment of ambient fluid within the buoyant cloud is simply proportional to the mean vertical velocity u_z and to the surface area of the cloud (Fig. 5.19). This is the basic assumption of the *turbulent entrainment* models used to describe the dynamics of turbulent clouds, plumes, and jets.

This assumption implies that the time derivative of the cloud volume is given by

$$\frac{d}{dt}\left(\frac{4\pi}{3}R^3\right) = 4\pi R^2 \alpha u_z, \tag{5.229}$$

where α is the *entrainment coefficient*. Noting that $d(...)/dt = u_z d(...)/dz$, where z is the vertical position of the center of mass of the cloud, integration of equation (5.229) gives

$$R = R_0 + \alpha z, \tag{5.230}$$

which is consistent with the prediction of dimensional analysis.

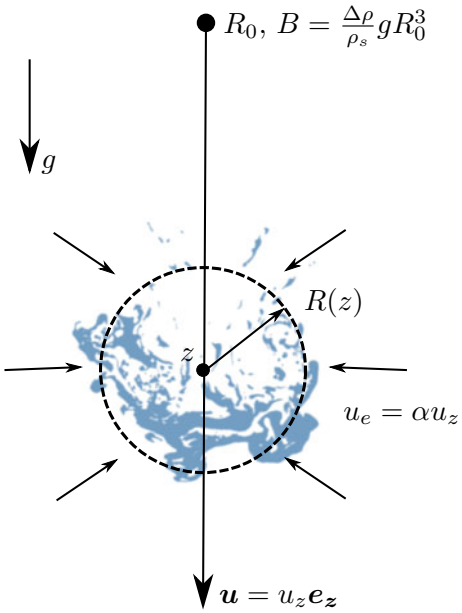

Fig. 5.19 The *turbulent thermal* model: a volume of fluid with initial radius R_0 and density $\rho_a + \Delta\rho$ is released at $z = 0$ in a fluid of density ρ_a. The thermal has a mean vertical velocity u_z. Its mean radius R increases with the distance z from the source due to entrainment of ambient fluid at a rate $u_e = \alpha u_z$

Conservation of momentum allows to obtain a predictive law for the vertical velocity u_z of the center of mass of the cloud. Ignoring fluid drag on the cloud and a possible loss of buoyancy in the wake of the cloud, conservation of momentum simply states that

$$\frac{d}{dt}\left(\frac{4\pi}{3} R^3 \bar{\rho} u_z\right) = \frac{4\pi}{3} R_0^3 \Delta\rho g \tag{5.231}$$

where $\bar{\rho}$ is the mean density of the cloud, given by

$$\bar{\rho} = \rho_a + \Delta\rho \frac{R_0^3}{R^3} = \rho_a + (1 + \alpha z)^{-3} \Delta\rho. \tag{5.232}$$

Conservation of mass implies that

$$\frac{d}{dt}\left(\frac{4\pi}{3} R^3 \bar{\rho}\right) = 4\pi \rho_a R^2 \alpha u_z. \tag{5.233}$$

Using this relation in Eq. (5.231), using the transformation $d(...)/dt = u_z d(...)/dz = \alpha u_z d(...)/dR$, and re-arranging gives

$$\frac{du_z^2}{dR} + \frac{6}{R}\frac{\rho_a}{\bar{\rho}} u_z^2 = \frac{2g}{\alpha}\frac{\Delta\rho}{\bar{\rho}}\frac{R_0^3}{R^3}, \tag{5.234}$$

a linear first order ordinary differential equation with varying coefficients. The solution, written for u_z as a function of z, is

$$u_z = \left(\frac{g}{2\alpha^3}\frac{\Delta\rho}{\rho_a}R_0^3\right)^{1/2}\mathcal{F}\left(\frac{R_0}{\alpha z},\frac{\Delta\rho}{\rho_a}\right)\frac{1}{z}, \tag{5.235}$$

where

$$\mathcal{F}\left(\frac{R_0}{\alpha z},\frac{\Delta\rho}{\rho_a}\right) = \frac{\left[1+4\frac{R_0}{\alpha z}+6\left(\frac{R_0}{\alpha z}\right)^2+4\left(1+\frac{\Delta\rho}{\rho_a}\right)\left(\frac{R_0}{\alpha z}\right)^3\right]^{1/2}}{1+3\frac{R_0}{\alpha z}+3\left(\frac{R_0}{\alpha z}\right)^2+\left(1+\frac{\Delta\rho}{\rho_a}\right)\left(\frac{R_0}{\alpha z}\right)^3}. \tag{5.236}$$

The function $\mathcal{F}$ tends toward 1 at large $\alpha z/R_0$. The full solution is thus consistent with the dimensional analysis prediction when far from the source. Close to the source, the velocity is given (at first order in $\alpha z/R_0$), by

$$u_z = \left(2\frac{\Delta\rho}{\rho_a}gz\right)^{1/2}. \tag{5.237}$$

Though the turbulent thermal model just described has been developed to model *miscible* flows, experiments suggest that it can also be applied to immiscible fluids in situations where the Bond and Weber numbers are large (Deguen et al. 2014; Landeau et al. 2014; Wacheul et al. 2014; Wacheul and Le Bars 2017). A qualitative comparison of Fig. 5.17a, b suggests that it is indeed the case. The similarity between the miscible and immiscible experiments also holds on a quantitative level: from a series of experiments similar to that presented on Fig. 5.17, we have been able to show that the evolution of both R and u_z are very well described by the turbulent entrainment model with $\alpha = 0.25 \pm 0.05$, similar to miscible flows (Deguen et al. 2014; Landeau et al. 2014). This demonstrates that there is indeed no effect of surface tension on the large-scale part of the flow.

Fragmentation

Qualitative Observations form Experiments

In the experiment shown on Fig. 5.17b and in similar experiments, most of the fragmentation of the dense liquid occurs during a relatively short time span. In Fig. 5.17b, the dense phase is essentially continuous until the third snapshot, and almost entirely fragmented into drops at the fourth snapshot. The analysis of images obtained with a high-speed camera (1kHz) shows that drops formation results from two mechanisms:

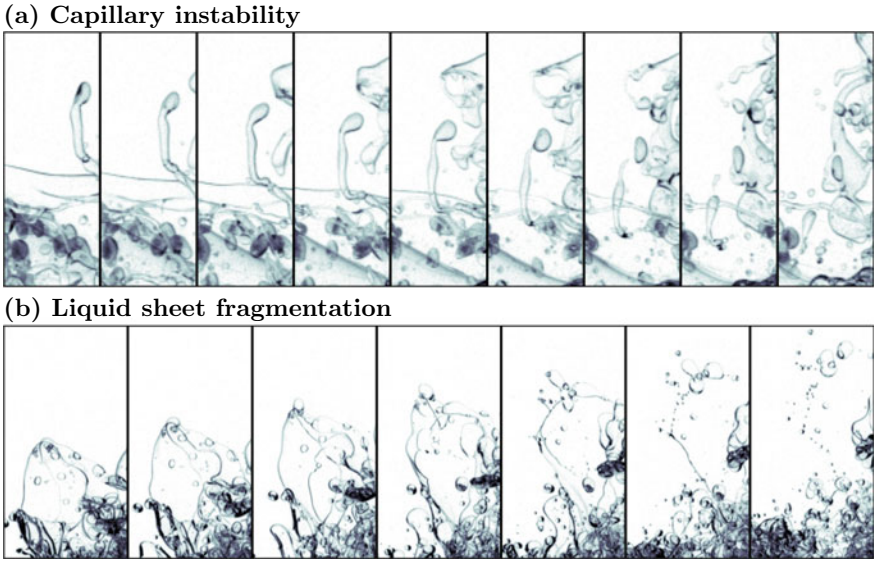

Fig. 5.20 Two fragmentations mechanisms observed in the experiment shown in Fig. 5.17b. **a** Fragmentation of a liquid (NaI solution) ligament. The time interval between two images is $\Delta t = 10$ ms, and the width of each image is 1 cm. **b** Fragmentation of liquid film. The time interval between two images is $\Delta t = 20$ ms, and the width of each image is 1.8 cm

1. the fragmentation of stretched cylindrical ligaments of aqueous solution through the Rayleigh–Plateau capillary instability, as shown in Fig. 5.20a (the mechanism of the Rayleigh–Plateau instability is explained below),
2. the fragmentation of thin liquid films, as shown in Fig. 5.20b. In this regime, thin films of aqueous solutions are stretched by the flow before eventually being punctured. The film then quickly retracts, the liquid forming the film gathering into ligaments which then fragment into drops due to the Rayleigh–Plateau instability.

These two modes of fragmentation are classically observed in fragmentation problems in a variety of contexts. In fact, liquid fragmentation necessitates a capillary instability, irrespectively of the nature of the flow (Villermaux 2007). What varies from one problem to another is the sequence of mechanisms resulting in the formation of ligaments which can fragment as a result of the Rayleigh–Plateau capillary instability. In experiments such as shown in Fig. 5.17b, the observed sequence is the following: (i) the interface is destabilised and deformed by the combined effect of shear and Rayleigh–Taylor instabilities; (ii) three-dimensional structures generated by the destabilisation of the interface are stretched and stirred by the mean flow and velocity field fluctuations; (iii) stirring produces ligaments and films, which will then break up and produce a population of drops.

Rayleigh–Plateau Capillary Instability

In many situations, the deformation of an interface results in an increase of its surface area, and hence of its interfacial energy. In this case deformation is not energetically favoured, and mechanical work therefore has to be provided to deform the interface. This is for example the case of initially planar interface: any perturbation of the interface results in an increase of its surface area and energy.

In contrast, the deformation of a cylindrical interface can, under certain conditions, result in a decrease of its surface area, and hence of its interfacial energy. Take a cylinder of one liquid into another, of length L and radius R_0. Its surface area is $2\pi R_0 L$ and its interfacial energy is $2\pi R_0 L\gamma$. It is easy to see that the cylindrical shape is not very favourable from an energetic point of view: if the liquid of the cylinder is re-arranged to form a sphere of the same volume ($\pi R_0^2 L$), the sphere will have a radius equal to $\left[(3/4)R_0^2 L\right]^{1/3}$, and a surface area equal to $4(3/4)^{2/3}\pi R_0^{4/3} L^{2/3}$, which is smaller than the cylinder surface area if the length of the cylinder is larger than $(9/2)R_0$. This shows that the fragmentation into drops of liquid cylinder is energetically favoured if the ratio of its length and radius is larger than 9/2.

Is fragmentation dynamically possible? To see if it is, let us consider again a liquid cylinder of radius R_0, and assume now that its surface is perturbed from its initial shape as

$$R(x) = \bar{R} + \epsilon \sin\left(2\pi \frac{x}{\lambda}\right), \tag{5.238}$$

where x is the coordinate along the axis of symmetry of the cylinder, and ϵ and λ the amplitude and wavelength of the perturbation (Fig. 5.21). Note that conservation

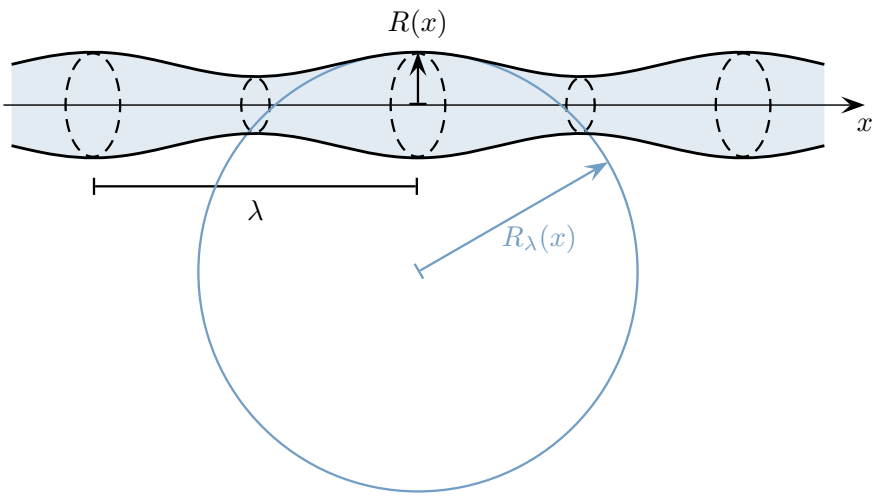

Fig. 5.21 A liquid cylinder (blue) with its surface perturbed by an axisymmetric sinusoidal perturbation

of mass implies that $\bar{R} < R_0$: comparing the volume of a section of length λ of the unperturbed and perturbed states indeed shows that

$$\bar{R} = R_0 \left(1 - \frac{\epsilon^2}{4R_0^2}\right)^{1/2}. \tag{5.239}$$

Calculating the surface area of the perturbed cylinder shows that the perturbation induces a decrease of the surface area (and hence of energy) if $\lambda > 2\pi R_0$, which suggests that the cylindrical shape may be unstable to perturbations with wavelengths larger than $2\pi R_0$.

To see how the instability works, let us consider the two principal curvatures of the interface (Fig. 5.21). One is the curvature associated with the radius of the cylinder, $1/R(x)$, and the other is the curvature associated with the longitudinal perturbation, $1/R_\lambda(x)$, which is equal to the divergence in the x-direction of the normal $\mathbf{n}$ of the interface. The Laplace pressure jump across the interface is equal to

$$\Delta P = \gamma \left(\frac{1}{R(x)} + \frac{1}{R_\lambda(x)}\right). \tag{5.240}$$

The contribution of R_λ is positive where $R > R_0$, and negative where $R < R_0$. It thus produces a pressure gradient from regions of large R to regions of small R, which can drive a flow from large to small R that would decrease the amplitude of the radius perturbation. It thus has a stabilising effect. In contrast, the pressure jump associated with $1/R$ is larger in regions of small R. It thus produces a pressure gradient from small to large R, which may drive a flow that would increase the amplitude of the perturbation. The amplitude of the radius perturbation can therefore grow if the pressure gradient associated with the curvature $R(x)$ is larger in magnitude that the pressure gradient associated with the curvature $R_\lambda(x)$.

At first order in ϵ, one find

$$\frac{1}{R} = \frac{1}{R_0}\left[1 - \frac{\epsilon}{R_0}\sin\left(2\pi\frac{x}{\lambda}\right)\right] + \mathcal{O}(\epsilon^2), \tag{5.241}$$

and

$$\frac{1}{R_\lambda} = \frac{-1}{\sqrt{1 + (dR/dx)^2}}\frac{d^2R}{dx^2} = \frac{4\pi^2}{\lambda^2}\epsilon\sin\left(2\pi\frac{x}{\lambda}\right) + \mathcal{O}(\epsilon^2), \tag{5.242}$$

which gives a pressure jump across the interface given by

$$\Delta P = \gamma\left[\frac{1}{R_0} + \epsilon\left(\frac{4\pi^2}{\lambda^2} - \frac{1}{R_0^2}\right)\sin\left(2\pi\frac{x}{\lambda}\right)\right] + \mathcal{O}(\epsilon^2). \tag{5.243}$$

Its gradient along x is given by

$$\frac{\partial \Delta P}{\partial x} = \epsilon \frac{2\pi}{\lambda}\gamma \left(\frac{4\pi^2}{\lambda^2} - \frac{1}{R_0^2}\right) \cos\left(2\pi \frac{x}{\lambda}\right) + \mathcal{O}(\epsilon^2). \tag{5.244}$$

This shows that the pressure gradient inside the liquid cylinder is from small to large R if $\frac{4\pi^2}{\lambda^2} < \frac{1}{R_0^2}$, and from large to small R instead. In other words, the initial perturbation will grow if

$$\lambda > \lambda_c = 2\pi R_0, \tag{5.245}$$

which will eventually lead to the fragmentation of the cylinder into drops. This dynamical criterion is slightly more restrictive that the energy criterion, since $2\pi \simeq 6.26 > 9/2 = 4.5$.

Things get more complicated in situations where liquid ligaments are deformed and stretched by the ambient flow. Fragmentation can be significantly protracted by stretching effects (Taylor 1934; Tomotika 1936; Mikami et al. 1975; Eggers and Villermaux 2008), which can be understood as follows. Let us consider a stretched ligament, the surface of which is modulated by a longitudinal perturbation of wavelength λ. The stretching will affect the disturbance, which will see its wavelength increase in proportion to the amount of stretching. If the perturbation wavelength initially corresponds to the optimal wavelength for the growth of the capillary instability, increasing the wavelength will decrease the rate of growth of the disturbance.

Chemical and Heat Transfer at the Drop Scale

If the metal phase ends up being fragmented into drops of size equal or smaller than the maximal stable size $R_c \sim \sqrt{\gamma/(\Delta\rho g)}$ [Eq. (5.221)], then thermal and chemical equilibration of the metal phase with the surrounding silicates is not an issue (e.g. Stevenson 1990; Karato and Rama Murthy 1997; Rubie et al. 2003; Ulvrová et al. 2011, as shown below.

One can show (Lherm and Deguen 2018) that the timescale of chemical equilibration of a falling metal drop with its surrounding is given by

$$\tau_{\rm eq} \sim \frac{R^2}{6\kappa_s} D_{\rm m/s} {\rm Pe_s}^{-1/2} \left[1 + \frac{1}{D_{\rm m/s}} \left(\frac{\kappa_s}{\kappa_m}\right)^{1/2}\right], \tag{5.246}$$

where κ_s and κ_m are the compositional diffusivities in the silicates and metal, $D_{\rm m/s}$ the metal/silicates partitioning coefficient of a given chemical element, and $Pe_s = UR/\kappa_s$. The distance $\ell_{\rm eq}$ fallen by the drop during a time $\tau_{\rm eq}$ is given by

$$\ell_{\rm eq} = \tau_{\rm eq} U \sim \frac{R}{6} D_{\rm m/s} {\rm Pe_s}^{1/2} \left[1 + \frac{1}{D_{\rm m/s}} \left(\frac{\kappa_s}{\kappa_m}\right)^{1/2}\right] \tag{5.247}$$

In the case of siderophile elements ($D_{\mathrm{m/s}} \gg 1$), this is approximated by

$$\ell_{\mathrm{eq}} \sim \frac{R}{6} D_{\mathrm{m/s}} \mathrm{Pe_s}^{1/2}. \tag{5.248}$$

For a metal drop falling into a magma ocean, R_c is about 5 mm. The corresponding Grashof number is

$$Gr = \frac{\Delta\rho}{\rho_s} \frac{g R_c^3}{\nu_s^2} \sim \left(\frac{g}{10\,\mathrm{m.s^{-2}}}\right) \times \left(\frac{10^{-2}\,\mathrm{Pa.s}}{\eta_s}\right)^2 \times 10^5. \tag{5.249}$$

Magma ocean viscosity is estimated to be in the range 10^{-3}–10^{-2} Pa.s, which implies that the drop is in the newtonian regime and has a terminal velocity given by $\sim\sqrt{(\Delta\rho/\rho_s g R_c}$. With a compositional diffusivity $\kappa_s \sim 10^{-9}$ m.s^{-2}, this gives a Péclet number around 10^6 and we thus have $(R/6)\mathrm{Pe_s}^{1/2} \simeq 1$ m. Siderophile elements like Nickel or Cobalt have partitioning coefficients $D_{\mathrm{m/s}}$ around 10^3 at low pressure, and as low as $\sim$10 when approaching the pressure of the core-mantle boundary. This would give $\ell_{\mathrm{eq}} \sim 1$ km at low pressure, and $\ell_{\mathrm{eq}} \sim 10$ m at high pressure. This is in both cases much smaller than typical magma ocean depth, which implies that drops of metal a few mm in size will readily equilibrate with the surrounding molten silicates.

However, the above conclusion rests on the assumption that the metal phase fragments into drops of a few mm in radius. We have no well-tested fragmentation model that can be used in the context of core formation, so whether the metal phase would fragment or not is still an open question. It is also possible that efficient equilibration does not require fragmentation of the metal phase. The metal phase would necessarily be intensely stirred and stretched before fragmentation, and this may allow for efficient chemical transfer between the metal and silicates phase (Lherm and Deguen 2018).

Acknowledgements This project has received funding from the European Research Council (ERC) under the European Unions Horizon 2020 research and innovation programme (grant agreement No 716429).

References

Alboussière, T., Deguen, R., & Melzani, M. (2010). Melting induced stratification above the Earth's inner core due to convective translation. *Nature*, *466*, 744–747.

Alfè, D., Gillan, M. J., & Price, G. D. (2000). Constraints on the composition of the Earth's core from ab initio calculations. *Nature*, *405*, 172–175.

Andrault, D., Monteux, J., Le Bars, M., & Samuel, H. (2016). The deep Earth may not be cooling down. *Earth and Planetary Science Letters*, *443*, 195–203.

Badro, J., Fiquet, G., Guyot, F., Gregoryanz, E., Occelli, F., Antonangeli, D., et al. (2007). Effect of light elements on the sound velocities in solid iron: Implications for the composition of Earth's core. *Earth and Planetary Science Letters*, *254*, 233–238.

Badro, J., Brodholt, J. P., Piet, H., Siebert, J., & Ryerson, F. J. (2015). Core formation and core composition from coupled geochemical and geophysical constraints. *Proceedings of the National Academy of Sciences*, *112*(40), 12310–12314.

Badro, J., Siebert, J., & Nimmo, F. (2016). An early geodynamo driven by exsolution of mantle components from Earth's core. *Nature*, *536*(7616), 326–328.

Batchelor, G. K. (1954). Heat convection and buoyancy effects in fluids. *Quarterly Journal of the Royal Meteorological Society*, *80*, 339–358.

Bercovici, D., & Kelly, A. (1997). The non-linear initiation of diapirs and plume heads. *Physics of the Earth and Planetary Interiors*, *101*, 119–130.

Berhanu, M., Monchaux, R., Fauve, S., Mordant, N., Pétrélis, F., Chiffaudel, A., et al. (2007). Magnetic field reversals in an experimental turbulent dynamo. *EPL (Europhysics Letters)*, *77*(5), 59001.

Birch, F. (1940). The alpha-gamma transformation of iron at high pressures, and the problem of the Earth's magnetism. *American Journal of Science*.

Birch, F. (1952). Elasticity and constitution of the Earth's interior. *Journal of Geophysical Research*, *57*, 227.

Birch, F. (1964). Density and composition of mantle and core. *Journal of Geophysical Research*, *69*, 4377.

Bondi, H., & Lyttleton, R. A. (1948). On the dynamical theory of the rotation of the earth: I. the secular retardation of the core. In *Mathematical Proceedings of the Cambridge Philosophical Society* (Vol. 44, pp. 345–359). Cambridge University Press.

Braginsky, S. I. (1963). Structure of the F layer and reasons for convection in the Earth's core. *Doklady Akademii Nauk SSSR English Translation*, *149*, 1311–1314.

Braginsky, S. I. (1970). Torsional magnetohydrodynamics vibrations in the Earth's core and variations in day length. *Geomagnetism and Aeronomy*, *10*, 3–12.

Buffett, B. A. (2002). Estimates of heat flow in the deep mantle based on the power requirements for the geodynamo. *Geophysical Research Letters*, *29*(12), 120000–1.

Buffett, B. A., & Bloxham, J. (2000). Deformation of Earth's inner core by electromagnetic forces. *Geophysical Research Letters*, *27*, 4001–4004.

Buffett, B. A., Huppert, H. E., Lister, J. R., & Woods, A. W. (1996). On the thermal evolution of the Earth's core. *Journal of Geophysical Research*, *101*, 7989–8006.

Bullard, E. (1949). The magnetic field within the Earth. *Proceedings of the Royal Society of London A*, *197*(1051), 433–453.

Bullard, E. (1950). The transfer of heat from the core of the Earth. *Geophysical Journal International*, *6*, 36–41.

Bullard, E., & Gellman, H. (1954). Homogeneous dynamos and terrestrial magnetism. *Philosophical Transactions of the Royal Society of London A*, *247*(928), 213–278.

Busse, F. H. (1970). Thermal instabilities in rapidly rotating systems. *Journal of Fluid Mechanics*, *44*, 441–460.

Cabanes, S., Schaeffer, N., & Nataf, H.-C. (2014). Turbulence reduces magnetic diffusivity in a liquid sodium experiment. *Physical Review Letters*, *113*(18), 184501.

Cheng, J. S., & Aurnou, J. M. (2016). Tests of diffusion-free scaling behaviors in numerical dynamo datasets. *Earth and Planetary Science Letters*, *436*, 121–129.

Christensen, U. R., & Wicht, J. (2015). Numerical dynamo simulations. *Treatise on Geophysics (Second Edition)*, *8*, 245–277.

Christensen, U. R., Aubert, J., & Hulot, G. (2010). Conditions for Earth-like geodynamo models. *Earth and Planetary Science Letters*, *296*(3–4), 487–496.

Christensen, U. R. (2010). Dynamo scaling laws and applications to the planets. *Space Science Reviews*, *152*(1–4), 565–590.

Christensen, U. R., & Aubert, J. (2006). Scaling properties of convection-driven dynamos in rotating spherical shells and application to planetary magnetic fields. *Geophysical Journal International*, *166*(1), 97–114. ISSN 1365-246X.

Christensen, U. R., & Tilgner, A. (2004). Power requirement of the geodynamo from ohmic losses in numerical and laboratory dynamos. *Nature*, *429*, 169–171.
Clift, R., Grace, J. R., & Weber, M. E. (1978). *Bubbles, drops and particles*. New York: Academic Press.
Corgne, A., Keshav, S., Fei, Y., & McDonough, W. F. (2007). How much potassium is in the Earth's core? New insights from partitioning experiments. *Earth and Planetary Science Letters*, *256*, 567–576.
Cottaar, S., & Buffett, B. (2012). Convection in the Earth's inner core. *Physics of the Earth and Planetary Interiors*, *198–199*, 67–78.
Dahl, T. W., & Stevenson, D. J. (2010). Turbulent mixing of metal and silicate during planet accretion—and interpretation of the Hf–W chronometer. *Earth and Planetary Science Letters*, *295*, 177–186.
de Koker, N., Steinle-Neumann, G., & Vlcek, V. (2012). Electrical resistivity and thermal conductivity of liquid Fe alloys at high P and T, and heat flux in Earth's core. *Proceedings of the National Academy of Sciences*, *109*(11), 4070–4073.
Deguen, R. (2012). Structure and dynamics of Earth's inner core. *Earth and Planetary Science Letters*, *333–334*, 211–225.
Deguen, R., & Cardin, P. (2011). Thermo-chemical convection in Earth's inner core. *Geophysical Journal International*, *187*, 1101–1118.
Deguen, R., Olson, P., & Cardin, P. (2011). Experiments on turbulent metal-silicate mixing in a magma ocean. *Earth and Planetary Science Letters*, *310*, 303–313.
Deguen, R., Alboussière, T., & Cardin, P. (2013). Thermal convection in Earth's inner core with phase change at its boundary. *Geophysical Journal International*, *194*(3), 1310–1334.
Deguen, R., Landeau, M., & Olson, P. (2014). Turbulent metal-silicate mixing, fragmentation, and equilibration in magma oceans. *Earth and Planetary Science Letters*, *391*, 274–287.
Deguen, R., Alboussière, T., & Labrosse, S. (2018). Double-diffusive translation of Earth's inner core. *Geophysical Journal International*, *214*(1), 88–107.
Deguen, R., Risso, F., Keita, M. Double-diffusive translation of Earth's inner core, in prep..
Dormy, E., Soward, A. M., Jones, C. A., Jault, D., & Cardin, P. (2004). The onset of thermal convection in rotating spherical shells. *Journal of Fluid Mechanics*, *501*, 43–70.
Dziewonski, A. M., & Gilbert, F. (1971). Solidity of the inner core of the Earth inferred from normal mode observations. *Nature*, *234*, 465–466.
Eggers, J., & Villermaux, E. (2008). Physics of liquid jets. *Reports on Progress in Physics*, *71*(3), 036601.
Gailitis, A., Lielausis, O., Platacis, E., Dement'ev, S., Cifersons, A., Gerbeth, G., et al. (2001). Magnetic field saturation in the riga dynamo experiment. *Physical Review Letters*, *86*(14), 3024.
Gillet, N., Jault, D., Canet, E., & Fournier, A. (2010). Fast torsional waves and strong magnetic field within the Earths core. *Nature*, *465*(7294), 74–77.
Gilman, P. A., & Miller, J. (1981). Dynamically consistent nonlinear dynamos driven by convection in a rotating spherical shell. *The Astrophysical Journal Supplement Series*, *46*, 211–238.
Glatzmaier, G. A. (1984). Numerical simulations of stellar convective dynamos. I. The model and method. *Journal of Computational Physics*, *55*(3), 461–484.
Glatzmaier, G. A. (1985a). Numerical simulations of stellar convective dynamos. II-field propagation in the convection zone. *The Astrophysical Journal*, *291* 300–307.
Glatzmaier, G. A. (1985b). Numerical simulations of stellar convective dynamos III. At the base of the convection zone. *Geophysical & Astrophysical Fluid Dynamics*, **31**(1–2), 137–150.
Glatzmaier, G. A., & Roberts, P. H. (1995). A three-dimensional self-consistent computer simulation of a geomagnetic field reversal. *Nature*, *377*, 203–209. https://doi.org/10.1038/377203a0.
Gomi, H., Ohta, K., Hirose, K., Labrosse, S., Caracas, R., Verstraete, M. J., et al. (2013). The high conductivity of iron and thermal evolution of the Earth's core. *Physics of the Earth and Planetary Interiors*, *224*, 88–103.

Gomi, H., Hirose, K., Akai, H., & Fei, Y. (2016). Electrical resistivity of substitutionally disordered hcp Fe-Si and Fe-Ni alloys: Chemically-induced resistivity saturation in the Earth's core. *Earth and Planetary Science Letters*, *451*, 51–61.

Gubbins, D. (1977). Energetics of the Earth's core. *Journal of Geophysics Zeitschrift Geophysik*, *43*, 453–464.

Gubbins, D., Alfè, D., Masters, G., Price, G. D., & Gillan, M. (2004). Gross thermodynamics of two-component core convection. *Geophysical Journal International*, *157*, 1407–1414.

Gubbins, D., Alfè, D., & Davies, C. J. (2013). Compositional instability of Earth's solid inner core. *Geophysical Research Letters*, *40*, 1–5.

Halliday, A. (2004). Mixing, volatile loss and compositional change during impact-driven accretion of the Earth. *Nature*, *427*(6974), 505–509. ISSN 0028-0836. https://doi.org/10.1038/nature02275.

Herzenberg, A. (1958). Geomagnetic dynamos. *Philosophical Transactions of the Royal Society of London*, *250*(986), 543–583.

Hirose, K., Morard, G., Sinmyo, R., Umemoto, K., Hernlund, J., Helffrich, G., et al. (2017). Crystallization of silicon dioxide and compositional evolution of the Earth's core. *Nature*, *543*(7643), 99.

Holme, R. (2015). Large-scale flow in the core. *Treatise on Geophysics*, *8*, 91–113.

Jacobs, J. A. (1953). The Earth's inner core. *Nature*, *172*, 297.

Jaupart, C., & Mareschal, J.-C. (2010). *Heat generation and transport in the Earth*. Cambridge: Cambridge University Press.

Jephcoat, A., & Olson, P. (1987). Is the inner core of the Earth pure iron? *Nature*, *325*, 332–335.

Jones, C. A. (2011). Planetary magnetic fields and fluid dynamos. *Annual Review of Fluid Mechanics*, *43*, 583–614.

Jones, C. A., Soward, A. M., & Mussa, A. I. (2000). The onset of thermal convection in a rapidly rotating sphere. *Journal of Fluid Mechanics*, *405*, 157–179.

Kageyama, A., Sato, T., & (Complexity Simulation Group) (1995). Computer simulation of a magnetohydrodynamic dynamo. II. *Physics of Plasmas*, *2*(5), 1421–1431.

Karato, S., & Rama Murthy, V. (1997). Core formation and chemical equilibrium in the Earth—I. Physical considerations. *Physics of the Earth and Planetary Interiors*, *100*(1–4), 61–79. ISSN 00319201. https://doi.org/10.1016/S0031-9201(96)03232-3.

Karato, S. (2012). *Deformation of Earth materials: an introduction to the rheology of solid Earth*. Cambridge: Cambridge University Press.

King, E. M., & Buffett, B. A. (2013). Flow speeds and length scales in geodynamo models: The role of viscosity. *Earth and Planetary Science Letters*, *371*, 156–162.

Konôpková, Z., McWilliams, R. S., Gómez-Pérez, N., & Goncharov, A. F. (2016). Direct measurement of thermal conductivity in solid iron at planetary core conditions. *Nature*, *534*(7605), 99–101.

Labrosse, S. (2014). Thermal and compositional stratification of the inner core. *Comptes Rendus Geoscience*, *346*, 119–129.

Labrosse, S. (2015). Thermal evolution of the core with a high thermal conductivity. *Physics of the Earth and Planetary Interiors*, *247*, 36–55.

Labrosse, S., Hernlund, J. W., & Coltice, N. (2007). A crystallizing dense magma ocean at the base of the Earth's mantle. *Nature*, *450*(7171), 866–869. ISSN 0028-0836. https://doi.org/10.1038/nature06355.

Landeau, M., Deguen, R., & Olson, P. (2014). Experiments on the fragmentation of a buoyant liquid volume in another liquid. *Journal of Fluid Mechanics*, *749*, 478–518.

Larmor, J. (1919). How could a rotating body such as the sun become a magnet. *Report of the British Association for the Advancement of Science*, 159–160.

Lasbleis, M., & Deguen, R. (2015). Building a regime diagram for the Earth's inner core. *Physics of the Earth and Planetary Interiors*, *247*, 80–93.

Lasbleis, M., Deguen, R., Cardin, P., & Labrosse, S. (2015). Earth's inner core dynamics induced by the Lorentz force. *Geophysical Journal International*, *202*, 548–563.

Lay, T., Hernlund, J., Garnero, E. J., & Thorne, M. S. (2006). A post-perovskite lens and D"heat flux beneath the central Pacific. *Science*, *314*, 1272–1276.

Lehmann, I. (1936). P'. *Bureau Central Sismologique International*, *14*, 87–115.

Lherm, V., & Deguen, R. (2018). Small-scale metal/silicate equilibration during core formation: The influence of stretching enhanced diffusion on mixing. *Journal of Geophysical Research: Solid Earth*, *123*(12), 10–496.

Lister, J. R. (2003). Expressions for the dissipation driven by convection in the Earth's core. *Physics of the Earth and Planetary Interiors*, *140*, 145–158. https://doi.org/10.1016/S0031-9201(03)00169-9.

Loper, D. E. (1978). The gravitationally powered dynamo. *Geophysical Journal International*, *54*, 389–404.

Lowes, F. J., & Wilkinson, I. (1963). Geomagnetic dynamo: a laboratory model. *Nature (London)*, *198*, 4886.

Lunine, J. I., O'brien, D. P., Raymond, S. N., Morbidelli, A., Quinn, T., & Graps, A. L. (2011). Dynamical models of terrestrial planet formation. *Advanced Science Letters*, *4*(2), 325–338.

Malkus, W. V. R. (1963). Precessional torques as the cause of geomagnetism. *Journal of Geophysical Research*, *68*(10), 2871–2886.

Malkus, W. V. R. (1968). Precession of the Earth as the cause of geomagnetism: Experiments lend support to the proposal that precessional torques drive the Earth's dynamo. *Science*, *160*(3825), 259–264.

Maus, S., Rother, M., Stolle, C., Mai, W., Choi, S., Lühr, H., Cooke, D., & Roth, C. (2006). Third generation of the Potsdam Magnetic Model of the Earth (POMME). *Geochemistry, Geophysics, Geosystems*, *7*(7).

Mikami, T., Cox, R. G., & Mason, S. G. (1975). Breakup of extending liquid threads. *International Journal of Multiphase Flow*, *2*(2), 113–138.

Mizzon, H., & Monnereau, M. (2013). Implication of the lopsided growth for the viscosity of Earth's inner core. *Earth and Planetary Science Letters*, *361*, 391–401.

Monchaux, R., Berhanu, M., Bourgoin, M., Moulin, M., Odier, P., Pinton, J.-F., et al. (2007). Generation of a magnetic field by dynamo action in a turbulent flow of liquid sodium. *Physical Review Letters*, *98*(4), 044502.

Monnereau, M., Calvet, M., Margerin, L., & Souriau, A. (2010). Lopsided growth of Earth's inner core. *Science*, *328*, 1014–1017.

Monteux, J., Ricard, Y., Coltice, N., Dubuffet, F., & Ulvrova, M. (2009). A model of metal–silicate separation on growing planets. *Earth and Planetary Science Letters*, *287*(3–4), 353–362. ISSN 0012821X. https://doi.org/10.1016/j.epsl.2009.08.020.

Monteux, J., Jellinek, A. M., & Johnson, C. L. (2011). Why might planets and moons have early dynamos? *Earth and Planetary Science Letters*, *310*(3), 349–359.

Morton, B. R., Taylor, G., & Turner, J. S. (1956). Turbulent gravitational convection from maintained and instantaneous sources. *Proceedings of the Royal Society of London. Series A, Mathematical and Physical Sciences*, *234*, 1–23.

Nataf, H.-C., & Gagnière, N. (2008). On the peculiar nature of turbulence in planetary dynamos. *Comptes Rendus Physique*, *9*(7), 702–710.

Olson, P. (2013). Experimental dynamos and the dynamics of planetary cores. *Annual Review of Earth and Planetary Sciences*, *41*, 153–181.

Olson, P., & Christensen, U. R. (2006). Dipole moment scaling for convection-driven planetary dynamos. *Earth and Planetary Science Letters*, *250*(3–4), 561–571.

O'Rourke, J. G., & Stevenson, D. J. (2016). Powering Earth's dynamo with magnesium precipitation from the core. *Nature*, *529*(7586), 387–389.

O'Rourke, J. G., Korenaga, J., & Stevenson, D. J. (2017). Thermal evolution of Earth with magnesium precipitation in the core. *Earth and Planetary Science Letters*, *458*, 263–272.

Ponomarenko, Y. B. (1973). Theory of the hydromagnetic generator. *Journal of Applied Mechanics and Technical Physics*, *14*(6), 775–778.

Poupinet, G., Pillet, R., & Souriau, A. (1983). Possible heterogeneity of the Earth's core deduced from PKIKP travel times. *Nature*, *305*, 204–206.
Pozzo, M., Davies, C., Gubbins, D., & Alfè, D. (2012). Thermal and electrical conductivity of iron at Earth's core conditions. *Nature*, *485*, 355–358.
Ribe. N. M. (2007). Analytical Approaches to mantle dynamics. In Schubert, G. (Ed.), *Treatise on geophysics* (Vol. 7).
Ribe, N. M. (1983). Diapirism in the Earth's mantle: Experiments on the motion of a hot sphere in a fluid with temperature dependent viscosity. *Journal of Volcanology and Geothermal Research*, *16*, 221–245.
Ricard, Y. (2007). Physics of mantle convection. In Schubert, G. (Ed.), *Treatise on geophysics* (Vol. 7). Elsevier.
Roberts, P. H. (1968). On the thermal instability of a rotating-fluid sphere containing heat sources. *Philosophical Transactions of the Royal Society of London A*, *263*(1136), 93–117.
Roberts, G. O. (1972). Dynamo action of fluid motions with two-dimensional periodicity. *Philosophical Transactions of the Royal Society of London A*, *271*(1216), 411–454.
Roberts, P. H., Jones, C. A., & Calderwood, A. (2003). Energy fluxes and ohmic dissipation in the Earth's core. In Jones C. A., Soward A. M., & Zhang K. (Eds.), *Earth's core and lower mantle*. Taylor & Francis.
Rubie, D. C., Melosh, H. J., Reid, J. E., Liebske, C., & Righter, K. (2003). Mechanisms of metal–silicate equilibration in the terrestrial magma ocean. *Earth and Planetary Science Letters*, *205*(3–4), 239–255. ISSN 0012821X. https://doi.org/10.1016/S0012-821X(02)01044-0.
Rubie, D. C., Jacobson, S. A., O'Brien, D. P., Young, Ed. D., de Vries, J., Nimmo, F., et al. (2015). Accretion and differentiation of the terrestrial planets with implications for the compositions of early-formed solar system bodies and accretion of water. *Icarus*, *248*, 89–108.
Rudge, J. F., Kleine, T., & Bourdon, B. (2010). Broad bounds on Earth's accretion and core formation constrained by geochemical models. *Nature Geoscience*, *3*, 439–443.
Samuel, H. (2012). A re-evaluation of metal diapir breakup and equilibration in terrestrial magma oceans. *Earth and Planetary Science Letters*, *313*, 105–114.
Samuel, H., & Tackley, P. J. (2008, June). Dynamics of core formation and equilibration by negative diapirism. *Geochemistry, Geophysics, Geosystems*, *9*, 6011–+. https://doi.org/10.1029/2007GC001896.
Samuel, H., Tackley, P. J., & Evonuk, M. (2010). Heat partitioning in terrestrial planets during core formation by negative diapirism. *Earth and Planetary Science Letters*, *290*, 13–19. https://doi.org/10.1016/j.epsl.2009.11.050.
Schaeffer, N., Jault, D., Nataf, H.-C., & Fournier, A. (2017). Turbulent geodynamo simulations: A leap towards Earth's core. *Geophysical Journal International*, *211*(1), 1–29.
Scorer, R. S. (1957). Experiments on convection of isolated masses of buoyant fluid. *Journal of Fluid Mechanics Digital Archive*, *2*(06), 583–594. https://doi.org/10.1017/S0022112057000397.
Seagle, C. T., Cottrell, E., Fei, Y., Hummer, D. R., & Prakapenka, V. B. (2013). Electrical and thermal transport properties of iron and iron-silicon alloy at high pressure. *Geophysical Research Letters*, *40*(20), 5377–5381.
Stacey, F. D., & Anderson, O. L. (2001). Electrical and thermal conductivities of Fe-Ni-Si alloy under core conditions. *Physics of the Earth and Planetary Interiors*, *124*, 153–162.
Stacey, F. D., & Loper, D. E. (2007). A revised estimate of the conductivity of iron alloy at high pressure and implications for the core energy balance. *Physics of the Earth and Planetary Interiors*, *161*, 13–18.
Starchenko, S. V., & Jones, C. A. (2002). Typical velocities and magnetic field strengths in planetary interiors. *Icarus*, *157*(2), 426–435.
Stelzer, Z., & Jackson, A. (2013). Extracting scaling laws from numerical dynamo models. *Geophysical Journal International*, *193*(3), 1265–1276.
Stevenson, D. J. (1990). Fluid dynamics of core formation. *Origin of the earth* (pp. 231–249). Oxford: Oxford University Press.

Stevenson, D. J. (2003). Planetary science: Mission to Earth's core—a modest proposal. *Nature*, *423*(6937), 239–240.

Stieglitz, R., & Müller, U. (2001). Experimental demonstration of a homogeneous two-scale dynamo. *Physics of Fluids*, *13*(3), 561–564.

Sumita, I., & Bergman, M. I. (2015). Inner-core dynamics. In Schubert G. (Ed.), *Treatise on geophysics* (Vol. 8, pp. 297–316). Elsevier.

Taylor, G. I. (1934). The formation of emulsions in definable fields of flow. *Proceedings of the Royal Society of London A*, *146*(858), 501–523.

Tomotika, S. (1936). Breaking up of a drop of viscous liquid immersed in another viscous fluid which is extending at a uniform rate. *Proceedings of the Royal Society of London A*, *153*(879), 302–318.

Ulvrová, M., Coltice, N., Ricard, Y., Labrosse, S., Dubuffet, F., Velímskỳ, J., et al. (2011). Compositional and thermal equilibration of particles, drops and diapirs in geophysical flows. *Geochemistry Geophysics Geosystems*, *12*(10), 1–11.

Verhoogen, J. (1961). Heat balance of the Earth's core. *Geophysical Journal of the Royal Astronomical Society*, *4*, 276–291.

Villermaux, E. (2007). Fragmentation. *Annual Review of Fluid Mechanics*, *39*, 419–446.

Wacheul, J.-B., & Le Bars, M. (2017). Experiments on fragmentation and thermo-chemical exchanges during planetary core formation. *Physics of the Earth and Planetary Interiors*.

Wacheul, J.-B., Le Bars, M., Monteux, J., & Aurnou, J. M. (2014). Laboratory experiments on the breakup of liquid metal diapirs. *Earth and Planetary Science Letters*, *403*, 236–245.

Walsh, K. J., Morbidelli, A., Raymond, S. N., O'Brien, D. P., & Mandell, A. M. (2011). A low mass for Mars from Jupiter/'s early gas-driven migration. *Nature*, *475*(7355), 206–209.

Weber, P., & Machetel, P. (1992). Convection within the inner-core and thermal implications. *Geophysical Research Letters*, *19*, 2107–2110.

Wenk, H.-R., Baumgardner, J. R., Lebensohn, R. A., & Tomé, C. N. (2000). A convection model to explain anisotropy of the inner core. *Journal of Geophysical Research*, *105*, 5663–5678.

Williams, J.-P., & Nimmo, F. (2004, February). Thermal evolution of the Martian core: Implications for an early dynamo. *Geology*, *32* 97–+.

Wood, B., Walter, M., & Wade, J. (2006). Accretion of the Earth and segregation of its core. *Nature*, *441*(7095), 825–833. ISSN 0028-0836. https://doi.org/10.1038/nature04763.

Woodward, B. (1959). The motion in and around isolated thermals. *Quarterly Journal of the Royal Meteorological Society*, *85*(364), 144–151.

Yin, Q., Jacobsen, S. B., Yamashita, K., Blichert-Toft, J., Telouk, P., & Albarede, F. (2002). A short timescale for terrestrial planet formation from Hf/W chronometry of meteorites. *Nature*, *418*(6901), 949–952. ISSN 0028-0836. https://doi.org/10.1038/nature00995.

Zhang, K., & Busse, F. H. (1988). Finite amplitude convection and magnetic field generation in a rotating spherical shell. *Geophysical & Astrophysical Fluid Dynamics*, *44*(1–4), 33–53.

Chapter 6
A Brief Introduction to Turbulence in Rotating and Stratified Fluids

Benjamin Favier

Abstract This chapter discusses basic aspects of turbulent flows relevant for the small-scale fluid dynamics of planets and stars. We particularly focus on how geometrical confinement, rotation, and stratification affect the nature of turbulent motions at different spatial scales. We introduce a hierarchy of models from the celebrated theory of Kolmogorov valid for homogeneous and isotropic turbulence to gradually more realistic models including rotation and stratification effects. Emphasis is put on simple physical processes and qualitative observations and not on rigorous mathematical derivations.

Introduction

Most of the fluid layers of planets and stars are in a turbulent state. This is a direct consequence of the very large spatial extent of these fluid domains so that molecular viscosity is virtually negligible at these scales. A cascade mechanism is therefore required to bring kinetic energy from the scales at which it is injected (usually by direct forcing or by some instability mechanism) to those where dissipative mechanisms are efficient. In the classical homogeneous isotropic case, this leads to the self-similar theory of turbulence postulated by Kolmogorov (1941). Fluid layers inside planets and stars are however constrained by at least four fundamental aspects, two of which will be discussed in this chapter: background rotation, stable density stratification, compressibility, and magnetic field.

This chapter will only consider non-electrically conducting fluids so that the subtle interaction between fluid motions and magnetic fields, a topic called magnetohydrodynamics (see the chapter by Deguen and Lasbleis of this book and Davidson (2013) for more details), will not be discussed. We will also focus on incompressible dynamics.

B. Favier (✉)
Aix Marseille University, CNRS, Centrale Marseille, IRPHE UMR, 7342 Marseille, France
e-mail: favier@irphe.univ-mrs.fr

M. Le Bars and D. Lecoanet (eds.), *Fluid Mechanics of Planets and Stars*,
CISM International Centre for Mechanical Sciences 595,
https://doi.org/10.1007/978-3-030-22074-7_6

Adding rotation and stratification to the turbulence problem is two edged: on the one hand, linear waves are now supported which reintroduces linear dynamics to the fundamentally nonlinear problem of turbulence. On the other hand, additional dimensionless parameters mean that different dynamical regimes are expected depending on the relative importance between the turbulence and the linear effects.

This chapter is by no mean a complete overview of the vast literature about turbulence in rotating and stratified fluids. The goal is primary to link fundamental models of turbulence such as homogeneous and isotropic turbulence to slightly more realistic models aiming at modeling small-scale flows in geophysical and astrophysical systems. The applications of these general concepts to more specific and complex flows inside planets and stars can be found in the other chapters and in specialized books and articles (e.g., Pedlosky (1992); Vallis (2006); Clarke et al. (2007); Davidson (2013); Alexakis and Biferale (2018)).

3D Homogeneous Isotropic Turbulence

This is the canonical model and probably the most natural starting point when considering turbulence. Most of our current understanding of turbulence was developed using the following assumptions: homogeneity and isotropy (and to a lesser extent, stationarity) (Batchelor 1953). While these assumptions are highly unrealistic at first glance, they allow for a systematic mathematical description of the statistics of a turbulent flow. Additionally, even if the large scales of realistic turbulent flows are neither homogeneous nor isotropic, these idealized properties might be recovered at the smallest spatial scales of the flow, far from any anisotropic and inhomogeneous energy injection mechanism.

Let us consider a velocity field $\boldsymbol{u}$ function of the position $\boldsymbol{x}$ and time t. A standard quantity to statistically describe this flow field is the velocity correlation tensor defined by

$$R_{ij}(\boldsymbol{x}, \boldsymbol{r}, t) = \left\langle u_i(\boldsymbol{x}, t) u_j(\boldsymbol{x} + \boldsymbol{r}, t) \right\rangle, \tag{6.1}$$

where brackets indicate an ensemble average. Assuming the flow to be homogeneous implies that the statistics of the flow do not depend on position $\boldsymbol{x}$ but only on the separation vector $\boldsymbol{r}$:

$$R_{ij}(\boldsymbol{x}, \boldsymbol{r}, t) = R_{ij}(\boldsymbol{r}, t). \tag{6.2}$$

In other words, there are no spatial gradients in any statistical quantity describing the flow. This discards physical boundaries or interfaces since the statistics of the flow would then depend on the distance to that boundary or interface, making the system effectively inhomogeneous. Assuming the flow to be additionally isotropic implies that only the norm of the separation vector matters

$$R_{ij}(\boldsymbol{r}, t) = R_{ij}(r, t) \quad \text{with} \quad r = |\boldsymbol{r}|. \tag{6.3}$$

There are no preferential direction required to statistically describe the flow, which is not true as soon as rotation or stratification is introduced. Finally, it is often assumed that the flow is stationary so that

$$R_{ij}(r,t) = R_{ij}(r)\ . \tag{6.4}$$

All these assumptions greatly simplify the statistical description of a turbulent flow, as will become apparent in the next sections. However, one should never forget that these assumptions are almost never satisfied in realistic flows and should systematically be questioned.

Let us now define the governing equations. The velocity field satisfies the Navier–Stokes equations for an incompressible fluid

$$\frac{\partial \boldsymbol{u}}{\partial t} + \boldsymbol{u}\cdot\nabla\boldsymbol{u} = -\nabla P + \nu\nabla^2\boldsymbol{u} + \boldsymbol{F} \tag{6.5}$$

$$\nabla\cdot\boldsymbol{u} = 0\ , \tag{6.6}$$

where P is the pressure divided by the constant fluid density, ν is the constant kinematic viscosity, and $\boldsymbol{F}$ is some external forcing. The only dimensionless number characteristic of these equations is the Reynolds number Re, measuring the relative importance of the nonlinear inertial term to viscous forces

$$\frac{|\boldsymbol{u}\cdot\nabla\boldsymbol{u}|}{|\nu\nabla^2\boldsymbol{u}|} \approx \frac{UL}{\nu} \equiv Re, \tag{6.7}$$

where we have introduced U a typical velocity and L a typical length. In many contexts, and this is the case for most of the fluid layers of planets and stars, $Re \gg 1$ and the flow is inevitably turbulent. At a spatial scale L characteristic of the flow, viscous forces are negligible compared to the inertia of the fluid.

The scalar product between Eq. (6.5) and $\boldsymbol{u}$, integrated over a given volume V (assuming homogeneity or appropriate boundary conditions), leads to the following kinetic energy equation:

$$\frac{dK}{dt} = \frac{d}{dt}\int_V \frac{1}{2}\boldsymbol{u}^2 \mathrm{d}V = -\int_V \underbrace{2\nu S_{ij}S_{ij}}_{\epsilon}\,\mathrm{d}V + \int_V \boldsymbol{u}\cdot\boldsymbol{F}\mathrm{d}V, \tag{6.8}$$

where S_{ij} is the rate of strain tensor and we have introduced ϵ the rate of dissipation of turbulent kinetic energy. As a consequence, steady states are obtained when the work done by the forcing is balanced by viscous dissipation. Neglecting viscosity altogether, which might look like a good idea for high Reynolds number flows, leads to an unbounded growth of the kinetic energy.

The Zeroth Law of Turbulence

This is the single most important empirical observation about turbulence. The zeroth law of turbulence is the following:

> The rate of dissipation of turbulent kinetic energy is finite
> and independent of viscosity for $Re \to \infty$.

No matter how small the viscosity is, providing that it is not zero, ϵ will remain finite. There are several empirical observations which are directly related to the zeroth law of turbulence. The drag coefficient of an object moving in a viscous fluid is eventually independent of the Reynolds number when the latter is large enough. The energy loss in a pipe flow with a sudden change in the section is independent of viscosity at large Reynolds numbers (the so-called Borda–Carnot energy loss equation).

At first look, the fact that the flow can dissipate energy even when the viscosity goes to zero can be surprising. The rate of dissipation of kinetic energy is $\epsilon = 2\nu S_{ij} S_{ij}$, where $S_{ij} = 1/2(\partial u_i/\partial x_j + \partial u_j/\partial x_i)$. In order for ϵ to remain constant as $\nu \to 0$, the velocity gradients must diverge $\partial u_i/\partial x_j \to \infty$. We therefore expect very large velocity gradients in the flow in order to dissipate energy. Assuming that ϵ depends on u and l only (and not on viscosity), where u is a typical velocity and l a typical length scale, we obtain the classical dimensional scaling

$$\epsilon \sim u^3/l \ . \tag{6.9}$$

Richardson's Cascade and Kolmogorov's 2/3rd Law

The cascade mechanism, which brings energy from large to small scales, was postulated by Richardson (1922) and summarized in the famous poem

> Big whirls have little whirls that feed on their velocity,
> And little whirls have lesser whirls and so on to viscosity.

The main hypothesis is that the energy flux from large to small scales takes the form of a long chain of inertial transfers. This is observed in many turbulent flows where large-scale circulations collapse into small-scale disorder (see a numerical example in Fig. 6.1). The flux of energy Π across any spatial scale r must be equal to ϵ (far from forcing and dissipation) and is equal to the kinetic energy u_r^2 at scale r divided by the turnover time r/u_r at the same scale:

$$\Pi(r) = \frac{u_r^2}{r/u_r} = \frac{u_r^3}{r} = \epsilon \quad \Rightarrow \quad u_r^2 \sim (\epsilon r)^{2/3} \ . \tag{6.10}$$

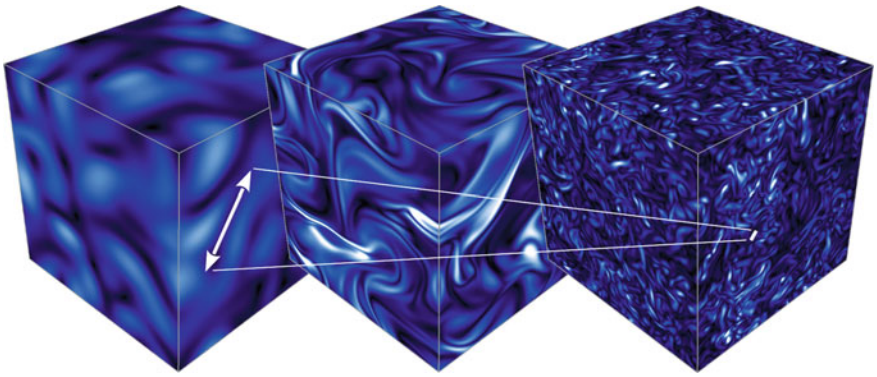

Fig. 6.1 Time evolution of the enstrophy in a standard tri-periodic direct numerical simulation of the decaying (i.e. without external forcing) Navier–Stokes equations. The initial condition contains only large-scale structures which collapse into small-scale vorticity filaments as time increases. Dark colors correspond to low enstrophy values while bright colors correspond to large enstrophy values

This is the so-called Kolmogorov's 2/3rd law, which is usually written for the longitudinal velocity structure function as

$$\left\langle (\delta u_r)^2 \right\rangle = C_K \, (\epsilon r)^{2/3} \tag{6.11}$$

where $\delta u_r(\boldsymbol{r}) = u(\boldsymbol{x} + \boldsymbol{r}) - u(\boldsymbol{x})$ and C_K is a universal constant.

Let us assume that the large scales have a velocity u and a length scale l, while the dissipative scales have a velocity u_η and a length scale η. Viscous dissipation balances inertia only at the dissipation scale so that the Reynolds number at that scale is of order unity:

$$\frac{u_\eta \eta}{\nu} \sim 1 \, . \tag{6.12}$$

The dissipation rate is $\epsilon \equiv 2\nu S_{ij} S_{ij} \sim \nu (u_\eta/\eta)^2$ leading to

$$\eta \sim \left(\frac{\nu^3}{\epsilon} \right)^{1/4} \quad \text{and} \quad u_\eta \sim (\nu \epsilon)^{1/4} \tag{6.13}$$

where η is often called the Kolmogorov scale. This is the scale at which energy is dissipated and beyond which the flow becomes smooth due to dominant viscous effects. Using $\epsilon \sim u^3/l$, one can make the link between large and small scales as a function of the Reynolds number:

$$\frac{\eta}{l} \sim \left(\frac{ul}{\nu} \right)^{-3/4} = Re^{-3/4} \quad \text{and} \quad \frac{u_\eta}{u} \sim \left(\frac{ul}{\nu} \right)^{-1/4} = Re^{-1/4} \, . \tag{6.14}$$

Spectral Statistics

Turbulence dynamics is often described in Fourier space, which is a natural way of studying the energy transfers across different scales in a homogeneous context. The forward and backward Fourier transforms are

$$\hat{\boldsymbol{u}}(\boldsymbol{k}) = \frac{1}{(2\pi)^3}\int \boldsymbol{u}(\boldsymbol{x})e^{-i\boldsymbol{k}\cdot\boldsymbol{x}}\mathrm{d}\boldsymbol{x} \quad \text{and} \quad \boldsymbol{u}(\boldsymbol{x}) = \int \hat{\boldsymbol{u}}(\boldsymbol{k})e^{i\boldsymbol{k}\cdot\boldsymbol{x}}\mathrm{d}\boldsymbol{k}\ . \tag{6.15}$$

The velocity correlation tensor can be defined in both spaces as

$$\hat{R}_{ij}(\boldsymbol{k}) = \frac{1}{(2\pi)^3}\int R_{ij}(\boldsymbol{r})e^{-i\boldsymbol{k}\cdot\boldsymbol{x}}\mathrm{d}\boldsymbol{x} \quad \text{and} \quad R_{ij}(\boldsymbol{r}) = \left\langle u_i(\boldsymbol{x}+\boldsymbol{r})u_j(\boldsymbol{x})\right\rangle\ . \tag{6.16}$$

Starting from the total kinetic energy of the system, one can then define the standard isotropic energy spectrum $E(k)$ as

$$K = \frac{1}{2}\int \hat{R}_{ii}(\boldsymbol{k})\mathrm{d}\boldsymbol{k} = \int e(\boldsymbol{k})\mathrm{d}\boldsymbol{k} = \int_0^\infty \underbrace{\left[\int_0^\pi\int_0^{2\pi} e(\boldsymbol{k})k^2\sin\theta\mathrm{d}\theta\mathrm{d}\phi\right]}_{E(k)}\mathrm{d}k, \tag{6.17}$$

where the wave vector $\boldsymbol{k}$ has been written in spherical coordinates $(k.\theta, \phi)$. For isotropic velocity fields,

$$E(k) = 2\pi k^2\hat{R}_{ii}(k)\ . \tag{6.18}$$

Note that while this definition is valid for any homogeneous turbulent flow, it is important to remember that an angular average has been performed, so that anistropic flows, such as rotating or stratified flows, are not well described by the inherently isotropic quantity $E(k)$.

Assuming that $E(k)$ depends on ϵ and k only (and not on viscosity) leads to the celebrated Kolmogorov energy spectrum

$$E(k) \sim \epsilon^{2/3}k^{-5/3}\ . \tag{6.19}$$

While this slope is indeed observed in many experiments and simulations (Frisch 1995), it is important to remember that this quantity only carries a fraction of the information contained in the full velocity field. In particular, the phase information, fundamental to reconstruct the velocity field in physical space, is lost. As an example, we show in Fig. 6.2 two velocity fields with the same Kolmogorov-like energy spectrum. One is a solution of the Navier–Stokes equations while the second is not.

The evolution equation for the energy spectrum is given by the so-called Lin equation

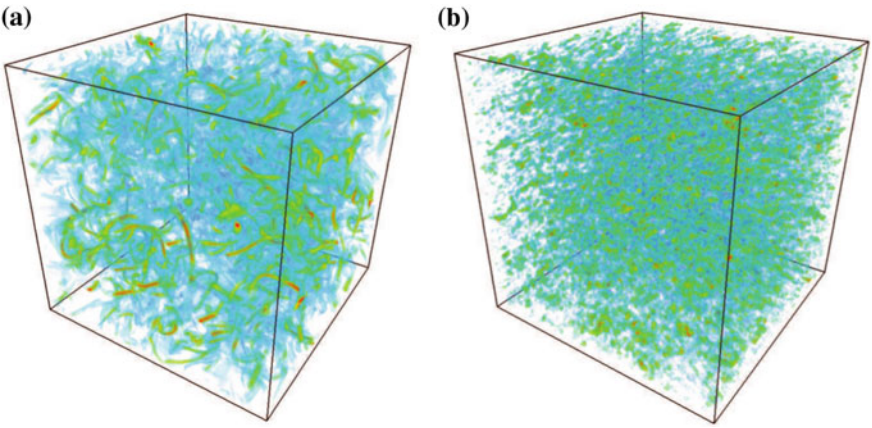

Fig. 6.2 **a** Volume rendering of the enstrophy in a standard tri-periodic direct numerical simulation of the forced Navier–Stokes equations. **b** Same as (**a**) but the flow field is not a solution of the Navier–Stokes equations. It is incompressible and has the same power spectrum $E(k)$ as the flow showed in (**a**), but the phase information has been randomized. Figures taken from Favier (2009)

$$\left(\frac{\partial}{\partial t} + \underbrace{2\nu k^2}_{\text{Dissipation}}\right) E(k,t) = \underbrace{T(k,t)}_{\text{Transfer}} + \underbrace{P(k,t)}_{\text{Production}}, \tag{6.20}$$

where $T(k)$ is the energy flux through wave number k which can be expressed in terms of third-order velocity moments (Frisch 1995; Davidson 2013). By definition, the transfer term does not contribute to the overall energy budget, so that

$$\int_0^\infty T(k)\mathrm{d}k = 0\,. \tag{6.21}$$

In a stationary state, we have the balance

$$\int_0^\infty 2\nu k^2 E(k)\mathrm{d}k = \int_0^\infty P(k)\mathrm{d}k = \epsilon \tag{6.22}$$

which is the same as Eq. (6.8).

Even if Kolmogorov theory is widely used in many contexts, one should remember that it holds when the following assumptions are satisfied:

- Homogeneity (which excludes physical boundaries, local bursts of turbulence, mixing layers, interfaces, etc.).
- Isotropy (which excludes rotating and stratified flows).
- Locality (which excludes nonlocal energy transfers across separated length scales).
- $Re \to \infty$ (which is fortunately verified by geophysical flows).

2D Homogeneous Isotropic Turbulence

The second canonical model to study turbulence, and which can also be seen as a first step toward geophysical and astrophysical turbulent flows, is two-dimensional (2D) turbulence. There are many situations where a 3D velocity field becomes effectively quasi-2D, for example:

- Rotation: rapid rotation dynamically leads to flows invariant along the rotation axis (see Taylor–Proudman theorem and section 3D Homogeneous Turbulence in Rotating Fluids).
- Magnetic field: an intense externally imposed magnetic field can lead to an anisotropic dissipation and partial bi-dimensionalization (Alexakis 2011; Favier et al. 2011).
- Geometric confinement: a fluid confined to a layer of depth h can be considered 2D over horizontal length scales $L \gg h$ (Smith et al. 1996).

Governing Equations

Let us assume that the velocity field is purely 2D in the (x, y)-plane

$$\boldsymbol{u}(x, y, t) = \big(u(x, y, t), v(x, y, t), 0\big) , \tag{6.23}$$

the vorticity is then

$$\boldsymbol{\omega} = \nabla \times \boldsymbol{u} = (0, 0, \zeta) \quad \text{with} \quad \zeta = \frac{\partial v}{\partial x} - \frac{\partial u}{\partial y} . \tag{6.24}$$

Note that the vortex stretching term $\boldsymbol{\omega} \cdot \nabla \boldsymbol{u}$ in the vorticity equation, so important in 3D and at the origin of the generation of small-scale intense velocity gradients, is identically zero. This means that the vorticity is conserved along fluid trajectories (without viscosity of course), which will have dramatic consequences on the energy fluxes.

The general equation for the vorticity is

$$\frac{\partial \zeta}{\partial t} + \boldsymbol{u} \cdot \nabla \zeta = \nu \nabla^2 \zeta . \tag{6.25}$$

Introducing the stream function ψ such that

$$\boldsymbol{u} = -\nabla \times (\psi \boldsymbol{e}_z) = -\nabla \psi \times \boldsymbol{e}_z , \tag{6.26}$$

we have

$$\frac{\partial \zeta}{\partial t} + J(\psi, \zeta) = \nu \nabla^2 \zeta, \tag{6.27}$$

where

$$J(\psi,\zeta)=\frac{\partial\psi}{\partial x}\frac{\partial\zeta}{\partial y}-\frac{\partial\zeta}{\partial x}\frac{\partial\psi}{\partial y}\quad\text{and}\quad\zeta=\nabla^2\psi\,. \tag{6.28}$$

The total kinetic energy over a domain S is

$$K=\frac{1}{2}\int_S \boldsymbol{u}^2\mathrm{d}S=\frac{1}{2}\int_S(\nabla\psi)^2\,\mathrm{d}S=-\frac{1}{2}\int_S\psi\zeta\mathrm{d}S \tag{6.29}$$

and one can define a new quantity called enstrophy defined as

$$Z=\frac{1}{2}\int_S\zeta^2\mathrm{d}S=\frac{1}{2}\int_S\left(\nabla^2\psi\right)^2\mathrm{d}S\,. \tag{6.30}$$

In the absence of forcing, these two quantities evolve according to the following conservation equations:

$$\frac{dK}{dt}=-2\nu Z=-\epsilon\quad\text{and}\quad\frac{dZ}{dt}=-\nu\int_S|\nabla\zeta|^2\mathrm{d}S\,. \tag{6.31}$$

Both kinetic energy and enstrophy are therefore inviscid invariants of the 2D Navier–Stokes equations. A key observation is that the enstrophy Z is bounded by its initial value. Since $\epsilon=2\nu Z$ and Z is bounded, it is not possible for ϵ to remain constant in the limit of vanishing viscosity. The zeroth law of turbulence is not applicable, there is no dissipation anomaly in 2D turbulence! It is therefore expected that $\epsilon\to 0$ when $\nu\to 0$.

Forward Cascade of Enstrophy

The vorticity of fluid parcels is conserved in the absence of viscosity. As a uniform vorticity blob is being stretched by the underlying turbulent flow, its transverse scale is decreasing, thus increasing vorticity gradients. This leads to the conclusion that the enstrophy is cascading toward small scales at a constant flux η. The typical turnover time at a wave number k with energy $E(k)$ is

$$\tau(k)\sim\left(k^3E(k)\right)^{-1/2}, \tag{6.32}$$

so that the dissipation rate of enstrophy $Z=\int k^2E(k)\mathrm{d}k$ per unit mass is given by

$$\eta\sim\frac{k^3E(k)}{\tau(k)}\sim\left(k^3E(k)\right)^{3/2}\quad\Rightarrow\quad E(k)\sim\eta^{2/3}k^{-3}\,. \tag{6.33}$$

This prediction is valid only for scales smaller than the energy injection scale and corresponds to a direct cascade of enstrophy.

Inverse Cascade of Energy

If the enstrophy is cascading toward small scales, what is a fate of the kinetic energy, which is another invariant of the inviscid equations? Let us define the energy spectrum centroid

$$k_c = \frac{\int k E(k) \mathrm{d}k}{\int E(k) \mathrm{d}k} \tag{6.34}$$

and the weighted spectrum

$$I = \int (k - k_c)^2 \, E(k) \mathrm{d}k = \underbrace{\int k^2 E(k) \mathrm{d}k}_{Z} - k_c^2 \underbrace{\int E(k) \mathrm{d}k}_{K} . \tag{6.35}$$

Assuming that $\frac{dI}{dt} > 0$ (i.e., the energy spreads in spectral space which is a natural assumption for this nonlinear system) and using enstrophy conservation leads to

$$\frac{dk_c^2}{dt} < 0 . \tag{6.36}$$

The energy spectrum centroid is decreasing with time, energy is on average transferred toward large scales, this is the so-called inverse cascade regime first postulated by Kraichnan (1967). Using the same dimensional analysis as in 3D, the inverse cascade satisfies

$$E(k) \sim \epsilon^{2/3} k^{-5/3}, \tag{6.37}$$

where ϵ is now the energy flux carried by the inverse cascade. This prediction is only valid for scales larger than the energy injection scale.

Experimental and Numerical Evidences

The theoretical concept of inverse cascade predicted by Kraichnan (1967) has been verified both experimentally and numerically. Some experiments used a thin layer of light conducting fluid on top of a heavier fluid forced electromagnetically at small scales. They observed an accumulation of energy at the scale of the container (Paret and Tabeling 1997; Chen et al. 2006). Similar conclusions were achieved using soap films (Couder et al. 1989; Gharib and Derango 1989). 2D turbulence is ideally studied numerically (see Fig. 6.3 and Smith and Yakhot (1993) for example), and the double cascade scenario where energy is flowing toward large scales while enstrophy cascades toward small scales were recently achieved in one unique simulation with very large-scale separation (Boffetta and Musacchio 2010).

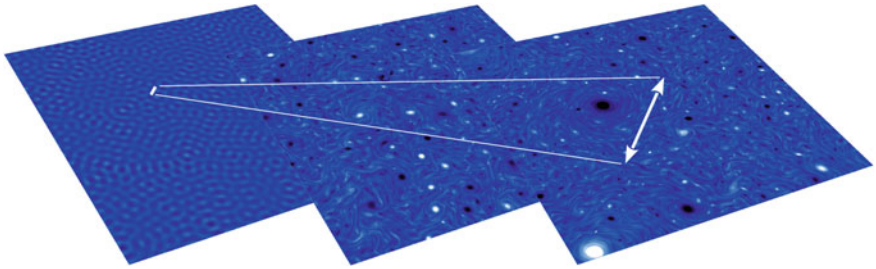

Fig. 6.3 Time evolution of the vertical vorticity in a standard doubly periodic direct numerical simulation of the forced 2D Navier–Stokes equations. The forcing is imposed at small scales only but large-scale coherent structures dynamically emerge. Bright and dark colors correspond to negative and positive values of the vorticity, respectively

Fate of the Energy at Large Scales

In the direct cascade regime, energy is transferred toward small scales, far from the nonuniversal behavior associated with the energy input at large scales. This gives some hope for the forward cascade mechanism characteristic of 3D turbulence to be universal. In the inverse cascade regime, however, energy piles up at the largest available scale so that the equilibrium state is not expected to be universal, but will depend on the details of the model considered. In the following, we give some examples of mechanisms responsible for the saturation of the inverse cascade.

In a doubly periodic domain, energy piles up at the box size generating a so-called condensate (Chertkov et al. 2007): a large-scale dipolar structure that interacts nonlocally with the cascade and modifies the $k^{-5/3}$ spectrum (Xia et al. 2008; Laurie et al. 2014).

In a closed container, no-slip boundary conditions can continuously reinject enstrophy in the system preventing the formation of large scales (Clercx et al. 2001).

If there is a linear friction term $-\lambda\zeta$ in the vorticity equation (to model the possible viscous coupling with a bottom boundary for example), an infrared cutoff is introduced at the transitional wave number $k_0 \sim \epsilon^{-1/2}\lambda^{3/2}$, where friction balances the upscale energy flux.

With additional physics (β-plane, finite-Rossby radius, etc.), the inverse cascade can compete with other mechanisms (see section Geostrophic Turbulence).

Thin-Layer Turbulence

While 2D turbulence is a necessary step to better understand energy transfers in more realistic flows, it is highly idealized and never exactly realized in nature. There have been several studies attempting to bridge the gap between 3D and 2D turbulence dynamics by considering the case of thin-layer turbulence (Smith et al. 1996; Celani et al. 2010).

Consider a thin layer of fluid contained between two stress-free horizontal plates a distance h apart. 3D turbulence is expected when the energy injection scale L_I is much smaller than the depth of the layer, $L_I \ll h$, while 2D turbulence is expected for $L_I \gg h$. In the intermediary regime, both inverse and direct energy cascades can exist, connected by a direct enstrophy cascade. Vortex stretching is negligible at large scales but feeds the direct energy cascade at small scales. This interesting split cascade scenario has been studied experimentally (Xia et al. 2009, 2011) and numerically (Benavides and Alexakis 2017).

There are other examples of inverse cascade of energy in three-dimensional systems. Rapidly rotating Rayleigh–Bénard convection is one of them: although the instability is intrinsically 3D, a spontaneous inverse cascade can develop in the so-called geostrophic turbulence regime (Julien et al. 2012; Favier et al. 2014, 2019).

Geostrophic Turbulence

The concept of homogeneous isotropic turbulence, both 2D and 3D, is very appealing from a theoretical point of view, but lacks several physical phenomena ubiquitous in geophysical and astrophysical applications. Fortunately, control parameters are often extreme in applications, leading to the derivation of reduced 2D or quasi-2D models. The purpose of this section is to give a brief overview of some of these models, and a more detailed description of the so-called β-plane turbulence.

Fundamental Concepts

There are several fundamental concepts very useful to study large-scale geophysical and astrophysical flows. Note that these are particularly useful to describe mid to high latitudes atmospheric or oceanic rotating flows in thin layers and are not necessarily relevant to other geophysical or astrophysical flows.

β-plane approximation: the lowest order effect of a planet sphericity appears only through the projection of the rotation vector on the local vertical axis

$$f = 2\boldsymbol{\Omega} \cdot \boldsymbol{e}_z \approx \underbrace{2\Omega \sin\theta_0}_{f_0} + \underbrace{\frac{2\Omega \cos\theta_0}{R_e}}_{\beta} y, \tag{6.38}$$

where Ω is the rotation rate, $\boldsymbol{e}_z$ is the local vertical axis, θ_0 is the latitude, R_e is the radius of the planet, and y is the local meridional coordinate (see Fig. 6.4). This effectively corresponds to a local linear variation of the Coriolis force along the meridional direction. The Coriolis parameter f is maximum at the pole while the β effect is negligible there.

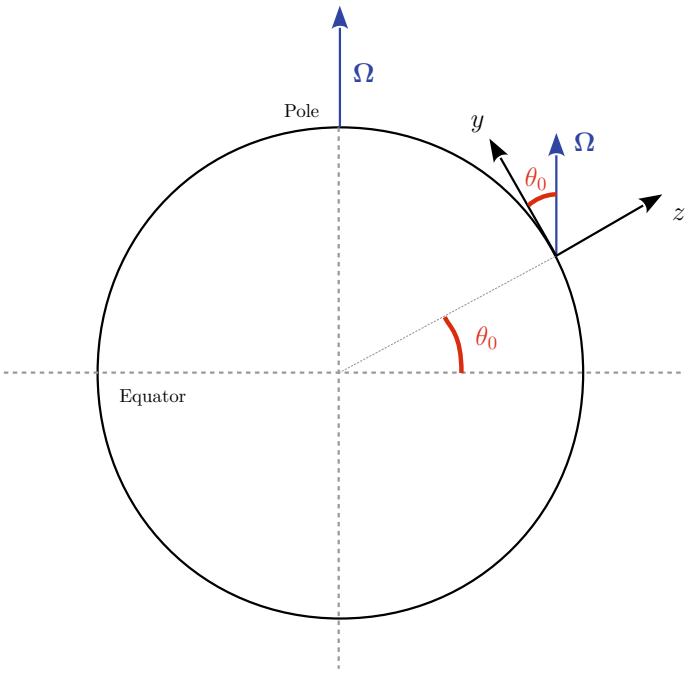

Fig. 6.4 Local β plane approximation. Only the local vertical projection of the rotation vector $\boldsymbol{\Omega}$ matters. θ_0 is the latitude

Hydrostatic balance: the vertical momentum balance reduces to

$$\partial_z P = -\rho g \,, \tag{6.39}$$

and inertial terms can be neglected. P is the pressure, ρ the density, and g is the gravitational acceleration.

Geostrophic balance: the horizontal momentum balance reduces to

$$f \boldsymbol{e}_z \times \boldsymbol{u} = -\frac{1}{\rho} \nabla_h P \,, \tag{6.40}$$

where ∇_h is the horizontal gradient operator.

Rossby radius of deformation: this is the fundamental scale at which rotation effects become as important as gravitational effects:

$$L_D = \frac{\sqrt{gh}}{f}, \tag{6.41}$$

where h is the fluid depth.

Quasi-geostrophy (QG)

In essence, quasi-geostrophic models consider perturbations from an exact geostrophic balance. Equations are obtained by a formal expansion in Rossby number $Ro = U/(fL)$, where U is a typical velocity and L its horizontal length scale:

$$\boldsymbol{u} = \boldsymbol{u}_0 + Ro\boldsymbol{u}_1 + \cdots \tag{6.42}$$

The first order gives the diagnostic geostrophic balance (6.40) while the next order gives the prognostic vorticity equation. In addition to the Rossby number being small, there are additional assumptions: the Ekman number $E = \frac{\nu}{fH^2}$, where H is a vertical length scale, must be small and $T \gg f^{-1}$, where T is a typical timescale (Pedlosky 1992; Vallis 2006).

There exists a hierarchy of QG models with an increasing degree of complexity. All of the models are derived from the vertical vorticity equation and can generally be written in the following form:

$$\frac{Dq}{Dt} = \text{Forcing} - \text{Dissipation} + O(Ro), \tag{6.43}$$

where we have introduced the potential vorticity q and D/Dt is the material derivative. In the absence of forcing or dissipative effects, q is a conserved quantity. Here is a list of some classical models, whose complete derivations can be found in classical textbooks (Pedlosky 1992; Vallis 2006):

- 2D Euler $q = \nabla^2\psi,$
- β-plane (rigid lid approximation) $q = \nabla^2\psi + \beta y,$
- Shallow water QG (Charney–Hasegawa–Mima) $q = \nabla^2\psi - \frac{1}{L_D^2}\psi + \beta y,$
- Full shallow water QG $q = \frac{\nabla^2\psi + f}{h},$ and
- Boussinesq continuous QG $q = \nabla^2\psi + \frac{\partial}{\partial z}\left(\frac{f^2}{N^2}\frac{\partial\psi}{\partial z}\right).$

2D Turbulence on a β Plane

We focus in the rest of this section on the simplest QG model, the β-plane, and consider the dynamics of a 2D turbulent flow on such a plane.

Consider first a 2D horizontal flow rotating around the vertical. The vorticity equation is

$$\frac{\partial\zeta}{\partial t} + \boldsymbol{u}\cdot\nabla(\zeta + f) = \frac{D(\zeta + f)}{Dt} = \nu\nabla^2\zeta\,. \tag{6.44}$$

If $f = \text{cste}$, rotation does not affect the 2D flow. On the β-plane, however, $f = f_0 + \beta y$ as we saw previously in Eq. (6.38), and the vorticity equation is

$$\frac{\partial \zeta}{\partial t} + \boldsymbol{u} \cdot \nabla \zeta + \beta u_y = \frac{D\left(\zeta + \beta y\right)}{Dt} = \nu \nabla^2 \zeta \,, \tag{6.45}$$

where we see that the potential vorticity $q = \zeta + \beta y$ is materially conserved in the absence of viscosity. By analogy to 2D flows, the two inviscid invariants are also

$$K = -\frac{1}{2}\int_S \psi \zeta \mathrm{d}S \quad \text{and} \quad Z = \frac{1}{2}\int_S \zeta^2 \mathrm{d}S \,. \tag{6.46}$$

So far, the properties of β-plane turbulence seem very similar to standard 2D turbulence. A key difference is the existence of linear waves which were nonexistent in 2D isotropic turbulence. The vorticity equation in its linearized and inviscid form is indeed simply

$$\frac{\partial \zeta}{\partial t} = -\beta u_y \,, \tag{6.47}$$

where u_y is the velocity component in the meridional direction. Looking for plane wave solution of the form $\psi \sim \exp\left[i\left(\boldsymbol{k} \cdot \boldsymbol{x} - \omega t\right)\right]$ leads to the dispersion relation

$$\omega = -\beta \frac{k_x}{k^2} \,. \tag{6.48}$$

These Rossby waves propagate westward with a zonal phase velocity

$$c_{p,x} = \frac{\omega}{k_x} = -\frac{\beta}{k^2} \,. \tag{6.49}$$

The question is now to understand the importance of these Rossby waves in the dynamics of fully developed β-plane turbulence. We compare two simulations of β-plane turbulence in a channel in Fig. 6.5, one with $\beta = 0$ (standard 2D turbulence) and one with $\beta \neq 0$. Both are forced at small spatial scales. While we observe large-scale flows in both cases, vortices are favored in the standard 2D case while jets are sustained in the direction perpendicular to the background potential vorticity gradient for the β-plane turbulence. These large-scale jets are reminiscent of zonal jets observed on the atmosphere of Jupiter.

A balance between inertial and β terms in Eq. (6.45) gives

$$\frac{|\boldsymbol{u} \cdot \nabla \zeta|}{|\beta u_y|} \sim \frac{\zeta}{\beta L} \sim \frac{U}{\beta L^2} \sim 1 \quad \Rightarrow \quad L_{Rh} \sim \sqrt{U/\beta}, \tag{6.50}$$

where we introduced the length scale L_{Rh} called the Rhines scale (Rhines 1975). For scales much smaller than L_{Rh}, inertia dominates and the inverse cascade mechanism characteristic of classical 2D turbulence persists. At these small spatial scales, the frequency of Rossby waves is much lower than the typical turnover time of turbulent eddies and no significant interaction is expected. For scales comparable with L_{Rh}, however, β-plane dynamics and associated Rossby waves come into play. Note that

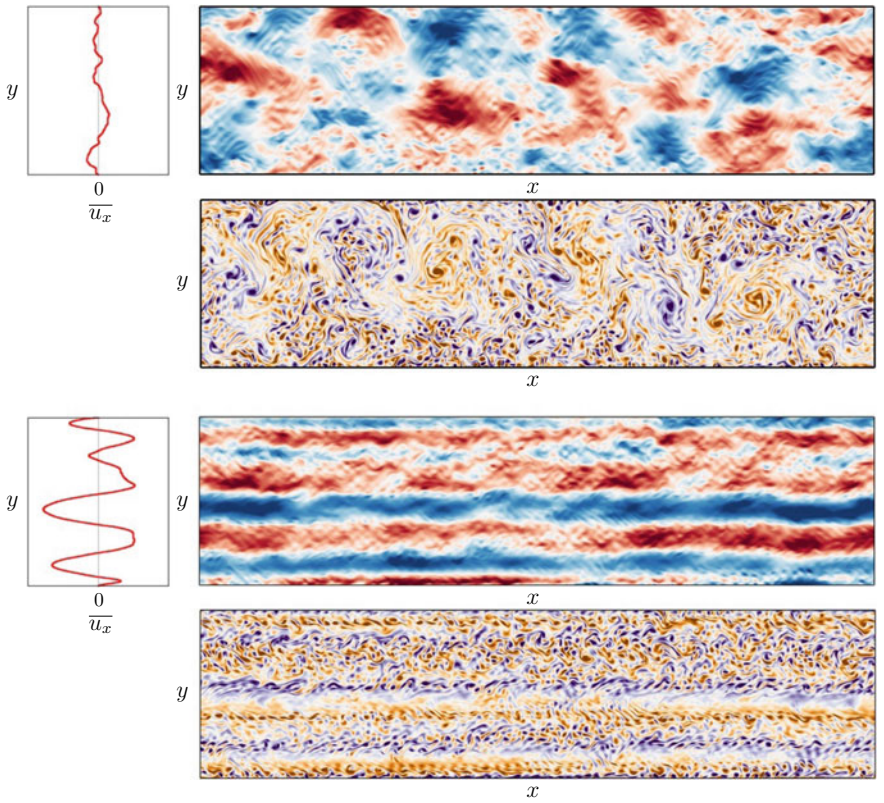

Fig. 6.5 2D turbulence forced at small scales in a periodic channel (boundaries are periodic in the horizontal direction and no-slip at the top and bottom of the channel). There is no β-effect at the top while there is one at the bottom (the gradient of potential vorticity is vertical). We show the horizontal velocity on the upper panel, the vorticity on the lower panel and the horizontally averaged flow $\overline{u_x} = 1/L_x \int u_x \mathrm{d}x$ on the left plot

we assumed that velocity and vorticity are evolving on the same length scale (see Eq. (6.50)), which is an arbitrary choice. One could equally choose another measure for the vorticity, such as $Z = \left\langle \zeta^2 \right\rangle^{1/2}$, where $<>$ denotes some averaging process, leading to another transition length scale

$$L_Z = \frac{Z}{\beta} \,. \tag{6.51}$$

Discussions about the relevant length scales for Rossby waves excitation and jet formation can be found in Sukoriansky et al. (2007) and references therein.

The formation of zonal jets in β-plane turbulence can be explained as follows. Turbulence is expected to excite Rossby waves when the wave period and eddy turnover

time are matched, leading to a transition between an isotropic inverse cascade (generating isotropic large-scale vortices) to an anisotropic inverse cascade favoring zonal jets. This explanation was, for example, put forward by Vallis and Maltrud (1993). Equating the (anisotropic) frequency of a Rossby wave to the (isotropic) frequency of a turbulent eddy at wave number k leads to

$$\beta \frac{k_x}{k^2} \sim \epsilon^{1/3} k^{2/3} \quad \Rightarrow \quad k_x = k_\beta \cos^{8/5}\theta \quad \text{and} \quad k_y = k_\beta \sin\theta \cos^{3/5}\theta \,, \tag{6.52}$$

where we have introduced the polar angle $\theta = \tan^{-1}(k_y/k_x)$ and the transitional wave number

$$k_\beta = \left(\frac{\beta^3}{\epsilon}\right)^{1/5} . \tag{6.53}$$

Note that the Rhines scale is recovered by neglecting anisotropy and by replacing the turbulence eddy frequency $\omega \sim \epsilon^{1/3} k^{2/3}$ by the so-called sweeping frequency $\omega \sim kU$ where U is the same undetermined velocity scale as in Eq. (6.50). At scales smaller than k_β^{-1}, the usual 2D double cascade mechanism is expected to hold from the energy injection scale, with a direct cascade of enstrophy with rate η and an inverse energy cascade with rate ϵ:

$$E(k) \sim \eta^{2/3} k^{-3} \quad \text{and} \quad E(k) \sim \epsilon^{2/3} k^{-5/3} \,. \tag{6.54}$$

At scales comparable with k_β^{-1}, an anisotropic competition between Rossby waves and turbulent eddies appear as predicted by Eq. (6.52). The initially isotropic energy flux from the inverse cascade is channeled toward the plane $k_x \approx 0$ (structures invariant along the zonal axis, i.e., jets). Rhines (1975) postulated a critical balance between waves and turbulent eddies to predict the zonal flow spectrum (see also Huang et al. (2001))

$$|\boldsymbol{u} \cdot \nabla \zeta| \sim |\beta u_y| \quad \Rightarrow \quad \hat{u}(k) \sim \beta/k^2 \quad \Rightarrow \quad E_Z(k) \sim \beta^2 k^{-5}, \tag{6.55}$$

where $E_Z(k)$ is the energy spectrum of the zonally averaged flow. This scaling was observed in Jupiter atmosphere (Galperin et al. 2014) and in experiments (Cabanes et al. 2017). For more details about jets formation and dynamics, the interested reader is referred to the recent book by Galperin and Read (2019).

3D Homogeneous Turbulence in Rotating Fluids

The two previous sections discussed some properties of two-dimensional turbulence, with or without β effect. While these models are probably relevant for the largest scales of planetary flows, for which the Rossby number is very small, going down in scales gradually increases the local value of the Rossby number so that three-

dimensional effects come back into play. The purpose of this section is to discuss some properties of three-dimensional rotating turbulence, especially focusing on the similarities and differences with two-dimensional turbulence.

Governing Equations

We start with the Navier–Stokes equations for an incompressible fluid in a frame rotating with an angular frequency $\boldsymbol{\Omega}$:

$$\frac{\partial \boldsymbol{u}}{\partial t} + \boldsymbol{u}\cdot\nabla\boldsymbol{u} + \underbrace{2\boldsymbol{\Omega}\times\boldsymbol{u}}_{\text{Coriolis}} = -\nabla\Pi + \nu\nabla^2\boldsymbol{u} + \boldsymbol{F} \tag{6.56}$$

$$\nabla\cdot\boldsymbol{u} = 0, \tag{6.57}$$

where Π is the modified pressure taking into account centrifugal effects. In addition to the Reynolds number, we have introduced a second important dimensionless number, the Rossby number Ro defined as a balance between inertial and Coriolis terms

$$\frac{|\boldsymbol{u}\cdot\nabla\boldsymbol{u}|}{|\boldsymbol{\Omega}\times\boldsymbol{u}|} \sim \frac{U}{\Omega L} \equiv Ro\ . \tag{6.58}$$

Three important regimes can be discussed as follows:

- When $Ro \gg 1$, the turbulence ignores rotation and behaves like 3D homogeneous isotropic turbulence.
- When $Ro \sim 1$, the turbulence becomes anisotropic and is dynamically affected by rotation. A gradual transition to quasi-2D dynamics can be observed.
- When $Ro \ll 1$, inertial waves and quasi-geostrophic motions dominate the dynamics.

Very importantly, the length scale L introduced to define the Rossby number is left to be defined for now. In a turbulent flow with a wide range of spatial scales, we naturally expect the local Rossby number (based on an eddy size l for example) to go from very small values at large scales to very large values at small scales. Note also that quasi-geostrophic models discussed previously are effectively filtering out inertial waves. They can nevertheless have an important impact on the dynamics at low Rossby numbers.

Inertial Waves

Similarly to the case of β-plane turbulence discussed previously, linearizing the equations leads to nontrivial dynamics. Considering the linear inviscid limit of the

Navier–Stokes equations in a rotating frame, one gets the Poincaré equation (Poincaré 1885):

$$\frac{\partial^2 \nabla^2 \boldsymbol{u}}{\partial t^2} + 4\Omega^2 \frac{\partial^2 \boldsymbol{u}}{\partial z^2} = 0, \tag{6.59}$$

which, looking for plane wave solutions, leads to the dispersion relation of inertial waves:

$$\omega = \pm 2\Omega \frac{k_z}{k} = \pm 2\Omega \cos\theta, \tag{6.60}$$

where we have introduced the polar angle θ between the wave vector $\boldsymbol{k}$ and the vertical axis, k_z being the vertical component of the wave vector. Inertial waves frequency is bounded by 2Ω so that they are expected to dominate the low-frequency part of the spectrum. The dispersion relation is anisotropic and the frequency tends to zero for $k_z \to 0$. A visualization of inertial waves excited by an oscillating object in a rotating fluid can be seen in Fig. 6.6.

The role of inertial waves in the dynamics of rotating turbulence is still an active area of research. On the one hand, they are widely observed both in experiments (Yarom et al. 2013) and in numerical simulations (Favier et al. 2010). On the other hand, their role in the dynamics is still unclear. Are they passively generated by turbulent eddies or do they significantly contribute to energy transfers through resonant interactions? Note finally that it is also possible to consider the so-called wave turbulence limit, where low-amplitude inertial waves weakly interact (Galtier 2003; Bellet et al. 2006; Le Reun et al. 2017) without leading to the formation of turbulent eddies. This limit will not be discussed in the following and only finite-Rossby rotating turbulence will be considered.

Phenomenological Observations

There are several empirical observations about the behavior of homogeneous turbulence submitted to background rotation.

First, as the rotation rate is increased, the dissipation rate ϵ is reduced. This has been observed experimentally by rotating grid-generated turbulence (Jacquin et al. 1990) or by spinning a propeller in a rotating tank filled with water (Campagne et al. 2016). This reduction of dissipation can be understood by a reduction of the forward energy flux through the direct cascade.

The second empirical property of rotating turbulence is the systematic formation of columnar structures invariant along the rotation axis. This is related to the Taylor–Proudman theorem, which is valid in the limit of steady, vanishing Rossby number, and inviscid motions. In that case, the curl of the geostrophic balance shows that motions are invariant along the rotation axis. Note however that the hypotheses required to justify this result are all violated in rotating turbulence, so that explaining the dynamical formation of columnar structures in rotating turbulence solely based on the Taylor–Proudman theorem is an approximation at best.

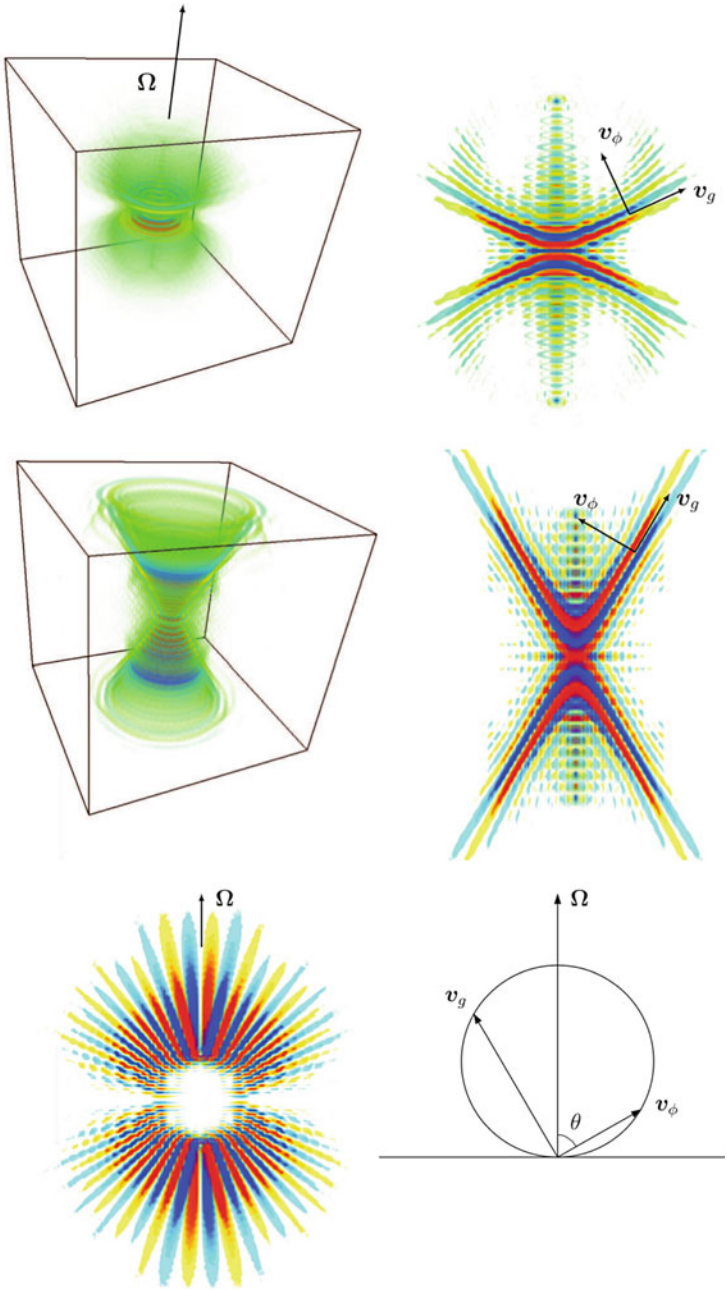

Fig. 6.6 Visualizations of the vertical velocity in a numerical simulation of inertial waves excited by an oscillating force localized at the center of the domain. The frequency is decreasing from the top panel to the middle one. At the bottom, we show the response to an impulse exciting a large band of frequencies. $\boldsymbol{v}_g$ is the group velocity while $\boldsymbol{v}_\phi$ is the phase velocity. Taken from Favier (2009)

Finally, the last important empirical observation concerns the cyclone–anticyclone asymmetry. During the process of anisotropy growth and columnar structure formation, the distribution of elongated vortices becomes asymmetric, such that cyclonic vorticity is favored. Cyclone–anticyclone asymmetry is indeed a generic feature of rotating flows, which originates from the modification of stretching and tilting of the vorticity by the Coriolis force, suggesting a more pronounced asymmetry at $Ro \sim 1$ and a restoration of symmetry for vanishing Rossby numbers. From an initially isotropic velocity field, it can be shown that, for short times (Gence and Frick 2001)

$$\frac{d}{dt}\left\langle \omega_z^3 \right\rangle = \frac{4}{5}\Omega \left\langle \omega_i \omega_j S_{ij} \right\rangle \ , \tag{6.61}$$

which explains the asymmetric nature of the probability density function of the vertical vorticity observed in many rotating turbulent flows. From an initially symmetric distribution function (i.e., $\left\langle \omega_z^3 \right\rangle \approx 0$), rotation breaks the cyclone–anticyclone symmetry. In addition, it is known that cyclonic vortices are more robust against centrifugal and elliptic instabilities than anti-cyclonic vortices (Sipp et al. 1999).

Anisotropic Energy Transfers

A very important observation is that the Coriolis force does no work ($\boldsymbol{u} \cdot (\boldsymbol{\Omega} \times \boldsymbol{u}) = 0$) so that the kinetic energy equation (which is a second order quantity) is unchanged in the rotating frame. Rotation does affect the kinetic energy transfers (which is a third-order quantity) by reducing the forward cascade, reducing dissipation, and generating anisotropic energy transfers (Cambon et al. 1997). The Coriolis force being anisotropic, energy transfers along the rotation axis are inevitably different from those perpendicular to it. The concept of isotropization of the turbulence where all statistical quantities can be reduced to isotropic tensors is not applicable anymore. In Fourier space, this means that statistical quantities do not only depend on the amplitude k of the wave vector $\boldsymbol{k}$, but also on its orientation. The angular energy spectrum $E(k, \theta)$ can be defined by

$$K = \frac{1}{2}\int \hat{R}_{ii}(\boldsymbol{k})\mathrm{d}\boldsymbol{k} = \int e(\boldsymbol{k})\mathrm{d}\boldsymbol{k} = \int_0^\infty \int_0^\pi \underbrace{\int_0^{2\pi} e(\boldsymbol{k}) k^2 \sin\theta \mathrm{d}\phi}_{E(k,\theta)} \mathrm{d}\theta \mathrm{d}k, \tag{6.62}$$

where the dependence on the polar angle θ is conserved, contrary to standard isotropic spectral statistics. Rotating turbulence is typically characterized by

$$E(k, \theta \approx 0) \ll E(k, \theta \approx \pi/2)$$

where $\theta = 0$ corresponds to purely vertical wave vectors (associated with spatial structures nearly invariant along the horizontal directions), whereas $\theta = \pi/2$ corre-

sponds to horizontal wave vectors (associated with spatial structures invariant along the vertical direction). Energy is not only transferred across wave numbers but also across angles from the pole to the equator. Note that as $\theta \to \pi/2$, $k_z \to 0$, and $\partial_z \to 0$, which is of course consistent with the formation of columnar structures discussed earlier. The question remains at which spatial scales are these columnar anisotropic structures expected?

Using the usual scaling $\epsilon \sim u^3/l$, one can build a typical length scale L_Z where the local Rossby number is around unity (Zeman 1994):

$$Ro(L_Z) = \frac{(L_Z\epsilon)^{1/3}}{\Omega L_Z} \sim 1 \quad \Rightarrow \quad L_Z = \left(\frac{\epsilon}{\Omega^3}\right)^{1/2}. \tag{6.63}$$

Scales larger than L_Z have a low Rossby number and are dynamically constrained by rotation. Scales smaller than L_Z have a large Rossby number and should recover an isotropic behavior. This transitional length scale separating anisotropic and isotropic dynamics has been observed in simulations (Delache et al. 2014).

Inverse Cascade

Since rotating turbulence naturally tends to transfer energy toward the $k_z = 0$ plane, it is then natural to focus on the dynamics of the $k_z = 0$ modes. Remember that modes with $k_z = 0$ are steady non-propagative motions when considering the dispersion relation of inertial waves (6.60). Starting from the Navier–Stokes equations without rotation but assuming that $\partial/\partial_z = 0$ leads to

$$\frac{\partial \boldsymbol{u}_h}{\partial t} + \boldsymbol{u}_h \cdot \nabla \boldsymbol{u}_h = -\nabla_h p + \nu \nabla_h^2 \boldsymbol{u}_h \tag{6.64}$$

$$\frac{\partial w}{\partial t} + \boldsymbol{u}_h \cdot \nabla_h w = \nu \nabla_h^2 w, \tag{6.65}$$

where $\boldsymbol{u}_h$ and w are the horizontal and vertical velocity components, respectively, and ∇_h is the horizontal gradient operator. The vertical component is passively advected by the horizontal flow while the horizontal flow satisfies the standard 2D Navier–Stokes equation. This state is often referred to as 2D-3C turbulence for two-dimensional three-components turbulence. We therefore expect that, in the limit where the flow becomes vertically invariant, an inverse cascade can develop in analogy with truly 2D turbulence. Of course, rotating turbulence is not exactly invariant along the rotation axis (see Gallet (2015) though), so that a transition is expected as the Rossby number is varied. An inverse cascade of the depth-invariant geostrophic modes is indeed observed in numerical simulations (Pouquet et al. 2013; Yokoyama and Takaoka 2017) and experiments (Campagne et al. 2014) when the Rossby number is low enough.

3D Homogeneous Turbulence in Stratified Fluids

This section is devoted to the case of fully three-dimensional turbulence in a linearly stratified fluid. As usual, we consider a homogeneous situation without boundaries and there is an external force injecting energy in the system.

Equations

Using the Boussinesq approximation, we consider the equations of motions

$$\frac{\partial \boldsymbol{u}}{\partial t} + \boldsymbol{u}\cdot\nabla\boldsymbol{u} = -\frac{1}{\rho_0}\nabla p + \nu\nabla^2\boldsymbol{u} - \frac{\rho}{\rho_0}g\boldsymbol{e}_z \tag{6.66}$$

$$\nabla\cdot\boldsymbol{u} = 0 \tag{6.67}$$

$$\frac{\partial \rho}{\partial t} + \boldsymbol{u}\cdot\nabla\rho = \kappa\nabla^2\rho + u_z\frac{\rho_0 N^2}{g}, \tag{6.68}$$

where ρ_0 is mean density, κ is the diffusivity of the stratifying agent, ν is the viscosity, ρ is the density perturbation around the equilibrium profile $\overline{\rho}(z) = \rho_0\left(1 - N^2 z/g\right)$, and $N = \sqrt{-\frac{g}{\rho_0}\frac{\partial\overline{\rho}}{\partial z}}$ is the Brunt–Väisälä frequency.

There are several important dimensionless numbers in this problem:

- The Reynolds number $Re = \frac{UL}{\nu}$,
- The Froude number $Fr = \frac{U}{NL}$,
- The Richardson number $Ri = \frac{N^2}{|\partial \boldsymbol{u}_h/\partial z|^2}$,
- The Schmidt number $Sc = \frac{\nu}{\kappa}$,

where we have introduce a typical velocity scale U and a typical length scale L.

These equations can be made dimensionless using various approaches. Scaling velocity with U, length with L, time with N^{-1}, and buoyancy $b \equiv \rho g/\rho_0$ with UN gives the following set of dimensionless equations (Lilly 1983):

$$\frac{\partial \boldsymbol{u}}{\partial t} + Fr\ \boldsymbol{u}\cdot\nabla\boldsymbol{u} = -\nabla p + \frac{Fr}{Re}\nabla^2\boldsymbol{u} + b\boldsymbol{e}_z \tag{6.69}$$

$$\frac{\partial b}{\partial t} + Fr\ \boldsymbol{u}\cdot\nabla b = -u_z + \frac{Fr}{Re\ Sc}\nabla^2 b \tag{6.70}$$

$$\nabla\cdot\boldsymbol{u} = 0. \tag{6.71}$$

In the low Froude and ideal (i.e., neglecting viscous and diffusive terms) limit, one recovers the internal wave equation

$$\frac{\partial}{\partial t}\nabla^2\phi + N^2\nabla_h^2\phi = 0, \tag{6.72}$$

where ∇_h is the horizontal gradient operator and ϕ is a velocity potential function. Internal waves correspond to the linear oscillatory response of a linearly stratified fluid and share several properties with inertial waves (dispersive, orthogonality between group and phase velocities, bounded frequencies). Similarly to rotating turbulence, stratified turbulence is characterized by a superposition and interaction between turbulent eddies and linear or weakly nonlinear waves.

Let us consider another way of scaling the equations. Scaling horizontal velocities with U, length with L, time with L/U, b with U^2/L, and vertical velocity with $U^3/(N^2L^2)$ (this particular scaling is obtained by a balance between $\partial_t b$ and $N^2 u_z$ in the buoyancy equation) gives

$$\frac{\partial \boldsymbol{u}_h}{\partial t} + \boldsymbol{u}_h \cdot \nabla_h \boldsymbol{u}_h + Fr^2 u_z \partial_z \boldsymbol{u}_h = -\nabla_h p + \frac{1}{Re}\nabla^2 \boldsymbol{u}_h \tag{6.73}$$

$$Fr^2 \left(\frac{\partial u_z}{\partial t} + \boldsymbol{u} \cdot \nabla u_z \right) = -\partial_z p + b + \frac{1}{Re}\nabla^2 u_z \tag{6.74}$$

$$\frac{\partial b}{\partial t} + \boldsymbol{u}_h \cdot \nabla b + Fr^2 u_z \partial_z b = -u_z + \frac{1}{Re\ Sc}\nabla^2 b \tag{6.75}$$

$$\nabla_h \cdot \boldsymbol{u}_h + Fr^2 \partial_z u_z = 0. \tag{6.76}$$

In the low Froude inviscid limit, one gets quasi-2D layered motions

$$\frac{\partial \nabla^2 \psi}{\partial t} + J(\psi, \nabla_h^2 \psi) = 0, \tag{6.77}$$

where $\psi(x, y, z, t)$ is the streamfunction. This equation is similar to the standard 2D Euler equation discussed previously in the context of 2D turbulence, except that the stream function depends on all three spatial coordinates.

These two particular scalings illustrate that strongly stratified flows can support two types of motions: three-dimensional internal waves and quasi-2D layered motions. While this could suggest that stratified turbulence and 2D turbulence share some similarities, there is an obvious limitation to the previous scaling. There is no information about the vertical correlation length between each layer. Are they decoupled or is there some vertical correlation in a turbulent stratified flow? Note also that this is reminiscent of rotating turbulence and the duality between inertial waves and geostrophic vortices.

The Zig-Zag Instability and the Buoyancy Scale

The Zig-Zag instability is characteristic of an initially vertically invariant vortex pair moving in a linearly stratified fluid (Billant and Chomaz 2000a). The vortex pair breaks into several layers with a well-defined vertical thickness. The most unstable vertical wavelength of the Zig-Zag instability is found to be Billant and Chomaz (2000b):

$$\lambda_z \sim U/N, \tag{6.78}$$

where U is the vortex pair traveling velocity and N is the Brunt–Väisälä frequency. Billant and Chomaz (2001) also showed that the inviscid governing equations in the limit $Fr \to 0$ are self-similar with respect to the variable zN/U. Vortex structures with a vertical size scaling like U/N have been also reported in stratified Taylor–Couette flows in the strongly stratified regime (Boubnov et al. 1995). It was therefore suggested that the intrinsic vertical scale, when no vertical length scales are imposed by initial or boundary conditions and when the fluid is strongly stratified, is given by

$$L_B = U/N\ , \tag{6.79}$$

the so-called buoyancy scale.

It is natural to focus on the dominant horizontal flow $\boldsymbol{u}_h = \left(u_x, u_y, 0\right)$ and on its correlation length scales

$$l_h = \frac{1}{\overline{\boldsymbol{u}_h^2}} \int \overline{\boldsymbol{u}_h(\boldsymbol{x}) \cdot \boldsymbol{u}_h(\boldsymbol{x} + r\boldsymbol{e}_h)} \mathrm{d}r \quad \text{and} \quad l_v = \frac{1}{\overline{\boldsymbol{u}_h^2}} \int \overline{\boldsymbol{u}_h(\boldsymbol{x}) \cdot \boldsymbol{u}_h(\boldsymbol{x} + r\boldsymbol{e}_z)} \mathrm{d}r\ , \tag{6.80}$$

where the overbar represents an averaging process, $\boldsymbol{e}_h$ and $\boldsymbol{e}_z$ are unit vectors in the horizontal and vertical directions, respectively. One can then define horizontal and vertical Froude numbers:

$$Fr_h = \frac{u_h}{N l_h} \quad \text{and} \quad Fr_v = \frac{u_h}{N l_v} \quad \text{where} \quad u_h = \sqrt{\overline{\boldsymbol{u}_h^2}}\ . \tag{6.81}$$

The incompressibility constraint leads to $u_v/l_v \sim u_h/l_h$ where u_v is a typical vertical velocity. In the strong stratification regime, one might expect $u_v \ll u_h$ so that $l_v \ll l_h$. The empirical observation that $l_v \sim L_B = U/N$ leads to $Fr_v \sim 1$ and not $Fr_v \to 0$ as assumed in the 2D layered turbulence characterized by Eq. (6.77).

The Buoyancy Reynolds Number

Strongly stratified turbulence is characterized by $Fr_h \ll 1$ and it organizes itself such that $Fr_v \sim 1$ or equivalently $l_v \sim U/N$ (Billant and Chomaz 2001; Riley and deBruynKops 2003). Using this scaling, the ratio between the horizontal inertial forces and the vertical viscous forces is

$$\frac{u_h^2/l_h}{\nu u_h/l_v^2} = \frac{u_h l_h}{\nu} \left(\frac{u_h}{N l_h}\right)^2 = Re_h Fr_h^2 \equiv \mathcal{R}\ , \tag{6.82}$$

where we have introduced the buoyancy Reynolds number $\mathcal{R}$. For the horizontal motions to be viscously decoupled in the vertical direction, one requires $\mathcal{R} \gg 1$ or

equivalently $Re_h \gg Fr_h^{-2} \gg 1$. This double limit is very difficult to achieve numerically and a transition between viscously locked layers when $\mathcal{R} \ll 1$ and strong stratified turbulence when $\mathcal{R} \gg 1$ has only been achieved recently (Brethouwer et al. 2007; Waite 2011).

From numerical simulations, it is observed that $\epsilon \sim u_h^3/l_h$. Following Kolmogorov's approach this leads to (Lindborg 2006):

$$E_h \sim \epsilon^{2/3} k_h^{-5/3} ,$$

where E_h is the horizontal energy spectrum and k_h is the horizontal wave number. It is still not clear if this scaling is indeed observed in the regime of large buoyancy Reynolds number.

Using the usual scaling $\epsilon \sim u^3/l$, one can build a typical length scale L_0, the so-called Ozmidov scale (Ozmidov 1965), where the local Froude number is around unity

$$Fr(L_0) = \frac{(L_0\epsilon)^{1/3}}{N L_0} \sim 1 \quad \Rightarrow \quad L_0 = \left(\frac{\epsilon}{N^3}\right)^{1/2} . \tag{6.83}$$

Scales larger than L_0 have a low Froude number and are dynamically constrained by stratification. Scales smaller than L_0 have a large Froude number and should recover an isotropic behavior. This is similar to the Zeman scale of rotating turbulence.

- In the ocean, $L_0 \sim 1\,\mathrm{m}$.
- In strongly stable atmosphere boundary layers $L_0 \sim 1\,\mathrm{m}$.
- In the upper troposphere or lower stratosphere, $L_0 \sim 10\,\mathrm{m}$.

Conclusion

These notes are at best a very broad introduction to the many subtleties of turbulence in rapidly rotating and stratified fluids. Many fundamental aspects have been neglected to focus on simpler physical processes or qualitative descriptions. The interested reader can read more complete classical textbooks cited throughout this review, in particular Davidson (2013).

To bridge the gap between this introduction and more applied issues relevant to the fluid dynamics of planets and stars, several additional effects have to be taken into account. Compressibility is one of them, since density can change by many orders of magnitude in stellar interiors or planetary atmospheres. Some properties of compressible turbulence, which are also relevant to engineering applications such as turbo-machinery, are, for example, discussed in Sagaut and Cambon (2008). Astrophysical fluids are often electrically conducting and therefore interact dynamically with the magnetic field. An introduction to magnetohydrodynamics is given in the chapter by Deguen and Lasbleis of the same book. The topic of magnetohydrodynamical turbulence is vast since it applies to many geophysical and astrophysical

flows from the Earth's liquid metal core to the ionized gases of stellar interiors. Finally, coupling all these effects together remain a tremendous task involving many dimensionless numbers and many different regimes depending on the spatial scales considered (Alexakis and Biferale 2018).

References

Alexakis, A. (2011). Two-dimensional behavior of three-dimensional magnetohydrodynamic flow with a strong guiding field. *Physical Review E*, *84*, 056330.

Alexakis, A., & Biferale, L. (2018). Cascades and transitions in turbulent flows. *Physics Reports*,.

Batchelor, G. K. (1953). *The Theory of Homogeneous Turbulence*. Cambridge Science Classics: Cambridge University Press. ISBN 9780521041171.

Bellet, F., Godeferd, F. S., Scott, J. F., & Cambon, C. (2006). Wave turbulence in rapidly rotating flows. *Journal of Fluid Mechanics*, *562*, 83–121.

Benavides, S. J., & Alexakis, A. (2017). Critical transitions in thin layer turbulence. *Journal of Fluid Mechanics*, *822*, 364–385.

Billant, P., & Chomaz, J.-M. (2000a). Experimental evidence for a new instability of a vertical columnar vortex pair in a strongly stratified fluid. *Journal of Fluid Mechanics*, *418*, 167–188.

Billant, P., & Chomaz, J.-M. (2000b). Three-dimensional stability of a vertical columnar vortex pair in a stratified fluid. *Journal of Fluid Mechanics*, *419*, 65–91.

Billant, P., & Chomaz, J.-M. (2001). Self-similarity of strongly stratified inviscid flows. *Physics of Fluids*, *13*(6), 1645–1651.

Boffetta, G., & Musacchio, S. (2010). Evidence for the double cascade scenario in two-dimensional turbulence. *Physical Review E*, *82*, 016307.

Boubnov, B. M., Gledzer, E. B., & Hopfinger, E. J. (1995). Stratified circular couette flow: Instability and flow regimes. *Journal of Fluid Mechanics*, *292*, 333–358.

Brethouwer, G., Billant, P., Lindborg, E., & Chomaz, J.-M. (2007). Scaling analysis and simulation of strongly stratified turbulent flows. *Journal of Fluid Mechanics*, *585*, 343–368.

Cabanes, S., Aurnou, J., Favier, B., & Le Bars, M. (2017). A laboratory model for deep-seated jets on the gas giants. *Nature Physics*, *13*(4), 387.

Cambon, C., Mansour, N. N., & Godeferd, F. S. (1997). Energy transfer in rotating turbulence. *Journal of Fluid Mechanics*, *337*, 303–332.

Campagne, A., Gallet, B., Moisy, F., & Cortet, P.-P. (2014). Direct and inverse energy cascades in a forced rotating turbulence experiment. *Physics of Fluids*, *26*(12), 125112.

Campagne, A., Machicoane, N., Gallet, B., Cortet, P.-P., & Moisy, F. (2016). Turbulent drag in a rotating frame. *Journal of Fluid Mechanics*, *794*, R5.

Celani, A., Musacchio, S., & Vincenzi, D. (2010). Turbulence in more than two and less than three dimensions. *Physical Review Letters*, *104*, 184506.

Chen, S., Ecke, R. E., Eyink, G. L., Rivera, M., Wan, M., & Xiao, Z. (2006). Physical mechanism of the two-dimensional inverse energy cascade. *Physical Review Letters*, *96*, 084502.

Chertkov, M., Connaughton, C., Kolokolov, I., & Lebedev, V. (2007). Dynamics of energy condensation in two-dimensional turbulence. *Physical Review Letters*, *99*, 084501.

Clarke, C., Carswell, B., & Carswell, R. F. (2007). *Principles of astrophysical fluid dynamics*. Cambridge: Cambridge University Press.

Clercx, H. J. H., Nielsen, A. H., Torres, D. J., & Coutsias, E. A. (2001). Two-dimensional turbulence in square and circular domains with no-slip walls. *European Journal of Mechanics - B/Fluids*, *20*(4), 557–576.

Couder, Y., Chomaz, J. M., & Rabaud, M. (1989). On the hydrodynamics of soap films. *Physica D: Nonlinear Phenomena*, *37*(1), 384–405.

Davidson, P. A. (2013). *Turbulence in rotating, stratified and electrically conducting fluids*. Cambridge: Cambridge University Press.
Delache, A., Cambon, C., & Godeferd, F. S. (2014). Scale by scale anisotropy in freely decaying rotating turbulence. *Physics of Fluids*, *26*(2), 025104.
Favier, B. (2009). *Modélisation et simulations en turbulence homogène anisotrope: effets de rotation et magnétohydrodynamique*. Ph.D. thesis, Ecole Centrale de Lyon.
Favier, B., Godeferd, F. S., & Cambon, C. (2010). On space and time correlations of isotropic and rotating turbulence. *Physics of Fluids*, *22*(1), 015101.
Favier, B., Godeferd, F. S., Cambon, C., Delache, A., & Bos, W. J. T. (2011). Quasi-static magneto-hydrodynamic turbulence at high reynolds number. *Journal of Fluid Mechanics*, *681*, 434–461.
Favier, B., Silvers, L. J., & Proctor, M. R. E. (2014). Inverse cascade and symmetry breaking in rapidly rotating Boussinesq convection. *Physics of Fluids*, *26*, 096605.
Favier, B., Guervilly, C., & Knobloch, E. (2019). Subcritical turbulent condensate in rapidly rotating Rayleigh-Bénard convection. *Journal of Fluid Mechanics*, *864*, R1.
Frisch, U. (1995). *Turbulence: the legacy of AN Kolmogorov*. Cambridge: Cambridge University Press.
Gallet, B. (2015). Exact two-dimensionalization of rapidly rotating large-reynolds-number flows. *Journal of Fluid Mechanics*, *783*, 412–447.
Galperin, B., & Read, P. L. (2019). *Zonal jets: Phenomenology, genesis, and physics*. Cambridge: Cambridge University Press.
Galperin, R. M. B., Young, R. M., Sukoriansky, S., Dikovskaya, N., Read, P. L., Lancaster, A. J., et al. (2014). Cassini observations reveal a regime of zonostrophic macroturbulence on jupiter. *Icarus*, *229*, 295–320.
Galtier, S. (2003). Weak inertial-wave turbulence theory. *Physical Review E*, *68*, 015301.
Gence, J. N., & Frick, C. (2001). Birth of the triple correlations of vorticity in an homogenous turbulence submitted to a solid body rotation. *Comptes Rendus de l'Académie des Sciences*, *329*(5), 351–356.
Gharib, M., & Derango, P. (1989). A liquid film (soap film) tunnel to study two-dimensional laminar and turbulent shear flows. *Physica D: Nonlinear Phenomena*, *37*(1), 406–416.
Huang, H.-P., Galperin, B., & Sukoriansky, S. (2001). Anisotropic spectra in two-dimensional turbulence on the surface of a rotating sphere. *Physics of Fluids*, *13*(1), 225–240.
Jacquin, L., Leuchter, O., Cambon, C., & Mathieu, J. (1990). Homogeneous turbulence in the presence of rotation. *Journal of Fluid Mechanics*, *220*, 1–52.
Julien, K., Rubio, A. M., Grooms, I., & Knobloch, E. (2012). Statistical and physical balances in low Rossby number Rayleigh-Bénard convection. *Geophysical and Astrophysical Fluid Dynamics*, *106*, 392–428.
Kolmogorov, A. N. (1941). The local structure of turbulence in incompressible viscous fluid for very large reynolds numbers. *Comptes rendus de l'Académie des sciences de l'URSS*, *30*, 301–305.
Kraichnan, R. H. (1967). Inertial ranges in 2D turbulence. *Physics of Fluids*, *10*, 1417–1423.
Laurie, J., Boffetta, G., Falkovich, G., Kolokolov, I., & Lebedev, V. (2014). Universal profile of the vortex condensate in two-dimensional turbulence. *Physical Review Letters*, *113*, 254503.
Le Reun, T., Favier, B., Barker, A. J., & Le Bars, M. (2017). Inertial wave turbulence driven by elliptical instability. *Physical Review Letters*, *119*, 034502.
Lilly, D. K. (1983). Stratified turbulence and the mesoscale variability of the atmosphere. *Journal of the Atmospheric Sciences*, *40*(3), 749–761.
Lindborg, E. (2006). The energy cascade in a strongly stratified fluid. *Journal of Fluid Mechanics*, *550*, 207–242.
Ozmidov, R. V. (1965). On the turbulent exchange in a stably stratified ocean. *Izvestiya - Academy of Sciences USSR, Atmospheric and oceanic physics*, *1*, 493–497.
Paret, J., & Tabeling, P. (1997). Experimental observation of the two-dimensional inverse energy cascade. *Physical Review Letters*, *79*, 4162–4165.
Pedlosky, J. (1992). *Geophysical fluid dynamics. Springer study edition*. New York: Springer.

Poincaré, H. (1885). Sur l'équilibre d'une masse fluide animée d'un mouvement de rotation. *Acta mathematica*, *7*(1), 259–380.
Pouquet, A., Sen, A., Rosenberg, D., Mininni, P. D., & Baerenzung, J. (2013). Inverse cascades in turbulence and the case of rotating flows. *Physica Scripta*, *T155*, 014032.
Rhines, P. B. (1975). Waves and turbulence on a beta-plane. *Journal of Fluid Mechanics*, *69*(3), 417–443.
Richardson, L. F. (1922). *Weather prediction by numerical process*.
Riley, J. J., & deBruynKops, S. M. (2003). Dynamics of turbulence strongly influenced by buoyancy. *Physics of Fluids*, *15*(7), 2047–2059.
Sagaut, P., & Cambon, C. (2008). *Homogeneous turbulence dynamics*. Cambridge: Cambridge University Press.
Sipp, D., Lauga, E., & Jacquin, L. (1999). Vortices in rotating systems: Centrifugal, elliptic and hyperbolic type instabilities. *Physics of Fluids*, *11*(12), 3716–3728.
Smith, L. M., Chasnov, J. R., & Waleffe, F. (1996). Crossover from two- to three-dimensional turbulence. *Physical Review Letters*, *77*, 2467–2470.
Smith, L. M., & Yakhot, V. (1993). Bose condensation and small-scale structure generation in a random force driven 2d turbulence. *Physical Review Letters*, *71*, 352–355.
Sukoriansky, S., Dikovskaya, N., & Galperin, B. (2007). On the arrest of inverse energy cascade and the rhines scale. *Journal of the Atmospheric Sciences*, *64*(9), 3312–3327.
Vallis, G. K. (2006). *Atmospheric and oceanic fluid dynamics*. UK: Cambridge University Press.
Vallis, G. K., & Maltrud, M. E. (1993). Generation of mean flows and jets on a beta plane and over topography. *Journal of Physical Oceanography*, *23*(7), 1346–1362.
Waite, M. L. (2011). Stratified turbulence at the buoyancy scale. *Physics of Fluids*, *23*(6), 066602.
Xia, H., Punzmann, H., Falkovich, G., & Shats, M. G. (2008). Turbulence-condensate interaction in two dimensions. *Physical Review Letters*, *101*, 194504.
Xia, H., Shats, M., & Falkovich, G. (2009). Spectrally condensed turbulence in thin layers. *Physics of Fluids*, *21*, 125101.
Xia, H., Byrne, D., Falkovich, G., & Shats, M. (2011). Upscale energy transfer in thick turbulent fluid layers. *Nature Physics*, *7*, 321–324.
Yarom, E., Vardi, Y., & Sharon, E. (2013). Experimental quantification of inverse energy cascade in deep rotating turbulence. *Physics of Fluids*, *25*(8), 085105.
Yokoyama, N., & Takaoka, M. (2017). Hysteretic transitions between quasi-two-dimensional flow and three-dimensional flow in forced rotating turbulence. *Phys. Rev. Fluids*, *2*, 092602.
Zeman, O. (1994). A note on the spectra and decay of rotating homogeneous turbulence. *Physics of Fluids*, *6*(10), 3221–3223.